PRIMARY COSMIC-RAY POSITRONS AND NEGATRONS IN 1968 AT ENERGIES BETWEEN 11 AND 204 MEV

Thesis by

Carl James Rice

In Partial Fulfillment of the Requirements

For the Degree of

Doctor of Philosophy

California Institute of Technology

Pasadena, California

1970

(Submitted December 22, 1969)

ACKNOWLEDGMENTS

This research topic was suggested by my faculty sponsor, Professor Rochus Vogt. I thank him for his invaluable guidance and support throughout the project.

Particular thanks are also due to Dr. Klaus Beuermann, who worked jointly in the design and development of the detector and in the flight program. In addition, his calculations of atmospheric secondary electrons were essential in the analysis of the data.

I wish to thank Professor Edward Stone and Dr. Martin Israel for valuable suggestions during the course of construction and data analysis. Design of the spark chamber readout system was aided by parallel work carried out by Dr. Charles Prescott and Mr. Walter Nilsson.

I acknowledge with thanks the very competent work of our laboratory personnel. The electronic system was designed and tested by Mr. William Blodgett, who also assisted in the flight operations at Fort Churchill. Mrs. Myrtle Casale, and Messers. John Toomer, Alton Story, and Richard Suchter contributed to the construction of the detector and support equipment. Messers. Harding Smith and Mark Radomsky ably assisted in construction and testing as well as data analysis.

The work of the personnel of the Bridge Laboratory Machine Shop under Mr. David Vail, and of the staff of Central Engineering Services is greatly appreciated.

I am grateful to Dr. Robert Walker for permission to calibrate our detector in the external electron beam of the Caltech Synchrotron Laboratory, and to the members of the synchrotron laboratory staff for aid during the calibration.

I also wish to thank the members of the Office of Naval Research and the flight crew of Raven Industries for the successful flight operations at Fort Churchill.

I am indebted to the National Science Foundation and the California Institute of Technology for financial aid during my graduate studies. The research described in this thesis was supported by the National Aeronautics and Space Administration under Grant NGL 05-002-007.

ABSTRACT

The cosmic-ray positron and negatron spectra between 11 and 204 MeV have been measured in a series of 3 high-altitude balloon flights launched from Fort Churchill, Manitoba, on July 16, July 21, and July 29, 1968. The detector system consisted of a magnetic spectrometer utilizing a 1000-gauss permanent magnet, scintillation counters, and a lucite Čerenkov counter.

Launches were timed so that the ascent through the 100 g/cm^2 level of residual atmosphere occurred after the evening geomagnetic cutoff transition. Data gathered during ascent are used to correct for the contribution of atmospheric secondary electrons to the flux measured at float altitude. All flights floated near 2.4 g/cm^2 residual atmosphere throughout the nighttime interval.

A pronounced morning intensity increase was observed in each flight. We present daytime positron and negatron data which support the interpretation of the diurnal flux variation as a change in the local geomagnetic cutoff. A large diurnal variation was observed in the count rate of positrons and negatrons with magnetic rigidities less than 11 MV and is evidence that the nighttime cutoff was well below this value.

Using nighttime data we derive extraterrestrial positron and negatron spectra. The positron-to-total-electron ratio which we measure indicates that the interstellar secondary, or collision, source contributes $\lesssim$50 percent of the electron flux within this energy interval. By comparing our measured positron spectrum with the positron spectrum calculated for the collision source we derive the absolute solar modulation for positrons in 1968. Assuming negligible energy loss during modulation, we derive the total interstellar electron spectrum as well as the spectrum of directly accelerated, or primary, electrons. We examine the effect of adiabatic deceleration and find that many of the conclusions regarding the interstellar electron spectrum are not significantly altered for an assumed energy loss of up to 50 percent of the original energy.

To Lorna

TABLE OF CONTENTS

LIST OF TABLES

LIST OF FIGURES

I. INTRODUCTION

Measurements of the composition and energy spectrum of cosmic rays are of importance to the study of a variety of astrophysical problems. The total energy content of the cosmic rays is sufficient to give them an important role in the dynamics of the galaxy. Knowledge of the galactic spectra of the cosmic-ray constituents is necessary to any theory which attempts to describe that role, as well as to theories of the origin, propagation, and containment of these energetic particles. The cosmic-ray spectra measured near the earth differ considerably from the interstellar spectra, however, due to the modulation effects of the solar wind. Measurements of the positron and negatron* spectra can provide a valuable tool for the study of the solar modulation of the cosmic-ray spectra. The only significant source of cosmic-ray positrons with energies above a few MeV is believed to be the decay of pions produced in collisions of high-energy cosmic-ray nuclei with the interstellar matter. The total solar modulation of the positron spectrum can be determined therefore by comparing measurements made near the earth with calculations of the

---

*In this thesis the designations "positron" and "negatron" will be used whenever the sign of the electron charge is relevant to the discussion.

interstellar spectrum of secondary positrons. The measured electron charge ratio provides information on the relative contributions of electrons resulting from pion decay and from other sources, and, when combined with the calculated secondary positron spectrum, enables us to reconstruct the interstellar electron spectrum from all sources. Coupled with surveys of the non-thermal galactic radio emission, knowledge of the interstellar electron spectrum can also yield information about conditions in interstellar space, in particular about the magnetic field and the location and extent of H_{II} regions.

Electrons represent only a small fraction of the cosmic rays incident on the earth. Early attempts to determine the primary electron flux (1-3) succeeded only in setting upper limits. The experiment of Critchfield, Ney, and Oleksa (3), for example, set an upper limit of 0.6 percent for the ratio of the flux of electrons with energy above 1 GeV to the total measured cosmic-ray flux. The presence of cosmic-ray electrons in the galaxy was deduced, however, from the observation of the galactic non-thermal radio noise. In 1950, Kiepenheuer (4) suggested that the galactic radio emission was synchroton radiation from high-energy electrons spiralling in the galactic magnetic field. He estimated that an electron flux of only one percent of

the cosmic-ray proton flux would be sufficient to account for the observed radio intensity. In 1952, Hayakawa (5) first examined the electron flux resulting from the decay of charged pions produced in interstellar nuclear interactions. He found by a rough calculation that a flux of the magnitude required by Kiepenheuer could be entirely accounted for by the pion-decay source alone.

The first direct observations of an extraterrestrial electron flux were made in 1960 by Meyer and Vogt (6) and by Earl (7). The cosmic-ray electron spectrum at the earth has been investigated subsequently by many workers (8-21). (These references are primarily recent results. References to earlier publications will be found in many of these papers.)

Several authors, taking advantage of improved knowledge of the relevant nuclear and galactic parameters, have recalculated the galactic equilibrium electron spectrum resulting from pion decay (22-29). The spectrum of interstellar knock-on electrons has also been calculated (30) and is found to dominate the pion-decay source below about 20 MeV. These two sources together constitute the collision, or so-called "secondary", source of interstellar electrons. Alternative sources which have been suggested for the origin of cosmic-ray electrons (such as Fermi acceleration or acceleration in super-novae or pulsars (25) (31)) all

involve direct acceleration and hence are referred to as "primary" sources. The secondary source contains a high proportion of positrons at all except the lowest energies. The primary source, whatever its exact nature, very probably injects only negatrons, since the energetic particles are accelerated out of the ambient matter, which presumably contains few free positrons. Hence a comparison of the electron charge ratio measured at the earth with that calculated for the secondary source alone permits the determination of the relative contributions of the primary and secondary cosmic-ray electron sources.

Experiments to measure the electron charge ratio have been performed by several investigators. A University of Chicago group flew a balloon-borne magnetic spectrometer during the period from 1963 to 1966 (32-35). The instrument covered an energy range from about 200 MeV to 14 BeV. Their measured positron spectrum agrees with calculations for positrons from pion decay but indicates that the majority of particles of these energies are of primary, rather than secondary, origin. Two other balloon-borne experiments have utilized the east-west asymmetry of the geomagnetic cutoff to determine electron charge ratios. A Saclay-University of Milan group flew a spark chamber experiment at a location with a vertical cutoff rigidity of 5.4 GV (36) (15). They reported a positron fraction,

$N_{e+}/(N_{e+} + N_{e-})$, of $< 0.39 \pm 0.11$ between 4.6 and 6.5 GeV. Daniel and Stephens flew oriented emulsions where the vertical cutoff rigidity was 16.2 GV (37). They claimed to see a positron fraction of 0.70 ± 0.20 between 15 and 50 GeV. In later publications the quoted error limits have been considerably increased, however, and analysis of additional events has indicated a possible negative excess (38) (39). Their reported electron spectrum is considerably above the calculated secondary spectrum at these energies.

Cline and Hones, using a satellite-borne detector, have reported a flux of 200 positrons/$(m^2 \cdot sec \cdot sr \cdot MeV)$ between 0.5 and 3.0 MeV (40). Their instrument identified positrons by detecting the annihilation photons and did not measure the total electron flux. Because of instrumental uncertainties the measurement was quoted as an upper limit. This very high positron flux is several orders of magnitude above the pion-decay source at these energies. Beta decay of radioactive spallation products in the cosmic rays has been examined as a possible source for these positrons (41) (42). This source requires a very large interstellar flux of cosmic-ray nuclei, however.

Recently Cline and Porreca (43) and Kniffen, Cline, and Fichtel (44) have reported measurements of the positron and negatron spectra between 2 and 10 MeV and between 35

and 220 MeV, respectively. We shall discuss their measurements in Chapter V.

In this thesis we report measurements of the positron and negatron spectra between 11 and 204 MeV made during three high-altitude balloon flights launched from Fort Churchill, Manitoba, in July, 1968. We have concentrated on this energy interval since it was previously only poorly explored due to inherent experimental difficulties and was potentially of great value for solar modulation studies. Other means of studying the absolute solar modulation, such as measurements of the deuterium and helium-3 spectra or inferences from the galactic synchrotron radiation, are confined by experimental limitations to rigidities above several hundred MV. Previous measurements of the electron spectrum between 10 and 200 MeV at the earth fell well below the calculated interstellar secondary spectrum alone. Over most of this energy interval the calculated positron fraction of the secondary source is considerably greater than one-half. Since the data of the University of Chicago group indicated that the measured positron fraction might be increasing below $\sim$ 400 MeV, it appeared that a measurable positron flux might be found below 200 MeV. Such measurements would yield valuable new information about solar modulation and the interstellar electron spectrum.

Measured electron spectra which overlap all or part of our energy range have been published previously (11) (18) (21) (45) (46). Although this reference list is confined to satellite experiments and to balloon experiments for which the local geomagnetic cutoff is known to fall below the detector threshold, there are nevertheless large differences in the reported fluxes. The variations may be attributable in part to solar modulation effects. However, in the case of balloon-borne detectors, the uncertainties introduced by large corrections for secondary electrons produced in the residual atmosphere above the instrument may contribute significantly. The satellite experiments (21) (45) have different, but no less severe, problems correcting for background events. In our work we make use of new calculations of the growth curves of atmospheric secondary positrons and negatrons (47), together with data gathered during ascent, to determine the atmospheric secondary contribution at float altitudes. (A complete discussion is found in Chapter IV, Section E). We derive an extraterrestrial electron spectrum which is in general close to or somewhat below previously reported intensities. Our results connect well to the most reliable data measured below and above this energy interval. Our measured extraterrestrial positron and negatron spectra give a charge ratio which is substantially constant throughout the

interval and indicate that the collision source contributes 30-50 percent of the measured electron flux over most of the range between 11 and 204 MeV. We derive the absolute solar modulation of positrons by comparing our measured spectrum with the interstellar positron spectrum calculated for the collision source. Neglecting energy loss during modulation we derive the interstellar electron spectrum between 11 and 204 MeV and extrapolate this spectrum to higher energies. This result is compared with the electron spectrum inferred by other investigators from radio data. The electron spectrum from primary sources alone is also derived. We examine the effect of adiabatic deceleration of cosmic rays passing through the solar wind and find that many of our conclusions regarding the interstellar electron spectrum remain essentially unaffected even for relatively large energy loss.

II. INSTRUMENT

A) Detector system

1) Overall description

The detector is a magnetic spectrometer, an instrument which measures the charge sign and magnetic rigidity (momentum divided by charge) of charged particles by determining their deflection in a magnetic field. Instrument parameters are chosen such that the rigidity interval 6-200 MV can be studied with good resolution. A schematic cross-section of the detector is shown in Figure 1.

A triple coincidence of Telescope Counter #1 (T1), Telescope Counter #2 (T2), and the Lucite Čerenkov Counter (C), triggers the spark chamber high voltage and initiates the data readout cycle. Two 4-gap wire spark chambers determine the trajectory of the particle before and after traversal of the gap of a permanent magnet. The spark locations are detected by magnetostrictive pickups and recorded in digital form on magnetic tape.

The Lucite Čerenkov counter is designed to discriminate against upward-moving splash albedo particles and to eliminate the nucleonic component of the cosmic rays in the rigidity interval of interest. The velocity threshold for Čerenkov emission in lucite (index of refraction = 1.49) is 0.67 c; corresponding rigidity thresholds are .46, 845

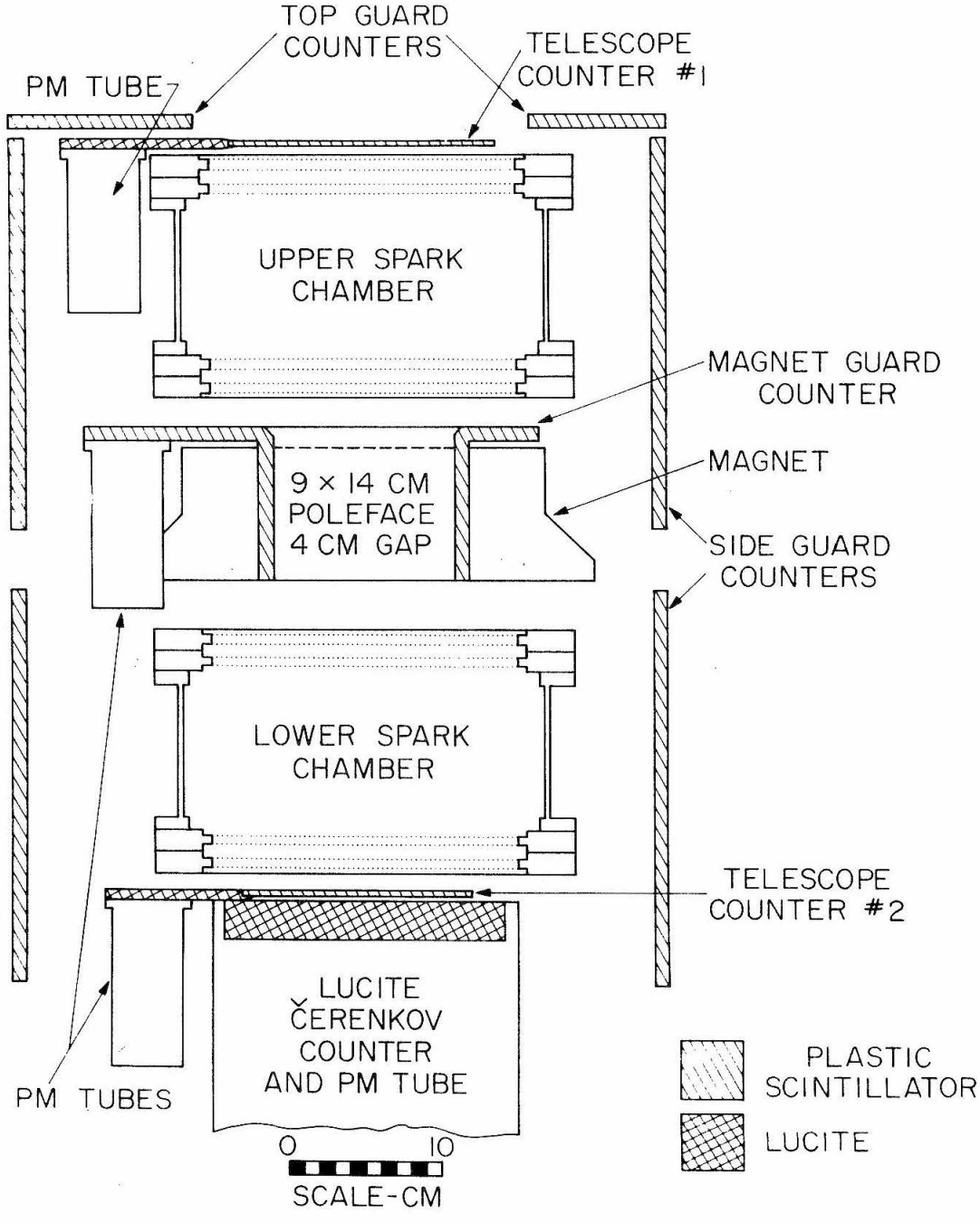

Fig. 1. Cross-section of the detector system.

and 1690 MV for electrons, protons, and alpha particles, respectively. Electronic pulse discrimination increases the rigidity threshold an additional 15 percent.

The specially designed Magnet Guard Counter, MA, is shown in Figure 2, together with the magnet, in an "exploded" isometric projection. The magnet guard counter covers the top of the magnet and completely lines the gap volume leaving a 3-cm x 12-cm open passage. This guard counter eliminates particles which might interact or scatter in the magnet pole pieces and, together with T1 and T2, defines the acceptance cone of the detector. Additional guard counters surround the sides of the instrument and cover the top with the exception of the telescope aperture. These counters eliminate charged particles which enter the detector from outside the acceptance cone and might subsequently interact, producing particles which trigger the telescope counters. All guard counters are in active anti-coincidence.

The atmospheric pressure during flight is monitored by a Wallace-Tiernan aneroid barometer (FA 160) which is photographed, together with a clock and a thermometer, at 5-minute intervals. The calibrated barometer is accurate to within ± 0.1 mb at 2.4 mb, our typical float altitude. An additional low-pressure gauge (Metro-physics Inc, Santa Barbara, Calif) is read out electronically.

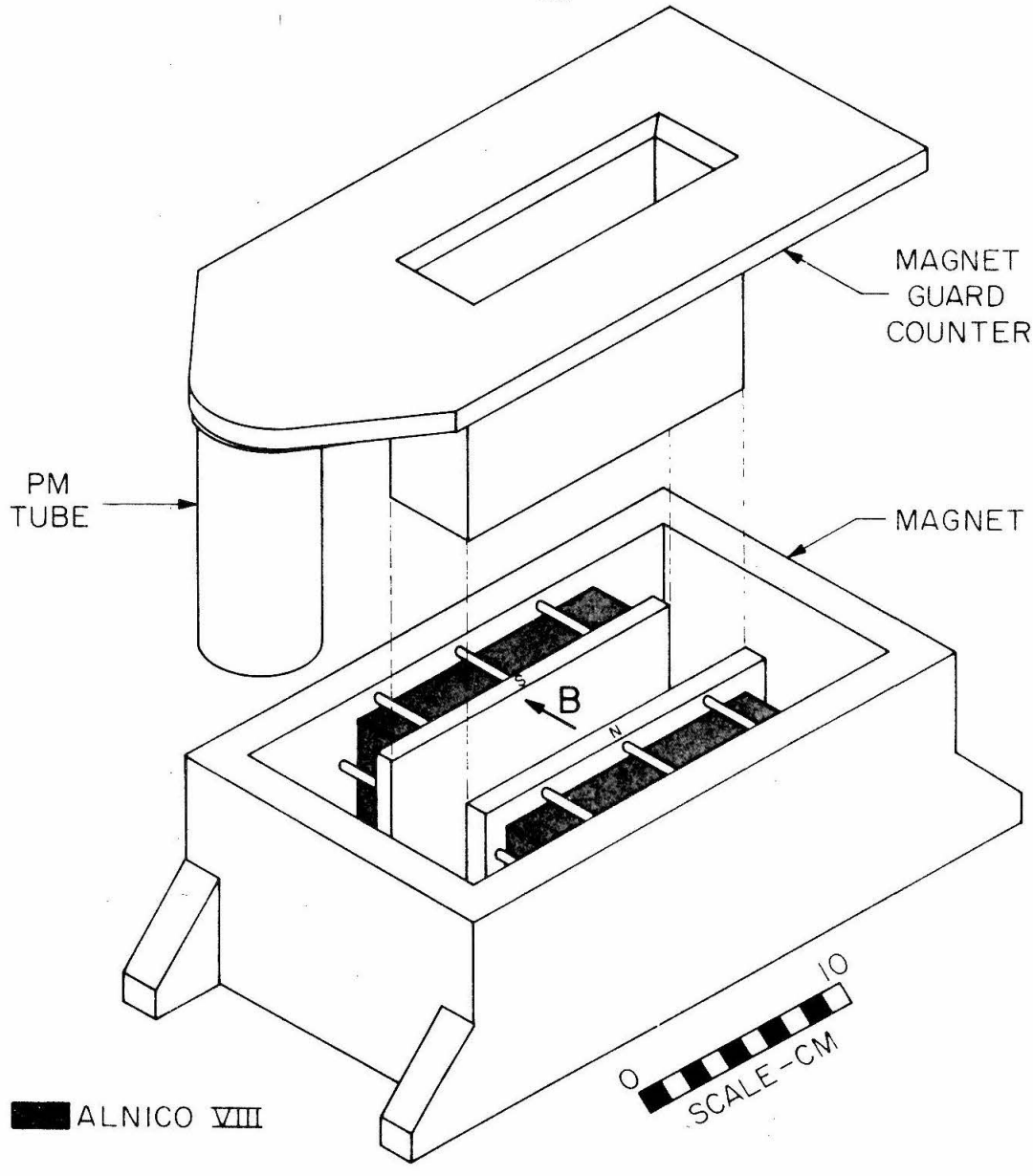

Fig. 2. Exploded view of the magnet and magnet guard counter.

The entire instrument, with the exception of the barometer and 30 silver-zinc batteries, is enclosed in a pressure-tight aluminum gondola during flight. A 0.012-inch aluminum window allows particles incident from above to penetrate the gondola with minimum scattering. The gondola is insulated and the temperature within is maintained above 45°F by thermostatically-controlled heaters. The weight of the instrument package is 370 lbs.

2) Magnet

The analyzing magnet (Indiana General Corp., Valparaiso, Ind.), which is shown in Figure 2, has a 4-cm air gap between 9-cm x 14-cm rectangular pole faces. Alnico 8 permanent magnets are used in a magnet circuit designed to minimize external stray fields. At the position of the photomultiplier tube for the magnet guard counter, for example, the field is less than one gauss. The nominal flux density within the magnet gap is 1000 gauss. The three orthogonal components of the field were measured at one-cm intervals throughout the volume accessible to particles out to a distance 5 cm above and below the magnet. Beyond these points readings were taken at larger intervals. The accuracy of individual field measurements is estimated at about 3 percent, based on the scatter of adjacent readings from a smooth curve and on deviations from

expected symmetries. Figure 3 shows the flux density measured along several vertical paths. Locations are specified in a righthanded coordinate system with the origin at the center of the magnet gap. The z-axis is vertical and positive upward; the x-axis is perpendicular to the pole faces and positive toward the south pole. (This coordinate system is used throughout this thesis. It is shown explicitly in Figure 5). A permanently mounted Hall effect device (F. W. Bell, Inc, Columbus, Ohio) was monitored as part of the check-out procedure before and after each flight; no change in the field strength was ever noted.

The geometrical factor, G, of the detector varies with rigidity due to the effect of the magnetic field on the beam. A Monte Carlo-type calculation determined G at six different rigidities R from 6 to 200 MV. A trajectory was selected at random from a simulated uniform isotropic flux of particles of rigidity R_i incident on counter T1. The trajectory was traced through the detector utilizing the measured magnetic field; it was rejected if it failed to pass through counter T2 or the aperture in the magnet guard counter. This procedure was repeated until 1000 trajectories had been accepted. The geometrical factor at R_i is then

Fig. 3. Magnet flux density in the gap of the analyzing magnet vs. position. The curves represent the field components along three vertical paths through the magnet gap. See Figure 5 and the text on page 14 for a description of the coordinate system employed.

1. Solid curve: x = 0 y = 0.5 cm
2. Dashed curve: x = 0 y = 5.5 cm
3. Dot-dashed curve: x = 1 cm y = 5.5 cm

B_z and B_y for paths 1 and 2 are identically zero and are therefore not shown explicitly in the figure.

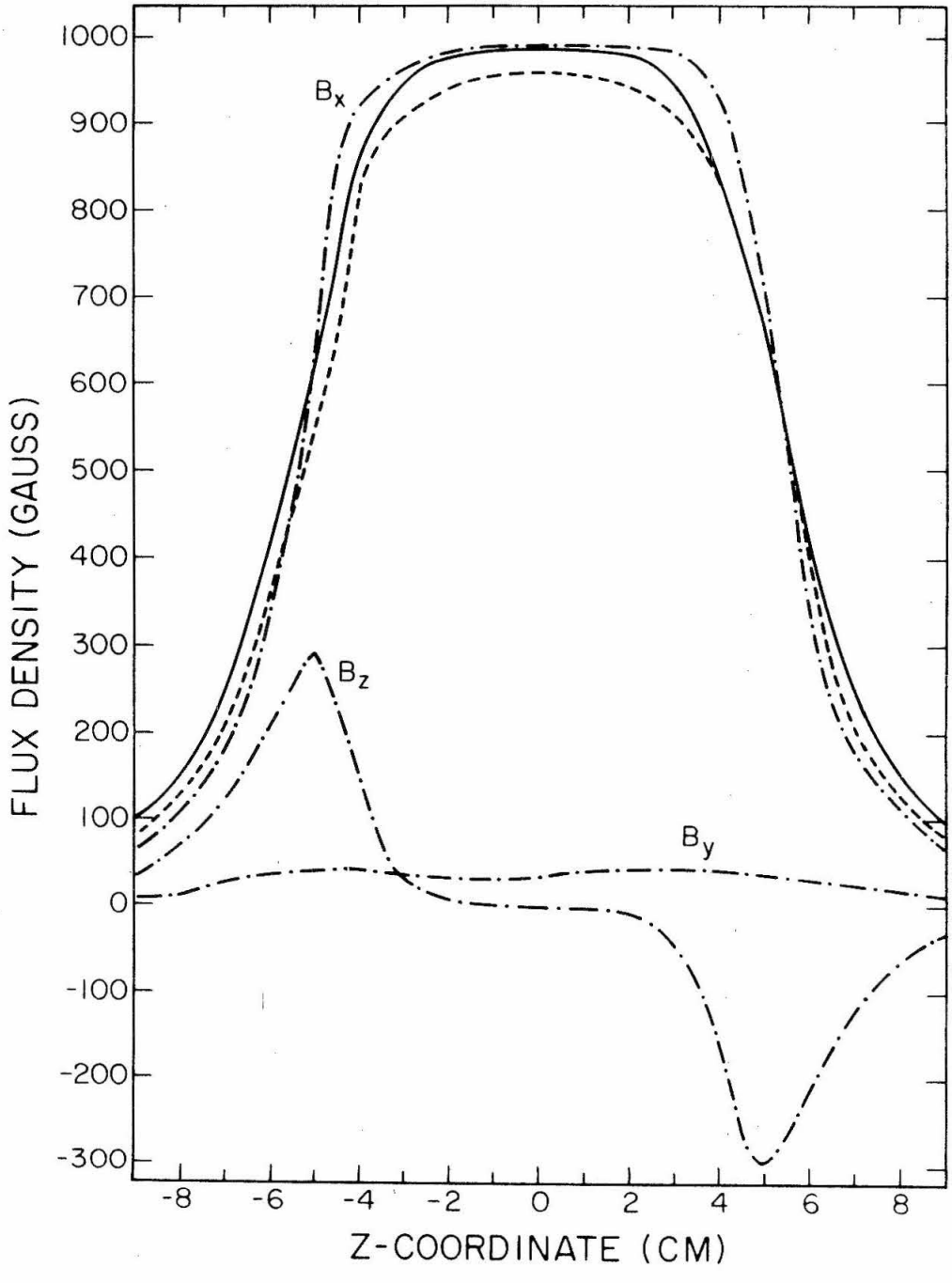
1000
900
800
700
600
500
400
300
200
100
0
-100
-200
-300
FLUX DENSITY (GAUSS)
B_x
B_z
B_y
-8
-6
-4
-2
0
2
4
6
8
Z-COORDINATE (CM)

Figure 3

$$G(R_i) = \frac{1000}{N(R_i)} A\Omega \qquad (1)$$

where A is the area of Tl and Ω is the solid angle out of which the $N(R_i)$ initial trajectories were chosen. The geometrical factor as a function of rigidity is shown in Figure 4. The calculation is accurate to about 3 percent and within this accuracy the geometrical factor is the same for both positive and negative particles.

For the following discussion reference should be made to Figure 5 where the relevant trajectory parameters are shown. We define entrance and exit parameters of the trajectory at convenient planes $z = \pm z_o$, above and below the region of field. The angle η is measured between the trajectory and the y-z plane; α_1 and α_2 are the entrance and exit angles projected in the y-z plane and measured from the negative z-axis. The deflection angle Θ is defined in the y-z plane and is given by

$$\Theta = \alpha_2 - \alpha_1 \qquad (2)$$

Angles measured clockwise are taken to be positive. Since the magnetic field is in the positive x-direction, the deflection angle is then positive for positively charged particles traversing the field in the downward direction.

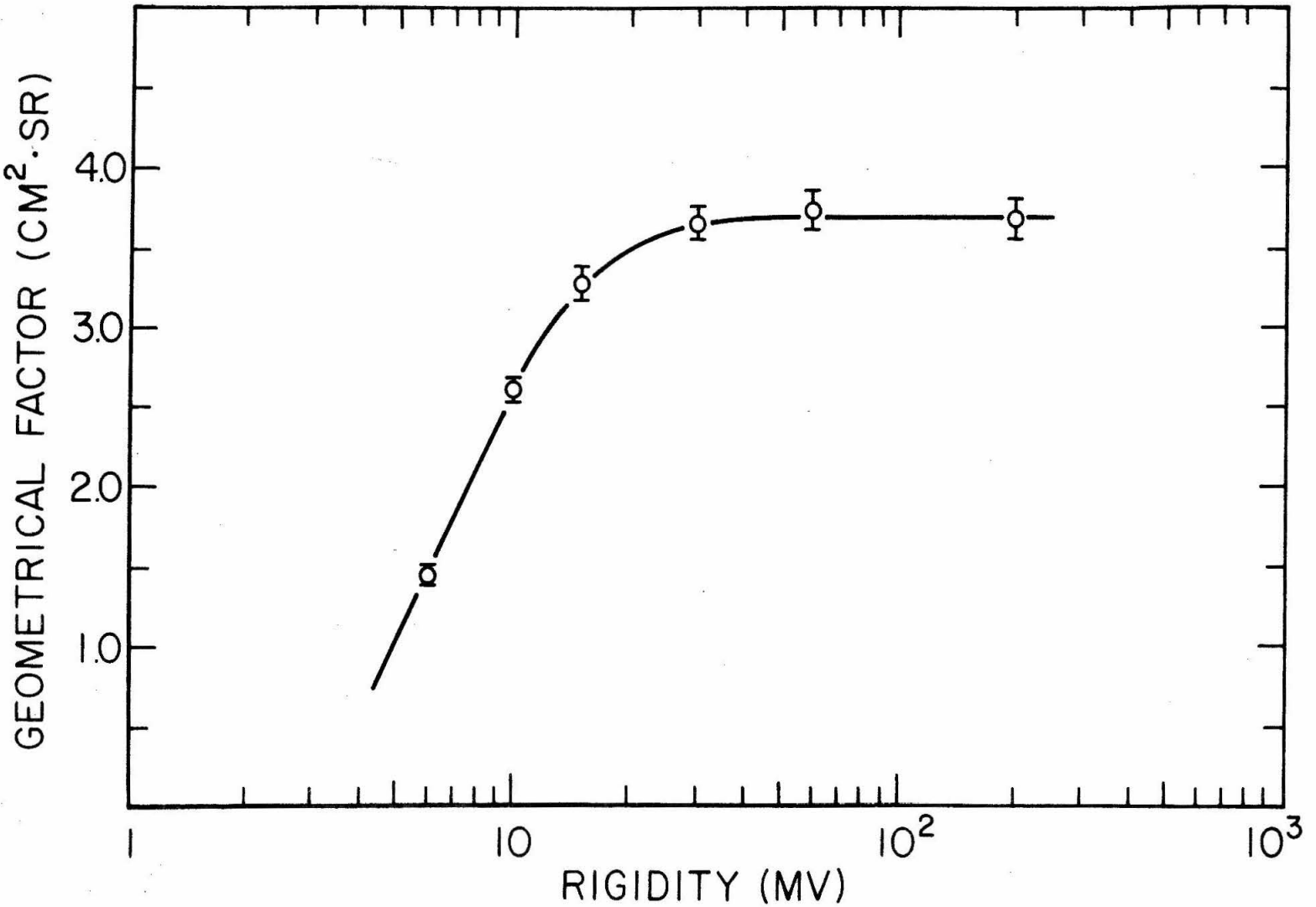

Fig. 4. Geometrical factor of the detector vs. particle rigidity.

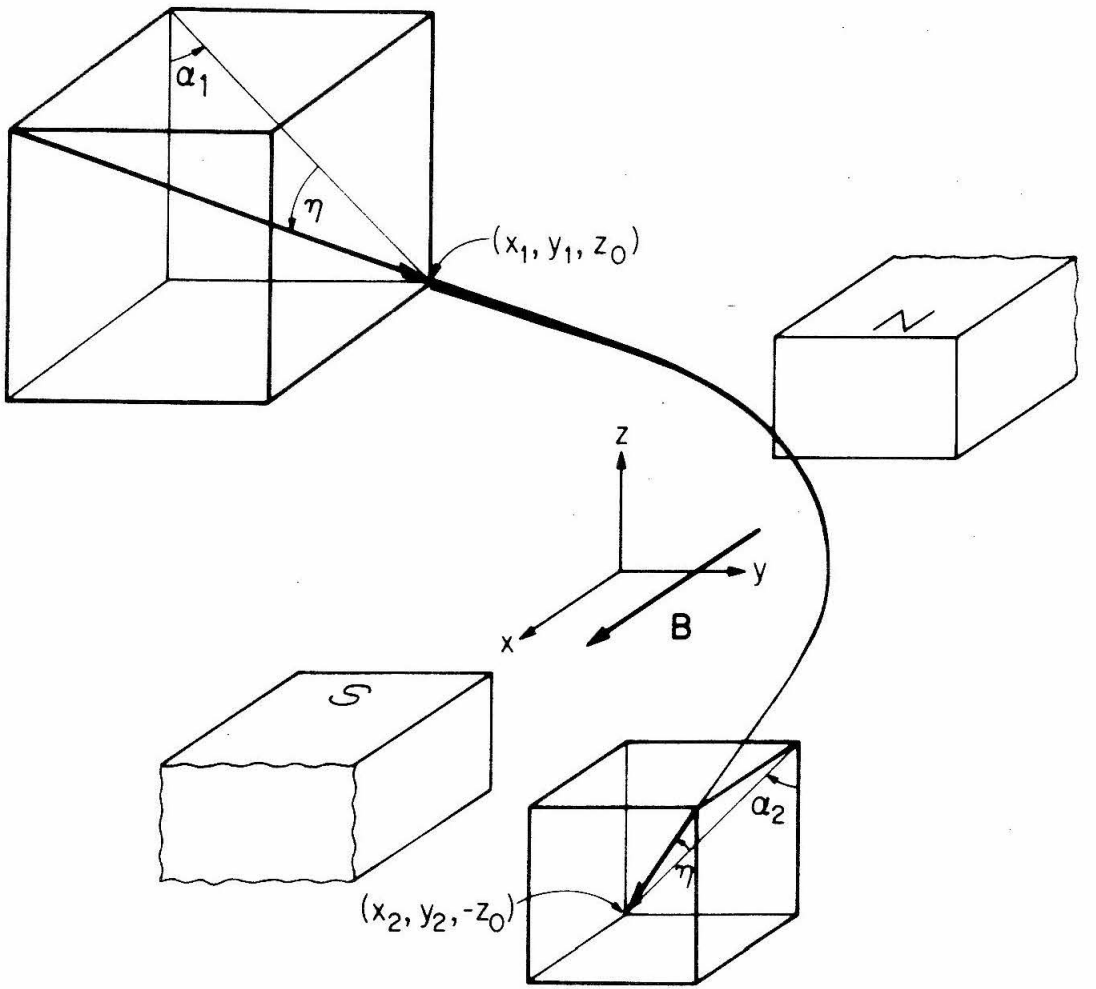

Fig. 5. Schematic view of a particle trajectory through the magnet gap, showing reference coordinate system and trajectory parameters used in the calculation of the particle rigidity.

The deflection of a particle of rigidity R moving through a magnetic field B is given by

$$\theta = \frac{3 \times 10^{-4}}{R} \int B_{\perp} \, dl \qquad (3)$$

where $B_{\perp}$ is the component of B normal to the trajectory and dl is an increment of distance. The deflection is given in radians for R, B, and l in MV, gauss, and cm, respectively. The line integral is evaluated along the trajectory of the particle and is known as the magnetic path, M. If the field and the trajectory of the particle are known, M can be evaluated and eq. (3) solved for the rigidity. In general M will differ along different possible trajectories through the magnetic field. In Figure 6 we show the range of values of R times θ for the random trajectories accepted in the calculation of the geometrical factor. Plotted are the mean value, the rms deviation (solid bar), and the extreme values (dashed bar) for each of the sample populations in that calculation (1000 trajectories for each rigidity). At all points the mean of R x θ is within one percent of 3.55 MV; the rms deviation is typically 2 percent of the mean and contains $\sim$ 70 percent of the sample while the extreme values differ from the mean by about 7 percent. The momentum resolution of the detector is

Fig. 6. Range of trajectory deflection angles in the detector as a function of particle rigidity. The mean value, rms deviation (solid bar), and extreme values (dashed bar) of rigidity x deflection angle are shown for a random distribution of 1000 incident trajectories at each of 6 rigidities.

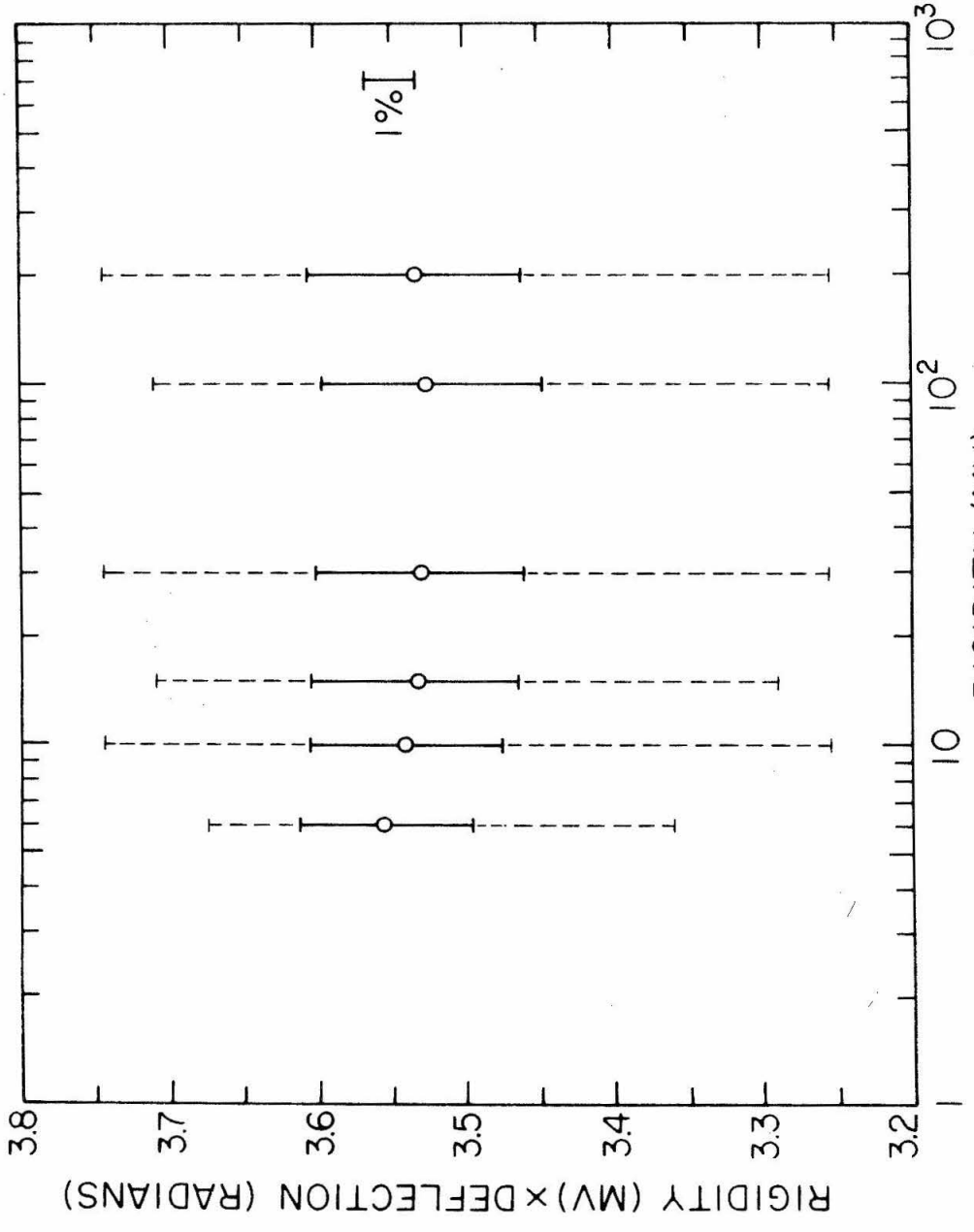
1%
RIGIDITY (MV)
RIGIDITY (MV) × DEFLECTION (RADIANS)
3.8
3.7
3.6
3.5
3.4
3.3
3.2
1
10
10²
10³

Figure 6

$\gtrsim$ 30 percent, FWHM (See Chapter IV, section A). Within this resolution we can approximate eq. (3) by

$$R = \frac{3.55}{\theta} \text{ MV} \qquad (4)$$

with negligible error.

Equation (4) has no dependence on the angle η. Furthermore, the complete sheathing of the magnet by the magnet guard counter eliminates the necessity of protecting against interactions in the pole faces by detailed trajectory reconstruction. This permits us to read out spark locations in the y-z projection only, saving both data storage and detector live time.

3) Scintillation Counters

The two telescope counters T1 and T2 and the nine guard counters are constructed from NE 102 plastic scintillator (Nuclear Equipment Corp., San Carlos, Calif.) and employ RCA 4439 photomultiplier tubes (RCA, Harrison, N. J.). Except for the specially cast magnet guard counter, all of the counters are flat sheets. Individual dimensions are listed in Table 1.

TABLE 1

SCINTILLATION COUNTERS

Designation	Function	Dimensions (Inches)	Connection to photomultiplier
T1	Telescope 1	1/8 x 4 x 7	Lucite light pipe
T2	Telescope 2	1/8 x 4 x 6(a)	Lucite light pipe
Top 1	Top Guard	3/8 x 15 1/2 x 17 1/8(b) with hole 5 x 8 3/8	Direct coupling of photomultiplier to scintillator for all guard counters
Top 2			
Side 1	Side Guard	3/8 x 10 1/2 x 15 1/4	
Side 2		3/8 x 10 1/2 x 15 1/4	
Side 3		3/8 x 10 1/2 x 15 1/4	
Side 4		3/8 x 10 1/2 x 15 1/4	
Side 5		3/8 x 15 7/16 x 22 5/8	
Side 6		3/8 x 15 7/16 x 22 5/8	
MA	Magnet Guard	(c)	

(a) T2 is not rectangular: it is a 4-inch wide strip cut from the center of a 6-inch diameter disc.

(b) Dimensions are for entire top guard; there are two "L" -shaped pieces.

(c) Specially cast; see Figure 2 and text on p. 25.

The photomultiplier tubes for counters T1 and T2 are mounted to lucite light pipes which view the scintillators edge-on. The resolution for minimum ionizing particles is 60 percent, FWHM, for both counters. The photomultiplier of each guard counter is coupled directly to the large flat side of the scintillator near one corner. Optical coupling is made with Dow-Corning 20-057 optical grease (Dow-Corning Corp., Midlands, Mich.). Despite the large size of the exterior guard counters the light collection efficiency is relatively independent of the point of passage of the particle outside a circle of ~10-cm radius centered on the phototube, and is everywhere sufficient to allow conservative discrimination levels to be set.

The magnet guard counter, which is shown in Figure 2, is cast in one piece in order to minimize light loss. The scintillator is 9.4-mm thick except for the area directly covering the pole faces which is 5-mm thick. The upper edge of the gap lining is beveled to aid reflection around the corner. Resolution is 90 percent for perpendicular traversal of a single thickness of the pole face sheath by a minimum ionizing particle. The discrimination level is set to trigger on 99.8 percent of such particles. Particles which trigger counters T1, T2, and C and have interacted or scattered in the magnet material must have passed either

through the top surface or obliquely through the magnet gap lining of MA. In either case, the light output is significantly greater than for perpendicular traversal of the pole face sheath. We therefore assume total rejection of such events.

The presence of the magnet guard counter as one of the elements defining the acceptance cone produces an uncertain rejection zone at the edges. This is due to the finite path length in MA which is required for rejection of the event. This zone is about 0.5-1.0 percent of the total geometrical factor of the instrument. While negligible as an error in the geometrical factor, it represents an additional source of scattering for 0.5-1.0 percent of the accepted electrons. The effect is included in the angular scattering distribution discussed in Chapter IV, section A.

4) Čerenkov Counter

The Čerenkov radiator is a 1-inch thick, 7 5/16-inch diameter disc of ultraviolet-transmitting lucite. It is mounted directly on the face of an EMI 9623 B photomultipler tube (Whittaker Corp., Plainview, N.Y.). This tube is 7 1/2 inches in diameter and has a quartz window. Optical coupling is made with Sylgard 182 resin (Dow-Corning, Midland, Mich.).

Resolution of the Cerenkov counter is 45 percent, FWHM. The discrimination level is set at 25 percent of the output from relativistic muons. The detection efficiency for relativistic particles moving backward through the Cerenkov counter is ~4 percent. During pre- and post-flight checkout, the singles rate of the Cerenkov counter was always <300 counts/sec and probably did not exceed ~1000 counts/sec during flight. Since the resolving time of the triple coincidence is 1 μsec, during flight the probability was less than $\sim 10^{-3}$ that a random pulse in C would accompany a T1 ∧ T2 coincidence.

Even though electrons from 6 to 200 MeV are well above the Čerenkov threshold, at the lowest energies the output and resolution of the counter are degraded somewhat due to increased scattering of the electrons. There is a higher probability of backscattering or stopping in the radiator which result in a shorter effective path for Čerenkov radiation directed toward the phototube cathode. There are no directly applicable experimental data which allow us to determine the effect on our detection efficiency. In the work of Jupiter, Lonergan, and Merkel (48) with 8.0 MeV electrons incident on a 2.4 g/cm^2 aluminum absorber (0.1 radiation length), the backscattered flux and the flux leaving the absorber in the forward hemisphere are respectively 2.7 percent and 77.3 percent of the incident

flux. The other 20 percent have a path length which, because of scattering, is sufficiently long that the particles lose all of their energy by ionization loss. Our Cerenkov radiator is one inch of lucite, which is 2.6 g/cm^2 or 0.06 radiation lengths. With our threshold set at 25 percent of the muon output, a radiating particle need only pass through ~1/4" of lucite in order to have 50 percent probability of detection. Scaling from the data of Lonergan et al. we estimate that all but about 5 percent of the 8 MeV electrons will penetrate 1/4" (.65 g/cm^2) of the lucite. In addition, a scattering electron will have, in general, a longer effective path for radiation of Čerenkov light than the depth to which it actually penetrates. It follows that the detection efficiency for 8.0 MeV electrons is probably $\gtrsim$ 95 percent. Because the exact value is uncertain but appears to be greater than 95 percent even at this unfavorable energy, we have assumed the detection efficiency to be 100 percent over the entire interval from 6 to 200 MeV.

5) Spark Chambers

The two identical wire spark chambers each consist of 4 independent and self-contained modular gaps. Figure 7 shows an exploded view of a single module. The three frame pieces are machined from Supramica 500, a type of bonded mica (Mycalex Corporation of America, Clifton, N.J.).

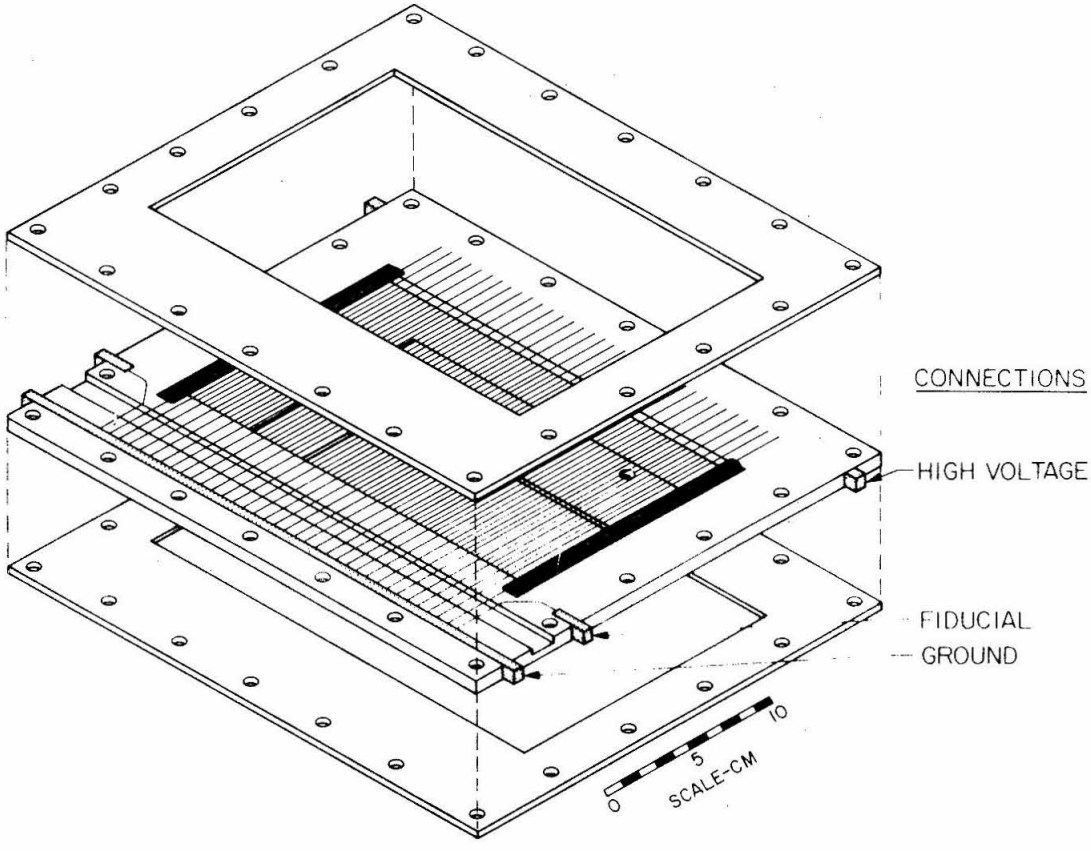

Fig. 7. Exploded view of a spark chamber module.

The upper and lower frames are each 1/8" thick and serve as insulating spacers between adjacent gaps. The central frame determines the spacing of the wire planes, which is .250", and the active area, which is 5" x 9". The high voltage and ground planes employ .0022" diameter silver-coated beryllium copper wire (Little Falls Alloys, Patterson, N.J.). The wires are parallel and evenly spaced 48 per inch and are held in place with Shell 828 epoxy (Shell Oil Co., New York, N.Y.). The 5 edgemost wires within the active area at either end are raised slightly and are looped by a strip of aluminized mylar which extends over the inner edge of the central frame. This feature prevents a high field concentration near the edge which could lead to spurious sparking.

All the wires of a single plane are connected at one end to a buss bar to which external connection can be made. Under the ground plane wires between the buss bar and the active chamber area is a slot which accepts the magnetostrictive pickup. (Use of a magnetostrictive technique for spark chamber readout has been described by Perez-Mendez and Pfab (49)). As the pickup we use a .004" x .009" ribbon of the magnetostrictive material Remendur (Wilbur B. Driver Co., Newark, N.J.) which is held near the wires of the ground plane by an aluminum "wand". The wand slips into the module frame as an independent sub-assembly. The

wand and ribbon are insulated from the chamber wires by a .001" layer of mylar. The current pulse from a spark in the chamber passes over the wand inducing a mechanical deformation in the ribbon. The mechanical pulse travels away from the point of origin at the speed of sound in Remendur, which is 5.3 cm/μsec at room temperature. At each end of the ribbon rubber pads damp the pulses, preventing reflections. Near one end the ribbon threads a small 200-turn pickup coil. Small bias magnets produce a magnetic field in the ribbon at the coil. Passage of the mechanical pulse induces a voltage signal in the coil by the inverse magnetostrictive effect.

Two fiducial wires, which carry pulses each time the high voltage is triggered, pass over the wand outside the chamber wires, one near either end. The quantity which is measured is the time delay between the arrival at the pickup coil of the nearer fiducial pulse and the subsequent spark pulse. Since the velocity of propagation of the pulses is known, the distance between the first fiducial wire and the wire carrying the spark current may be easily calculated. With this technique all spark location measurements are made relative to a standard fixed in the chamber. Furthermore, by separating the pickup coil and the nearer fiducial wire sufficiently, the fiducial pulse will not arrive at the coil until all RF noise from the spark has

disappeared, and hence the timing circuitry need not be noise-immune. The presence of the second fiducial provides a known constant distance with which to monitor changes of the propagation velocity due to temperature or other effects. It also performs a check of the timing and digitizing circuitry.

After all wires have been attached and all electrical connections made, the upper and lower frame pieces are epoxied to the central piece. The four modules of each chamber are mounted in pairs, with their high voltage planes back to back, on the top and bottom of a 4.25"-high open aluminum box. The gas volume is closed off by 0.5-mil mylar - 0.5-mil aluminum laminated foils on the top and bottom of the chamber. The gas used is standard "spark chamber neon", which is 90 percent neon and 10 percent helium. A 2 percent ethanol admixture acts as a quenching agent. During flight gas flows continuously through the chambers at a rate of 0.25 ml/sec and is exhausted into the gondola volume.

The typical efficiency for detection of a single charged particle is 96 to 98 percent in each gap. During some flights a few of the modules developed edge sparks which did not, however, seem to affect the efficiency of sparking at the trajectory location. The distribution of the deviation of the measured spark location from the true

trajectory is approximately gaussian with a standard deviation

$$\sigma_\ell \simeq .008" \qquad (5)$$

This excellent spatial resolution, which is less than the wire spacing, is the result of the magnetostructive read-out, which automatically indicates a mean location, weighted by the relative currents, should two or more wires carry the spark current.

The data readout determines the wires which carry spark current. It follows that a consistently undistorted projection of the trajectory requires that the wires of all modules be parallel. The accuracy of the wire alignment is on the order of ± .3 milliradians within a single chamber and about 1 milliradian between the two spark chamber boxes. The spark chambers and the magnet are mounted rigidly together so that no shifting can occur after the alignment is made.

B) Electronic system

1) Overall description

Figure 8 shows the general block diagram of the electronics system. Data collection is broken up into 16-minute cycles each of which consists of a 15-minute segment called Phase A followed by a 1-minute segment called Phase B.

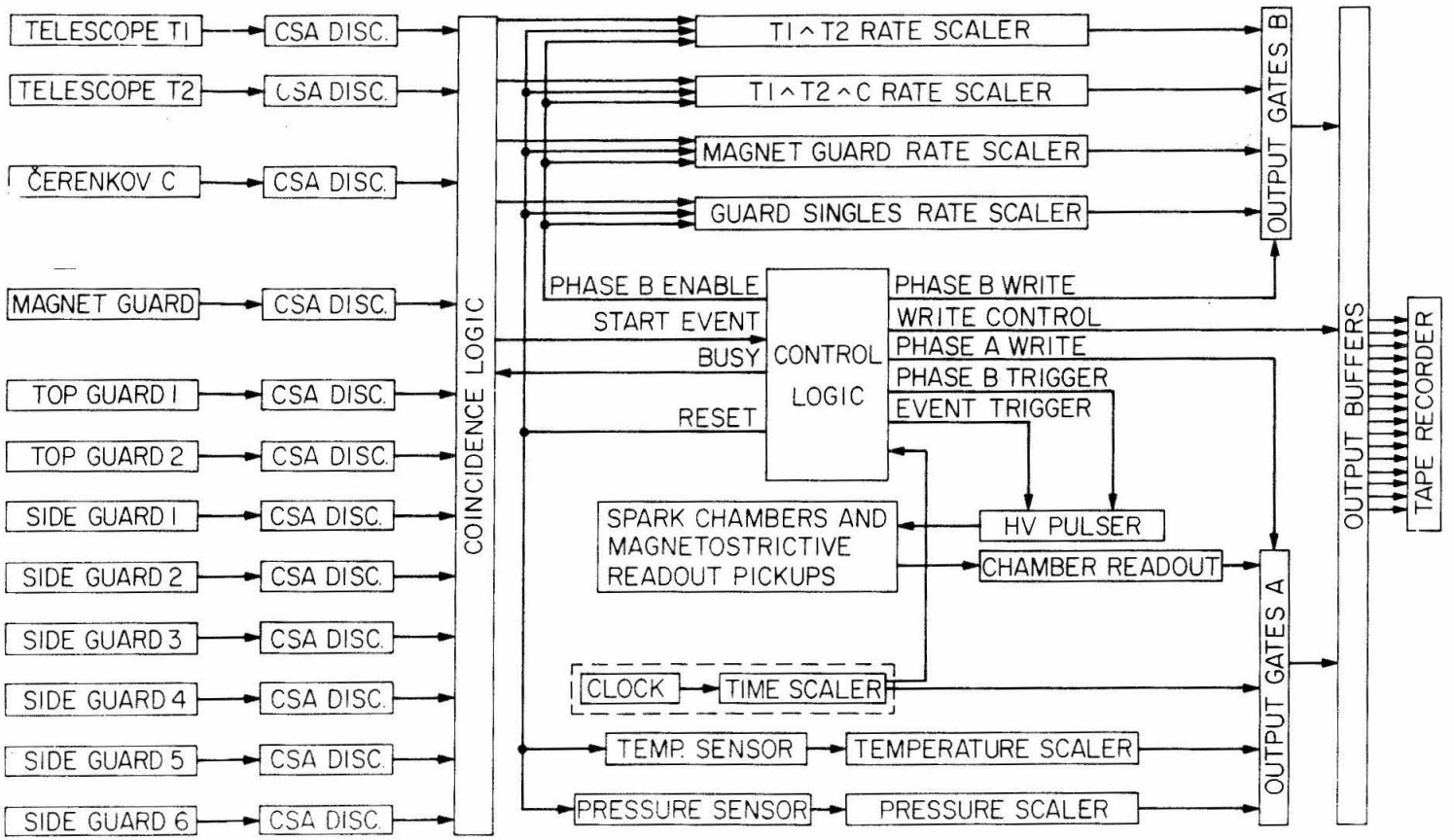

Fig. 8. Electronic block diagram.

CSA DISC = charge sensitive amplifier and discriminator.

Dashed line indicates components enclosed by spark noise shield.

During phase A, a triple coincidence of counters T1, T2, and C, unaccompanied by a pulse in any of the guard counters, triggers the high voltage pulsers and initiates the data readout cycle. A busy signal blocks the coincidence during the 350 milliseconds required to process the event. During the first 12 μsec all noise sensitive circuitry is held in the reset state. During the subsequent 1000 μsec the spark locations, atmospheric pressure, and gondola temperature data are digitized. Only the location of the spark nearest the first fiducial is stored. The presence of subsequent sparks (not including the far fiducial pulse) is indicated by a "Multiple Spark Indicator" (MSI) bit. These data, together with the time information, are then stored on 16-channel magnetic tape. The tape recorder runs continuously at 10 inches per minute and holds sufficient tape for a 30-hour flight. During ground testing the data can also be recorded directly on punched paper tape, which allows manual readout.

During phase B the normal coincidence trigger input is blocked. After sufficient time is allowed to finish recording any preceding event, a trigger pulse is initiated internally. Since this trigger is not associated with any real particle in the detector, no sparks should occur in the chambers and the digitized location should be that of the far fiducial. In practice a spark chamber gap sometimes

breaks down in random locations, but the fiducial appears frequently enough to provide a check of the digitizing operation.

The time remaining in phase B is used to monitor counter rates. There are 4 rate scalers: T1 ^ T2 double coincidence rate, T1 ^ T2 ^ C triple coincidence rate, magnet guard counter singles rate, and total guard counter singles rate. Throughout phase A these scalers are blocked. At the beginning of phase B they are reset and then count until the end of the one minute period, at which time the accumulated count is recorded on the magnetic tape. The rates are monitored in order to check possible counter malfunction, to detect variations in background radiation which might be caused, for example, by solar flares, and to determine detector dead time due to the guard counters. By blocking the spark chamber trigger input, the necessity for shielding the scalers from spark generated RF noise is eliminated. Only the clock and time scaler must be shielded, which is simple since no fast signals are involved. The clock, which provides the timing for the Phase A-Phase B cycle, is a Bulova Accutron.

Total power consumption of the electronics system is fourteen watts. When the heaters are all on an additional 80 watts is dissipated in the gondola. Power is supplied by 30 silver-zinc batteries (Yardney Electric Corp., Los

Angeles, Calif.) and 4 nickel-cadmium batteries (Gould, St. Paul, Minn.). The battery packs provide voltages between -6v and +30v. High voltages for the photomultiplier tubes and spark chambers are produced by DC-DC converters (Crestronics, Crestline, Calif., and Mil Associates, Hudson, N.H.).

2) High voltage pulsers

A 4.5 kilovolt pulse is applied to the spark chamber by pulsers utilizing KN 22 krytron tubes (E. G. & G., Inc., Salem, Mass.). There are eight pulsers, each one of which drives a single module and its associated fiducial wires. The pulser circuit and network are shown in Figure 9. The resistor R in parallel with the spark chamber module CM is used to adjust the decay time of the applied pulse for optimum performance. Too low a value causes sparking efficiency to decline while too large a value produces increased spurious breakdown. Typical values vary between 200 and 600 Ω. The value of the capacitor resistor chain in the fiducial lines is chosen to give magnetostrictive pulses approximately equal in amplitude to average spark discharge pulses.

The pulsers are all triggered by a single avalanche transistor-pulse transformer circuit which is itself directly triggered by the output of the coincidence circuit.

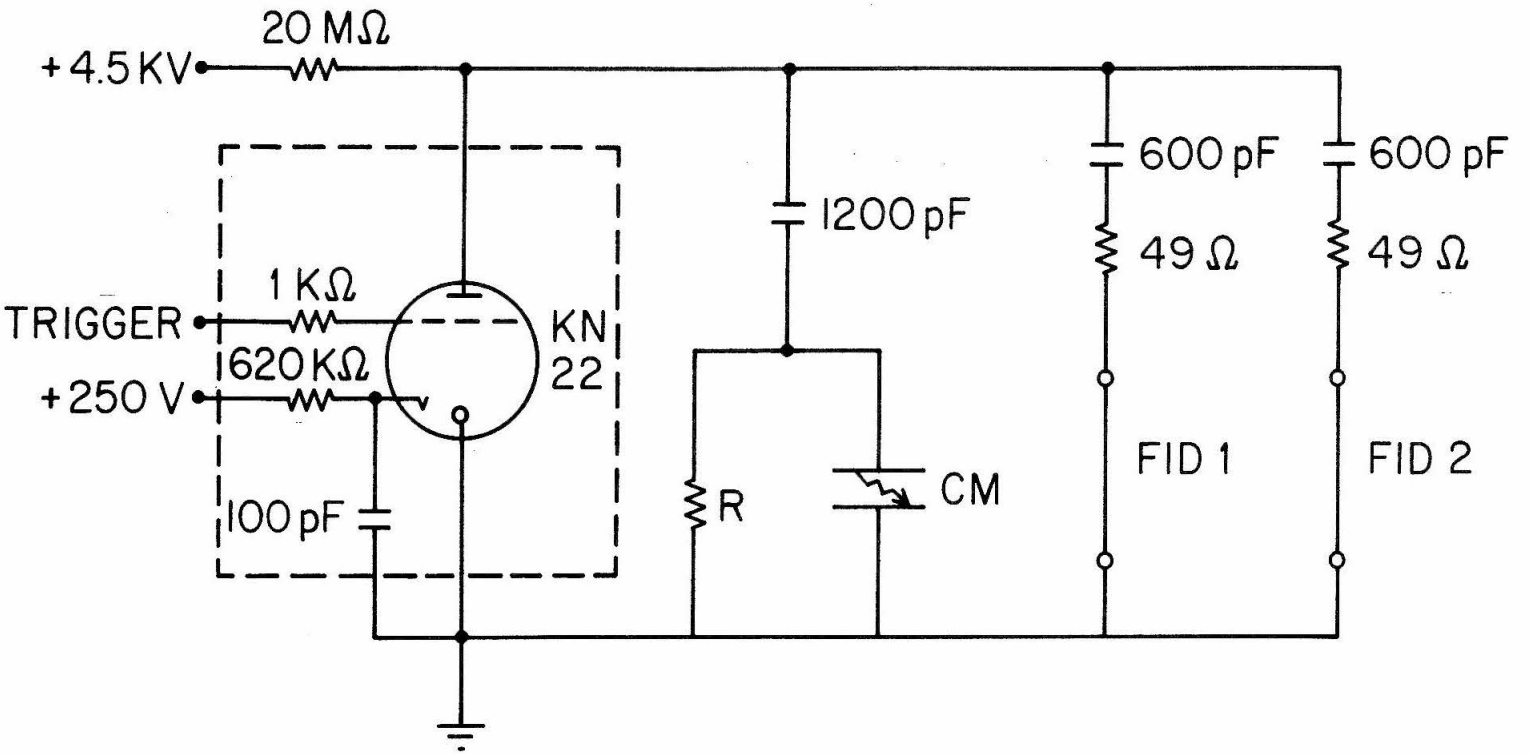

Fig. 9. High voltage pulse network.

CM = spark chamber module.

R = adjustable resistor.

FID1 & FID2 = fiducial wires.

The 10-90 percent risetime of the HV pulse at the spark chamber is 30 nsec. The total delay from passage of the particle to appearance of the high voltage pulse is about 275 nsec which is divided as follows:

Photomultiplier Tubes	100 nsec
Coincidence Circuitry	60 nsec
Avalanche Circuit	80 nsec
Pulser	35 nsec
	275 nsec

3) Spark chamber readout

The output of the magnetostrictive readout pickup coil is a sequence of pulses corresponding to the two fiducials and whatever sparks may have occurred in the spark chamber gap. These pulses have the shape shown in Figure 10A(a). Despite being relatively broad (the central lobe is about 400 nsec wide, equivalent to 2 mm on the magnetostrictive ribbon). The symmetry and reproducibility of the pulse shape allow the separation between pulses to be determined to better than 50 nsec. Our method is similar to that of Kirsten, Lee, and Conragan (50). After the small signals from the coil are amplified by a preamplifier mounted directly on the wand, they go to the so-called "magnetostrictive discriminator." Here the sequence of pulse transformations shown in Figure 10A takes place.

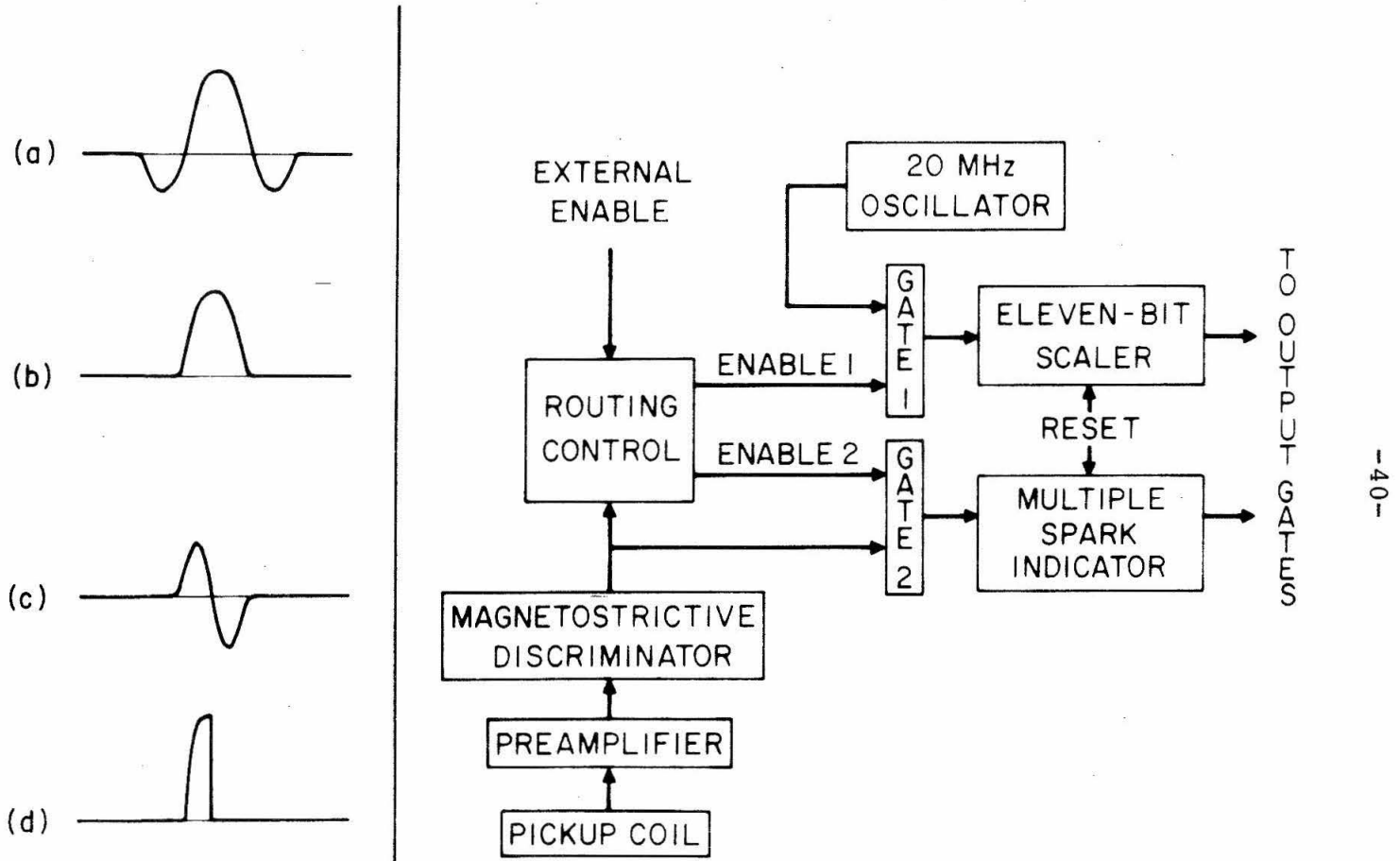

A. Pulse shaping

B. Block diagram of spark chamber readout electronics.

Fig. 10. Magnetostrictive spark chamber readout.

The input pulse, (a), first has its outer lobes clipped, (b), after which it is differentiated, (c). The output (d) of the zero-crossing discriminator which follows is a pulse with a relatively slow leading edge (100-150 nsec rise time) but a fast trailing edge (10 nsec fall time). The trailing edge corresponds to the zero crossing of (c) and hence to the peak of the input pulse (a). This edge is used in the subsequent routing and digitizing electronics, a block diagram of which is shown in Figure 10B. This part of the circuitry is similar to the commercially available Model 180 Multiple Time Digitizer (LeCroy Research Systems Corp., Elmsford, N.Y.) but has been adapted to our special requirements. Each module feeds into a single 11-bit scaler. Initially the scaler is reset and gates 1 and 2 are blocked. The arrival of the first pulse (the near fiducial) opens gate 1 which allows pulses from the 20 MHz oscillator to reach the scaler. Scaling continues until the arrival of a second pulse again blocks gate 1. A third pulse opens gate 2 and a fourth sets the multiple spark indicator. Any subsequent pulses have no effect. The indicator bit is thus set only if 2 or more pulses occur in the gap. The external enable allows digitization only in the 75 μsec immediately following an event. This protects against random noise

pulses setting the multiple spark indicator during the long (240 msec) period required to record the event.

The spark information recorded for each module is

1. the time delay between the first and second pulses on the magnetostrictive ribbon, digitized to 50 nsec (equivalent to .25 mm), and
2. an indication if more than one spark occurred in the gap.

III. BALLOON FLIGHTS

The data reported in this thesis were derived from three high-altitude balloon flights launched from Fort Churchill, Manitoba, on July 16, July 21, and July 29, 1968 (Universal Time). The flights are designated C1, C2, and C3, respectively. Relevant flight information is summarized in Table 2.

Figure 11 shows the trajectories of the three flights. Invariant latitude contours, calculated from the internal field only (51), are included to show the trajectories in the geomagnetic field.

In Figure 12 we show the altitude curves for the flights. In each case the launch was timed so that the detector would pass through the level at 100 g/cm^2 residual atmosphere after the evening transition to the low nighttime geomagnetic cutoff (see Chapter IV, section E and Chapter V, section A); the evening transition occurs at about 18:00 local time (00:20 UT). The float altitude during the nighttime interval stayed within the range 2.2-2.6 g/cm^2 residual atmosphere for all three flights.

In Figure 13 we show the daily average of the hourly count rate for both the Churchill (52) and the Mount Washington (53) neutron monitors, as well as the daily average of the 3-hour range indices for the

TABLE 2

BALLOON FLIGHTS

Flight Number		C1	C2	C3
Launch Date (1967) (a)		July 16	July 21	July 29
Launch Time (a)		00:27	01:04	01:31
Reach 100 g/cm^2 (a)		01:32	02:00	02:42
Begin Float (a)		03:49	04:09	04:53
Terminate (a)		17:15	19:18	01:11 (July 30)
Floating Depth (g/cm^2) (b)		2.2-2.6	2.2-2.6	2.1-3.4
Total Sensitive Time at Float (Min)		625	695	932
End Night Interval (a) (c)		09:09	09:45	10:45
Average Floating Depth--Night (g/cm^2) (c)		2.45	2.5	2.35
Total Sensitive Time at Float--Night (Min) (c)		251	254	265
K_p (d)	Total Flight	2+	2-	1+
	Nighttime Only	2	1	1+

Table 2 Continued

Mt. Washington Neutron Monitor (e)	Total Flight	2163	2200	2227
	Nighttime Only	2147	2194	2230
Churchill Neutron Monitor (e)	Total Flight	5857	5942	6025
	Nighttime Only	5861	5921	6003

(a) Universal Time

(b) See Figure 12

(c) For the period included in the nighttime data. For actual transition times see Chapter V, section A.

(d) Mean of three-hour K_p indices during float (54)

(e) Mean of hourly count rate during float (52) (53)

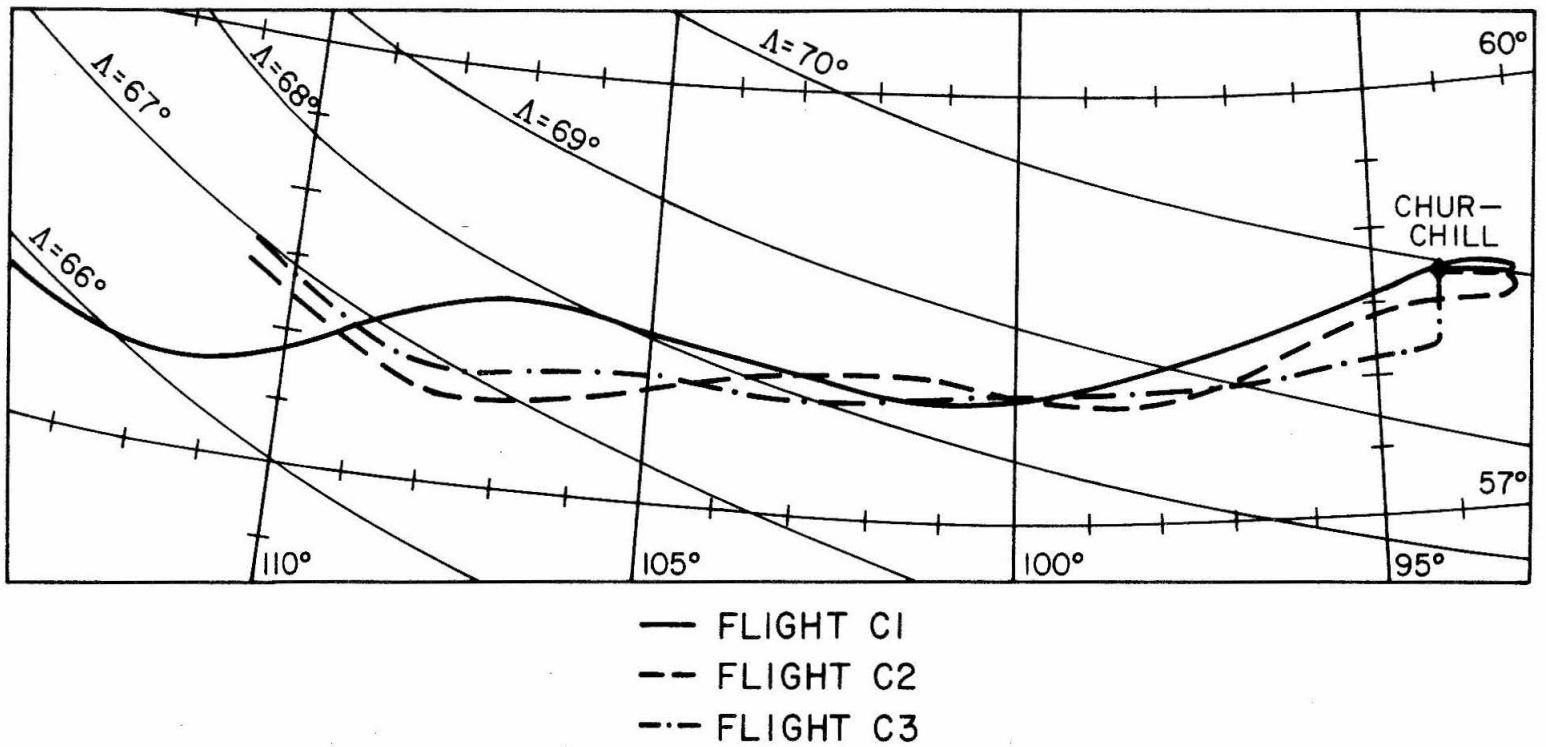

Fig. 11. Trajectories of the balloon flights. Invariant latitude contours are derived from the internal geomagnetic field only (Ref. 51).

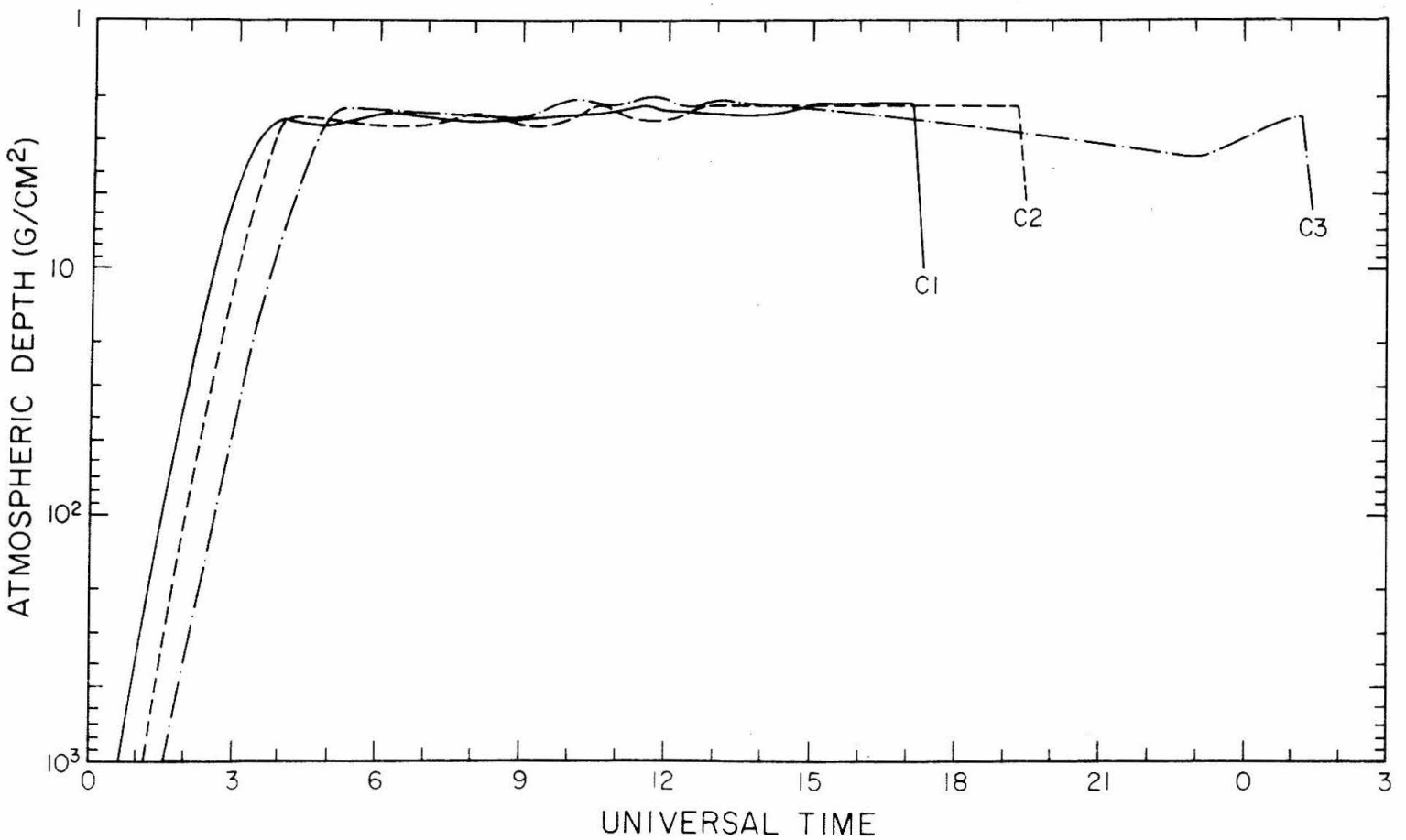

Fig. 12. Altitude curves. The curves are labeled with the flight number.

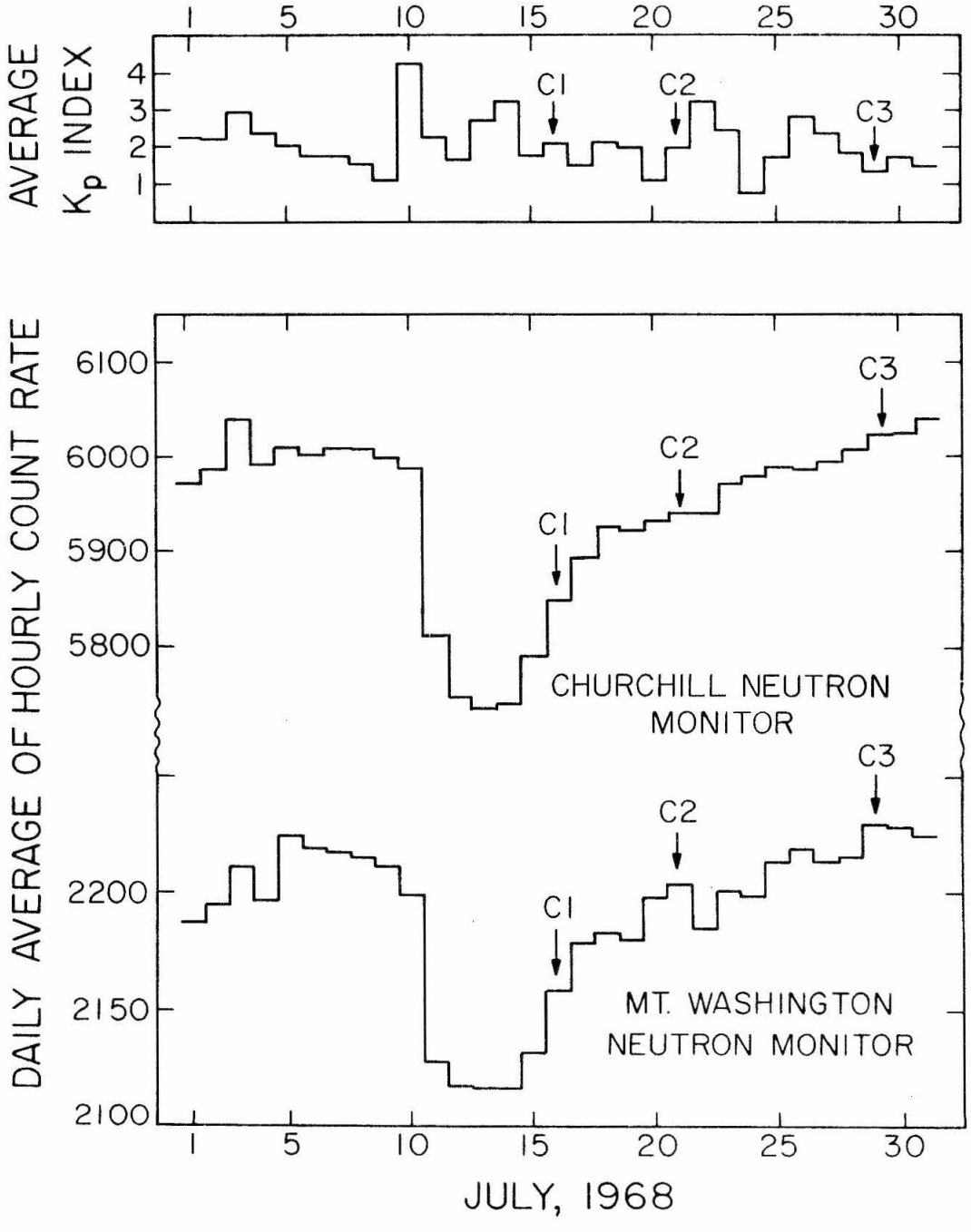

Fig. 13. Planetary magnetic index, K_p, and Churchill and Mt. Washington neutron monitor count rates during July, 1968. The numbered arrows indicate the times of our flights.

planetary magnetic index, K_p (54), for July 1968. All of our flights occurred during or just after the recovery phase following a Forbush decrease. The average hourly count rate of the Churchill neutron monitor was 5857, 5942, and 6025 for flights C1, C2, and C3, respectively. These rates differ among themselves by about 3.2 percent. For comparison, the average neutron monitor count rate during July 1967 was about 4 percent higher than the average rate during July 1968.

The solar proton monitor aboard the Explorer 34 satellite recorded no flux above 30 MeV and only negligible flux (0.2 particles/$cm^2 \cdot sec \cdot sr$) above 10 MeV throughout flights C1 and C3 (55). The same is true for the earlier part of C2, but at 15:00 UT a large short-term increase is evident. The event produced a significant flux of protons above 60 MeV. Activity is also evident in the K_p indices at about the same time and a principal magnetic storm occurred at about 16:00 UT (52). The relationship to our measured data is discussed in Chapter V, section A.

IV. DATA ANALYSIS

A) Detector Resolution

Several effects contribute in determining the magnetic rigidity resolution of our detector. The results of limiting the trajectory measurement to a single plane projection and of using a constant magnetic path approximation have already been discussed in Chapter II. An uncertainty of a few percent is introduced in the rigidity determination by these simplifications. More significant uncertainties at all rigidities are the result of the intrinsic angular resolution of the instrument and/or multiple electron scattering. The intrinsic angular resolution determines the ability of the detector to measure the actual deflection of the particle trajectory. Multiple electron scattering adds a random angular deviation to the deflection due to the magnetic field. It therefore determines how greatly the trajectory deflection angle differs from the angle corresponding to the particle rigidity R according to eq. (4), Chapter II. We shall discuss the errors in terms of the deflection angle Θ, since the error distributions are symmetric in angle. Because the rigidity R is inversely proportional to Θ, the equivalent distributions in R are skewed somewhat toward higher rigidities. Each of the two effects will be discussed

separately. Both will then be combined to give the "true" angular resolution, which corresponds to the ability of the detector to measure the rigidity of a particle.

The discussion in this section and the next uses a number of distributions for which standard deviations are defined. Since it has not been possible to employ self-evident symbols in every case, we have summarized in Table 3 the symbols used for the various standard deviations, together with a short definition for each and the number of the equation where the symbol is introduced. More complete definitions are found in the text.

We consider first the error in the measured deflection angle due to the intrinsic angular resolution of the detector, assuming no scattering. The intrinsic angular resolution depends on the ability of the instrument to define the entrance and exit angles, α_1 and α_2, of the particle trajectory (see Figure 5). It is independent of the rigidity or the species of the particle. Within each spark chamber the trajectory is determined by making a least-squares fit of the measured spark locations to a straight line. With our spark plane arrangement (see Figure 1), the standard deviation σ_s of the determination of the slope ($\tan \alpha$) of the particle trajectory in a single spark chamber is given approximately by

TABLE 3

SUMMARY OF SYMBOLS USED FOR STANDARD DEVIATIONS

Symbol	Definition	Where first used (a)
σ_ℓ	Standard deviation (S.D.) of the measured spark location in a single spark plane	Eq. (5), Ch. II
σ_α	S.D. of the measured entrance and exit angles, α_1 and α_2	Eq. (3)
σ_s	S.D. of the measured entrance and exit slopes, tan α_1 and tan α_2	Eq. (1)
σ_A	S.D. of the measured deflection angle arising solely from the intrinsic angular resolution of the detector	Eq. (4)
σ_ϕ	S.D. of the calculated projected scattering-angle distribution for electrons	Eq. (5)
σ_Θ	S.D. of the measured deflection angle Θ, including electron scattering and the intrinsic angular resolution of the detector	Eq. (7)
σ_ω	S.D. of the measured angle ω (see Figure 18)	Eq. (16)
σ_Δ	S.D. of the measured angle Δ (defined in Eq. (13)	Eq. (16)

(a) Equation numbers refer to Chapter IV unless otherwise indicated.

$$\sigma_s \simeq \begin{cases} \sigma_\ell / r & \text{for good sparks in 4 planes} \\ \sqrt{\frac{3}{2}}\ \frac{\sigma_\ell}{r} & \text{for good sparks in 3 planes} \end{cases} \qquad (1)$$

where σ_ℓ is the standard deviation of the distribution of the measured spark location about the true trajectory position and r is the overall separation within the spark chamber. In this case $r = 5.3"$ and $\sigma_\ell \simeq .008"$ (eq. 5, Chapter II) and hence

$$\sigma_s \simeq \begin{cases} .0015 & \text{for 4 planes} \\ .0018 & \text{for 3 planes} \end{cases} \qquad (2)$$

The relationship of σ_s to the standard deviation σ_α for the incident angle α depends weakly on the value of α within the acceptance cone of the instrument. We shall use a value for σ_α obtained by averaging over the possible trajectories within the acceptance cone. The result, valid for both the entrance and exit angles, α_1 and α_2, is

$$\sigma_\alpha \simeq \begin{cases} .0019 \text{ radians} & \text{for 4 planes} \\ .0022 \text{ radians} & \text{for 3 planes} \end{cases} \qquad (3)$$

The error distribution for α will be approximately gaussian, since the distribution of the measured spark location for any spark plane is approximately gaussian. The deflection angle Θ is the difference of α_2 and α_1 (eq. (2), Chapter II). It follows that the standard deviation σ_A for the error in the measurement of the deflection angle due solely to the intrinsic angular resolution of the detector is

$$\sigma_A = \sqrt{\sigma^2_{\alpha_1} + \sigma^2_{\alpha_2}} \simeq \begin{cases} .0027 \text{ radians} & \text{for 8 planes} \\ .0029 \text{ radians} & \text{for 7 planes} \\ .0031 \text{ radians} & \text{for 6 (3+3) planes} \end{cases} \qquad (4)$$

For data analysis, events are divided into 3 categories:

1. Those events where all 8 spark planes define the trajectory, referred to as "perfect" events;

2. Those events where a single spark plane in one or both spark chambers malfunctioned (registering either no spark or a spark off the trajectory defined by the other 3 planes), referred to as "one-error" events; and

3. Those events where more than one spark plane in one or both spark chambers malfunctioned, referred to as "multiple-error" events. Only the first two categories are used for the determination of particle rigidity. (See section B for more details on event selection criteria.)

In Figure 14 we show the measured distribution of deflection angles for a mono-energetic beam of positrons of 800 MeV from the California Institute of Technology Synchrotron. At this energy the deflection resolution is determined primarily by the intrinsic angular resolution of the detector. Also shown is a gaussian distribution for which $\sigma = .0028$ radians. The agreement of the measured distribution with eq. (4) is seen to be quite good for both "perfect" and "one-error" events.

We shall consider now the effect of multiple scattering, ignoring the intrinsic angular resolution of the detector. The scattering which affects the deflection measurement occurs principally at the wire spark chamber planes and foil covers immediately above and below the magnet. In Figure 15 we show (curve 1) the distribution of the projected scattering angle ϕ calculated for electrons of momentum p according to the theory of Moliere (data from ref. 56). Both the differential distribution, $dN/d\phi$, normalized by dividing by p, and the integral distribution, $N(>\phi)$, are plotted versus $p\phi$. Plotted in this way curve 1 can be used for all electron momenta above a few MeV/c. It follows that if k is the standard deviation of the distribution as plotted, then the standard deviation σ_ϕ of the projected scattering-angle distribution is

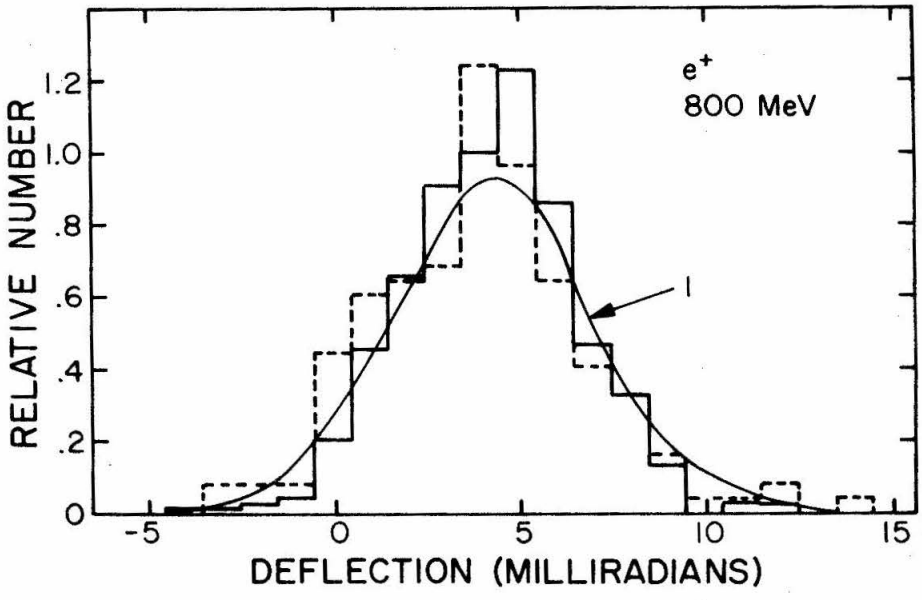

Fig. 14. Distribution of measured deflections in an 800 MeV positron beam. "Perfect" events (solid histogram) and "one-error" events (dashed histogram) are plotted separately. Curve 1 is a gaussian distribution for which σ = .0028 radians. The distributions are normalized to the same total number of events. From eq. (4), Chapter II, the expected deflection angle is .0045 radians.

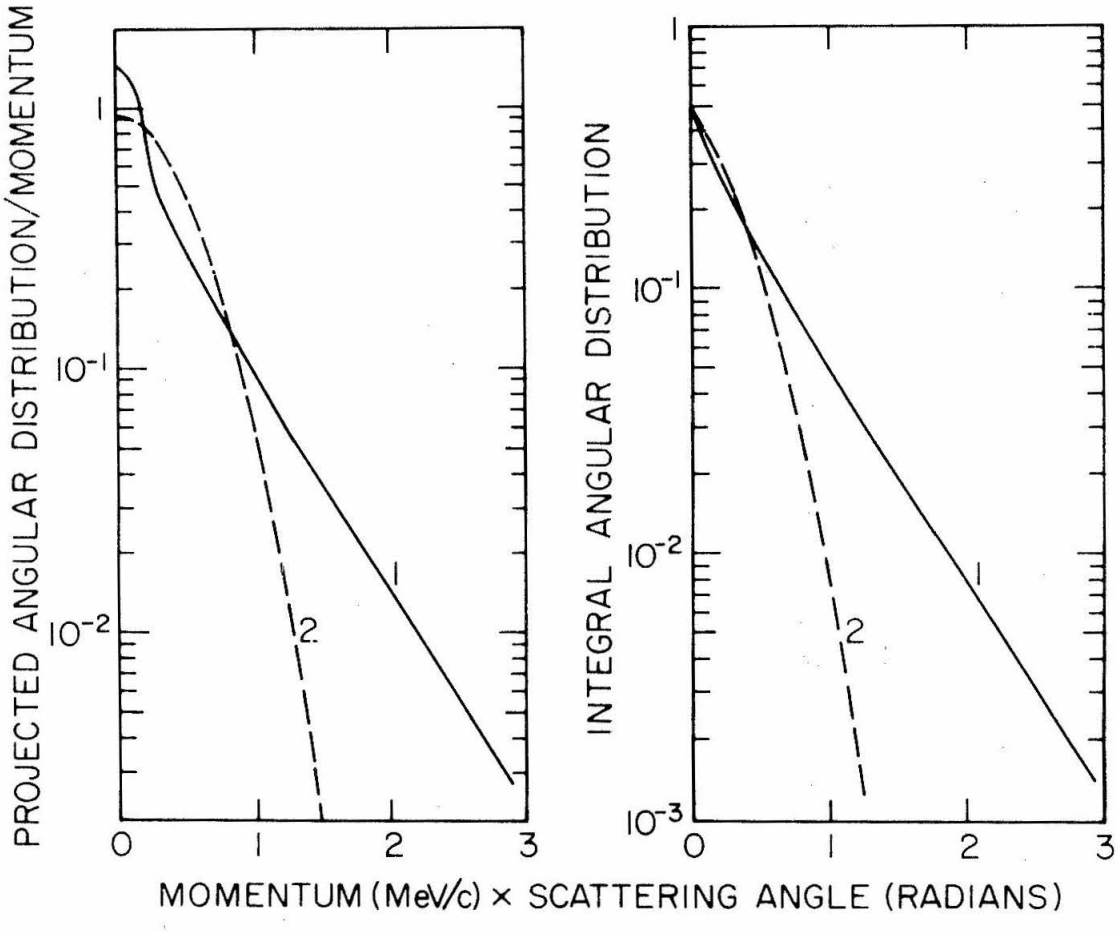

Fig. 15. Calculated electron scattering-angle distribution. Curve 1 is the angular distribution of the projected scattering angle. Plotted as above, the curve is valid for all electron momenta above a few MeV/c. Curve 2 is a gaussian distribution with σ = .42 MeV/c radians. Only one sign of the scattering angle is shown since the distribution is symmetric about zero.

$$\sigma_\phi = \frac{k}{p} \tag{5}$$

valid for all electron momenta of interest. Since p = R, the electron rigidity, we can substitute for p its value from eq. (4), Chapter II, to obtain

$$\sigma_\phi = \frac{k}{3.55}\,\theta \tag{6}$$

i.e., the standard deviation of the projected scattering-angle distribution is directly proportional to the "true," or magnetic, deflection angle θ. Curve 2 in Figure 15 is a gaussian distribution with a standard deviation of .42 $\frac{\text{MeV}}{c}$ radians. At $p\phi$ = .42 $\frac{\text{MeV}}{c}$ radians the integral distributions of curves 1 and 2 are equal. For calculating the deflection resolution P of the detector we shall use this gaussian curve as an approximation to the projected scattering-angle distribution. Since P for the distribution is defined with the full width at half maximum, the true scattering-angle distribution would give a deceptively small value due to its high, narrow maximum at small angles. (Fifty percent of the particles have scattering angles greater than the value at half maximum for the true scattering-angle distribution; with the gaussian approximation only 30 percent have larger scattering angles.) The

long large-angle scattering tail will be taken into account in the trajectory consistency checking (see section B).

We can now derive the deflection resolution by combining the independent error distributions due to the intrinsic angular resolution and to multiple scattering. Using the gaussian approximation for the latter, we obtain the standard deviation σ_θ of the deflection measurement for electrons by directly combining eqs. (4) and (6) to get

$$\sigma_\theta = \sqrt{\sigma_\phi^2 + \sigma_A^2} \simeq \sqrt{(.12\theta)^2 + (.003)^2} \qquad (7)$$

We have used here $k = .42 \frac{\text{MeV}}{c}$ radians and a value for σ_A appropriate for both "perfect" and "one-error" events. The deflection resolution P, FWHM, is then

$$P = \frac{2.36\ \sigma_\theta}{\theta} \simeq \sqrt{(.18)^2 + (.0045/\theta)^2} \qquad (8)$$

Equation (8) also applies for cosmic-ray nuclei, since θ is very small for nuclei above the Čerenkov threshold and the scattering term (the first term under the radical sign) is therefore negligible. In Figure 16 we show σ_A/θ, σ_ϕ/θ, σ_θ/θ, and the resolution P. The measured values (triangles) for the resolution were obtained in a mono-energetic positron beam at the California Institute of Technology Synchrotron. The deflection resolution P, as defined

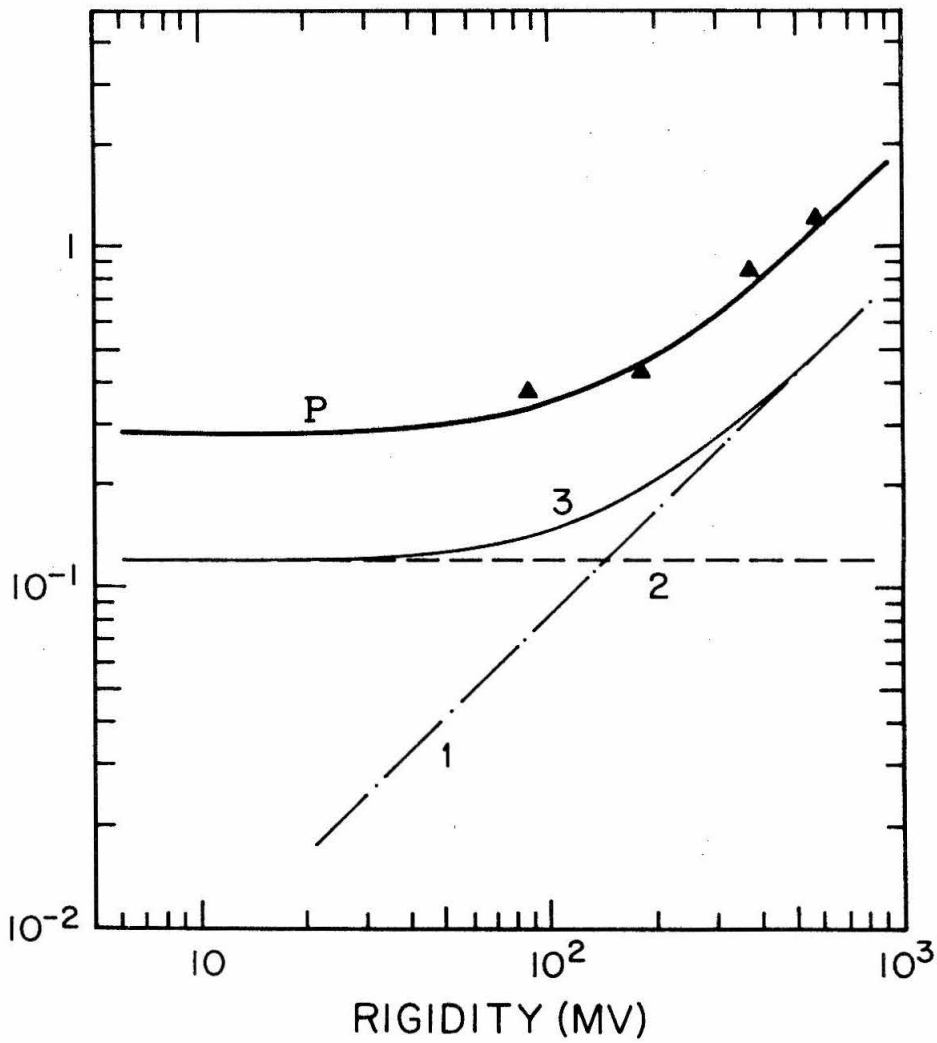

Fig. 16. Deflection resolution, P, FWHM, of the detector Data points (triangles) were measured in a mono-energetic positron beam. Curves 1, 2, and 3 are σ_A/Θ, σ_ϕ/Θ, and σ_Θ/Θ, respectively.

above, is derived for the distribution of measured deflections about the "true," or magnetic, deflection angle which corresponds to the rigidity of the particle according to eq. (4), Chapter II. Thus P is a direct measure of the accuracy to which the detector can determine the particle rigidity.

B) Event selection and detection efficiency

Because all anti-coincidence counters are active and no interactions are involved in particle identification, events accepted for analysis are selected purely on the basis of good chamber operation and a self-consistent trajectory determination. The event analysis can be divided into 3 steps: 1. determination of the trajectory in each spark chamber; 2. calculation of the deflection angle; and 3. checking whether a particle of the derived rigidity could travel a path consistent with the trajectory determined by the spark chambers.

Step (1): Initially each spark chamber box is examined independently. In each chamber a least-squares fit of the measured spark locations is made to a straight line. Only those events are accepted where 3 or 4 of the gaps in each spark chamber show sparks within 2.5 mm of the best-fit straight line. Should one or more gaps of a 4-gap fit not fulfill this criterion, the spark farthest

from the fitted trajectory is eliminated and a 3-gap fit is made. The average deviation of all gaps included in the final fit may not exceed 1.25 mm or the event is rejected. The mean deviation is generally less than 0.3 mm but tends to be slightly greater for trajectories away from the vertical. It is also required that the trajectory fit be within the acceptance cone of the detector.

The original intention was to ignore those gaps where the multiple spark indicator (MSI) bit was set (see Chapter II, section B). During flight several spark planes developed persistent spurious sparks at the edge away from the pick-up coil. Although these edge sparks did not seem to prevent registration of the trajectory spark location, they set the MSI, and thus made it necessary to ignore this bit. The effect is to increase the potential chance of fitting an incorrect trajectory in some ambiguous events or of failing to recognize a multiple particle event. The trajectory consistency checks, described in step (3) below, however, greatly decrease the probability of accepting an incorrect trajectory. Furthermore, a careful examination by hand for possible incorrect trajectory assignments or multiple particle events showed very few questionable events (much less than one percent). We therefore feel that ignoring the MSI bit has not significantly affected our results.

Step (2): The deflection is calculated according to eq. (2), Chapter II, and is simply the difference of the entrance and exit angles. The particle is assigned a rigidity according to eq. (4), Chapter II.

The alignment for zero deflection is determined by means of the cosmic-ray protons and alpha particles, which greatly outnumber other particle species triggering the detector and, in addition, are confined to small deflection angles. In Figure 17 we show the distribution of measured deflection angles Θ, for $|\Theta| \leq .010$ radians, measured during the nighttime period of flight C3. The criteria of step (3) below have been applied to these data. We have estimated the rigidity spectrum of cosmic-ray nuclei above the detector threshold by adjusting the observed spectra of Ormes and Webber (57) (58) according to the Mt. Washington neutron monitor count rate measured during the flight. Curves 1 and 2 in Figure 17 are obtained by folding the estimated spectrum with an angular resolution for which $\sigma_\Theta = .0027$ radians and $\sigma_\Theta = .003$ radians, appropriate for "perfect" and "one-error" events, respectively (eq. (4). We conclude from the good agreement of the measured and calculated distributions that our deflection zero is accurate to within better than .0005 radians. Distributions measured during other flights are similar.

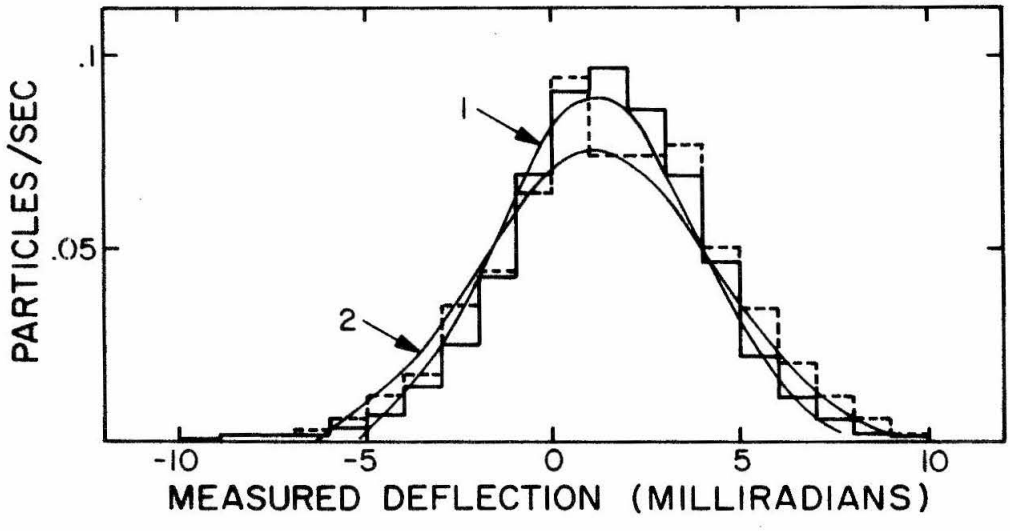

Fig. 17. Distribution of measured deflection Θ with $|\Theta| < .010$ radians during nighttime period of flight C3. "Perfect" events (solid histogram) and "one-error" events (dashed histogram) are plotted separately. Curves 1 and 2 give the predicted distribution for cosmic-ray nuclei folded with angular resolutions for which $\sigma_\Theta = .0027$ and $\sigma_\Theta = .003$, respectively.

Step (3): The last step is to check the self-consistency of the trajectory, i.e., to determine whether a particle of the assigned rigidity and measured entrance trajectory could be expected to emerge from the magnet with the measured exit trajectory. An obvious procedure would be to mathematically propagate such a particle through the measured magnetic field in the same manner used in the calculation of the geometrical factor (Chapter II). If the mathematical particle emerged from the field with the measured exit parameters, we would accept the event. The relatively large scattering which can occur and which, of course, is random in nature, considerably complicates this approach, however.

We use a much less time-consuming procedure, which utilizes the symmetry of the detector and the magnetic field and involves the detector resolution in a very straightforward manner. The trajectory parameters used in the checking are illustrated in Figure 18. We show there a projected view of a particle trajectory, assuming no scattering and an idealized magnetic field $\underline{B}$ which is uniform and constant within the magnet gap and zero beyond. For such a field the path is an arc of a circle within the field region and is straight above and below the magnet. We construct the straight line $\underline{ab}$ between the trajectory positions at the bottom high voltage plane of the top

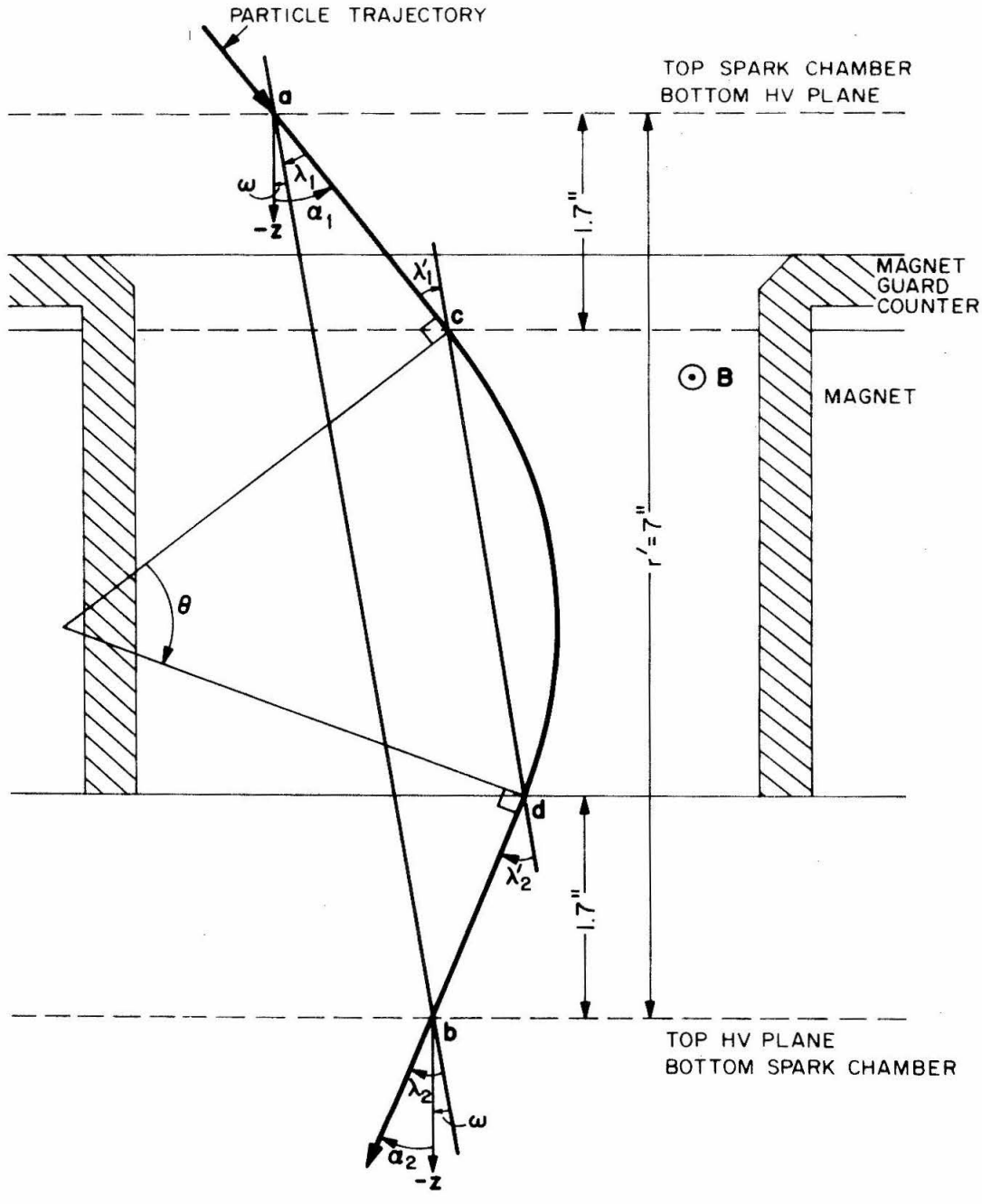

Fig. 18. Schematic view of a particle trajectory seen in projection, with definition of parameters used in trajectory self-consistency checking.

spark chamber and the top high voltage plane of the bottom spark chamber. Similarly, we construct the straight line cd between the trajectory positions at the top and bottom edge of the magnet gap. We define the angles λ_1, λ_2, λ'_1, λ'_2 and ω as shown in Figure 18. Following the convention adopted in Chapter II for the angles α_1, α_2, and Θ, clockwise angles are taken to be positive. The following relationships can be derived directly from the figure and simple geometry.

$$\lambda_1 = - \omega - \alpha_1 \tag{9}$$

$$\lambda_2 = \omega + \alpha_2 \tag{10}$$

$$\Theta = \alpha_2 - \alpha_1 = \lambda_1 + \lambda_2 = \lambda'_1 + \lambda'_2 \tag{11}$$

$$\lambda'_2 - \lambda'_1 = 0 \tag{12}$$

Equation (12) is both a necessary and sufficient condition that an arc of a circle can be drawn between c and d which will join smoothly to the trajectory external to the magnet gap. With the given field such a circular arc is indeed an acceptable path for a particle of some rigidity. The presence of the non-uniform fringing field in the actual detector causes a real trajectory to deviate

from a circular arc, and, in general, also destroys the equality of λ'_1 and λ'_2. However, we can define a new parameter

$$\Delta \equiv \lambda_2 - \lambda_1 \tag{13}$$

which will be useful for the trajectory checking. Determination of λ_1 and λ_2 only requires knowledge of the trajectory in the spark chambers. Using the measured magnetic field, we have calculated the range of Δ for all possible valid trajectories (without scattering) within our acceptance cone and find that in all cases

$$|\Delta| < .05\ |\theta| \tag{14}$$

For most trajectories $|\Delta|$ is very much less than this limit. We shall see below that the measurement of Δ is subject to essentially the same errors as the measurement of θ, which was discussed in section A. To the degree that Δ for the unscattered trajectory approximates zero, Δ is, in fact, a direct measure of the deviation of the measured entrance and exit path segments from a valid unscattered particle trajectory through the detector.

Combining eqs. (9), (10), and (13) we have for Δ

$$\Delta = \alpha_1 + \alpha_2 + 2\omega \tag{15}$$

The standard deviation σ_Δ for the determination of Δ is therefore

$$\sigma_\Delta = \sqrt{2\sigma_\alpha^2 + 4\ \sigma_\omega{}^2} = \sqrt{\sigma_\Theta{}^2 + 4\ \sigma_\omega{}^2} \qquad (16)$$

where σ_ω is the standard deviation of the measurement of ω. The last step in eq. (16) follows from eq. (11). Since we have already included scattering in σ_Θ, we need only consider the intrinsic angular error in σ_ω. Points a and b of the trajectory are each defined by a pair of spark gaps. The derivation of σ_ω is essentially the same as that of σ_α (equations (1), (2), and (3)), with r' replacing r. There are two differences: 1. the selection criteria allow as few as 2 sparks to define the line ab (although in practice this occurs only rarely), and 2. the averaging over incident angles does not apply since ω is restricted to a narrower range of angles than α_1 or α_2. The standard deviation σ_ω is given by

$$\sigma_\omega \simeq \begin{cases} \dfrac{\sigma_\ell}{r'} \simeq .0011 \text{ radians for 4 good sparks} \\ \sqrt{\dfrac{3}{2}}\ \dfrac{\sigma_\ell}{r'} \simeq .0014 \text{ radians for 3 good sparks} \\ \sqrt{2}\ \dfrac{\sigma_\ell}{r'} \simeq .0016 \text{ radians for 2 good sparks} \end{cases} \qquad (17)$$

since $\sigma_\ell \simeq .008"$ (eq. (5), Chapter II) and $r' = 7"$. For our purposes it is sufficient to take an average value

$$\sigma_\omega \simeq .0014 \text{ radians} \tag{18}$$

Substituting eqs. (7) and (18) into eq. (16), we obtain

$$\begin{aligned} \sigma_\Delta &\simeq \sqrt{(.12\theta)^2 + (.003)^2 + 4(.0014)^2} \\ &\simeq \sqrt{(.12\theta)^2 + (.004)^2} \end{aligned} \tag{19}$$

The content of eq. (19), for σ_Δ, is the same as that of eq. (7) for σ_θ, i.e., a term due to scattering and a term due to the intrinsic angular resolution of the instrument (though the latter is somewhat broadened). Hence, in particular, the distribution of scattering angle shown in Figure 15 applies equally well to the Δ distribution. (Note, however, that the gaussian approximation is still used in eq. (19).) Comparing eqs. (14) and (19) we see that, within the resolving ability of the detector, Δ for all unscattered trajectories is very close to zero. Thus the measured value of Δ is a direct indication of the error in the trajectory determination. Furthermore, the distribution for Δ contains the angular resolution of the instrument in a straightforward way which makes it a good

parameter to determine whether given measured entrance and exit trajectories are segments of a self-consistent path.

Based on these considerations and taking into account the true scattering-angle distribution, we choose as a criterion on Δ for acceptance of an event

$$\Delta^2 \leq (.32\theta)^2 + (.008)^2 \qquad (20)$$

This choice of limits on Δ is sufficiently stringent that the probability is very small that an event will be accepted where the assigned trajectory includes spurious spark locations. On the other hand, only about 7 percent of all valid trajectories are rejected, independent of rigidity. This result can be seen from the integral scattering-angle distribution in Figure 15 ($\phi = .32\theta$ corresponds to $p\phi = 1.15$ in the figure) and from the gaussian error distribution with $\sigma = .004$ which applies for the intrinsic angular resolution. In applying this criterion we must use the measured θ, of course, while development of eq. (19) implicitly assumed the "true" θ, corresponding to the true rigidity of the particle. Because the resolution is quite good for rigidities where the value of θ is large, however, the difference does not produce a significant error. The criterion is valid for nuclei as

well as electrons since the electron scattering term is negligible for rigidities where nuclei trigger the instrument.

Figure 19 shows Δ distributions for mono-energetic positrons of 800 and 100 MeV measured at the California Institute of Technology Synchrotron. The appropriate theoretical distributions, including the large-angle scattering, is also shown in each case. The rejection zones according to eq. (20) are indicated by cross-hatching.

Essentially no bias according to particle species or rigidity has been introduced by the event acceptance criteria described in steps (1) and (3) above. Furthermore, the triggering requirements are such that all events are potentially acceptable, depending only on spark chamber performance. It follows that the detection efficiency D, valid for all rigidities, is simply

$$D = \frac{n}{N} \tag{21}$$

where N is the total number of coincidences and n is the number of accepted events. D was typically .7 - .8 throughout all three flights.

Fig. 19. Measured distributions of the trajectory parameter Δ.

Graph A. Mono-energetic beam of 800 MeV positrons. Mean deflection is .0045 radians (Compare Figure 14).

Graph B. Mono-energetic beam of 100 MeV positrons. Mean deflection is .036 radians.

Also shown in each graph is the theoretical distribution. The shaded areas are the rejection zones according to eq. (20).

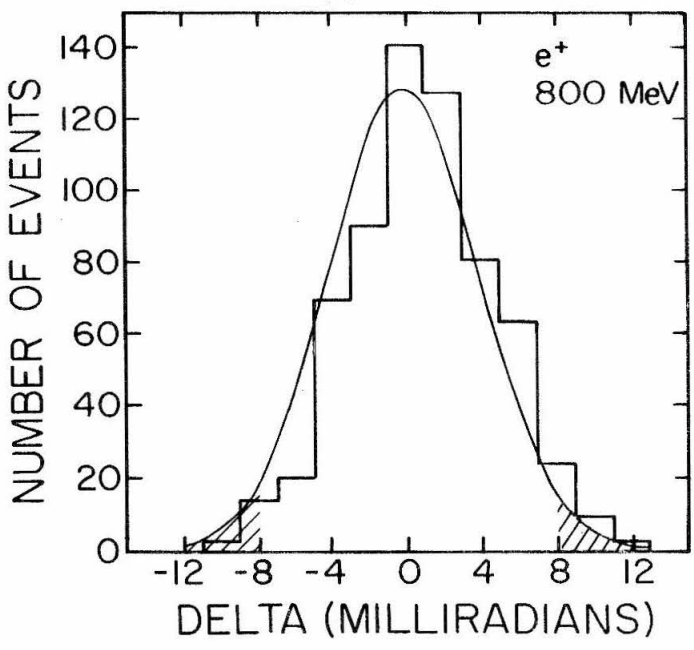

Figure 19 A

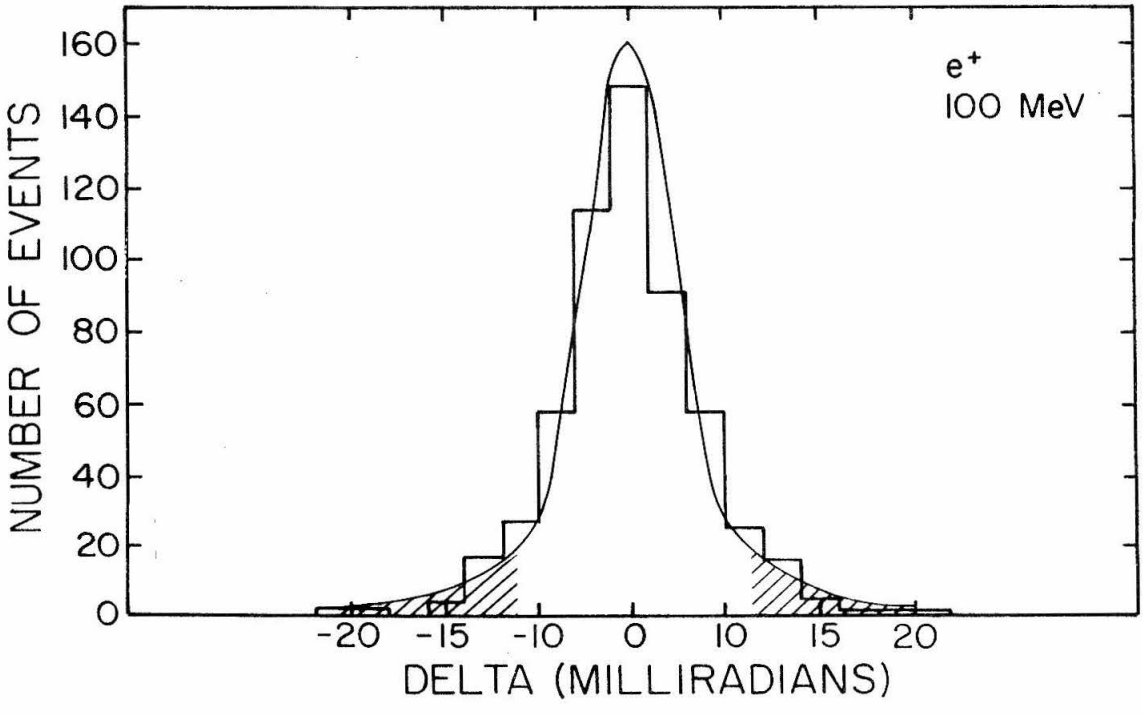

Figure 19 B

C) Dead Time Correction

The phase A period is a natural time interval for evaluating the event rate. During such a 15-minute period the total sensitive time t_s (in seconds) is given by

$$t_s = (900 - n_e t_e)\ (1 - n_a t_a) \qquad (22)$$

where

n_e = number of events recorded

t_e = time required to write a word

= .35 seconds

n_a = total guard counter singles rate (per second)

t_a = dead time following anti-coincidence pulse = 2×10^{-6} seconds

The above formula is correct provided n_a is much less than 5×10^5 counts per second, which was true throughout all flights. The value of n_a used for a given period was the average of the rate recorded during the phase B periods immediately before and after the phase A period in question.

At float altitude the fractional dead time was typically

$$t - t_s = .17\ t$$

The coincidence rate calculated using the sensitive time from equation (22) differs from the rate measured during the phase B period by less than one percent, which is well within the statistical accuracy of the phase B counter.

D) Instrumental background

The probability of a random pulse in the Cerenkov counter accompanying the passage of a particle below the Čerenkov threshold is about 0.1 percent (see Chapter II, section A). For heavy particles with rigidity less than 200 MV this represents a negligible contribution to the measured flux.

Possible sources of contamination from particles above the Čerenkov threshold are discussed individually below.

1. Nucleonic component

Cosmic-ray protons and alpha particles represent about 95 percent of all particles triggering the detector system at float altitude. Because they are effectively confined to small deflection angles, however, their contribution to rigidities below 200 MV can only result from secondary particles or from a possible miscalculation of the trajectory. The probability of the latter was measured in a high energy (1000 MeV) electron beam. The data showed fewer than 0.5 percent of all events which

appeared to have rigidities less than 200 MV. A similar percentage for nuclei in flight would give a rate of 3×10^{-3} counts per second; this is only about 5 percent of the rate in any one of our 5 rigidity intervals. This limit includes any contribution due to knock-on electrons produced in the detector. The total material of the detector in the beam above or within the spark chambers is about .005 interactions lengths; hence contamination by particles resulting from nuclear interactions in the detector is also not significant.

2. Pions and muons

Pions and muons with momentum greater than about 140 MeV/c and 105 MeV/c, respectively, are above the threshold of the lucite Čerenkov counter. At our float altitude pions near 200 MeV/c decay within .002 g/cm^2 of their point of production (59). Hence their contribution relative to muons may be ignored. The muon spectrum at a depth $x << L_a$ is, from Verma (59),

$$F(E_\mu, x)dE_\mu \simeq F_\pi(E_\pi) \frac{dE_\pi}{dE_\mu} dE_\mu \frac{x}{L_i} \left[\frac{1}{g+1} - \frac{x}{L_a} \frac{1}{g+2} \right] \qquad (23)$$

Here $F_\pi(E_\pi)$ is the charged pion production spectrum, E_π and E_μ the pion and muon energies, L_i and L_a the proton

interaction and absorption lengths, respectively, and $g = 1.07/E_\mu$, where E_μ is the muon energy in BeV. We have calculated the muon spectrum at an atmospheric depth of 2.4 g/cm^2, using the pion production spectrum of Perola and Scarsi (60) corrected to the proton spectrum at Fort Churchill in 1968. We make the usual assumption that the pion and resultant decay muon move at the same velocity and use L_a = 120 g/cm^2 and L_i = 100 g/cm^2. The calculated flux of muons with rigidities between 100 and 200 MV is $\sim 10^{-2}$ muons/(m^2·sec·sr·MV). This is about 5 percent of the total measured flux in this interval.

3. Gamma-rays

Gamma-rays may interact in the lucite Čerenkov radiator, trigger that counter, and subsequently scatter upward into the acceptance cone of the detector (see Figure 20). In order to determine the sensitivity to this effect we have calibrated the detector in a γ-ray beam at the California Institute of Technology Synchrotron. Measurements of the high-altitude γ-ray spectrum at various zenith angles have been made by Fichtel, Kniffen and Ögelman (61). Their observations were made at Mildura, Victoria, Australia, in December, 1966. The geomagnetic cutoff rigidity is 4.7 GV at Mildura (62), which is much higher than the value at Fort Churchill (<200MV). The level of

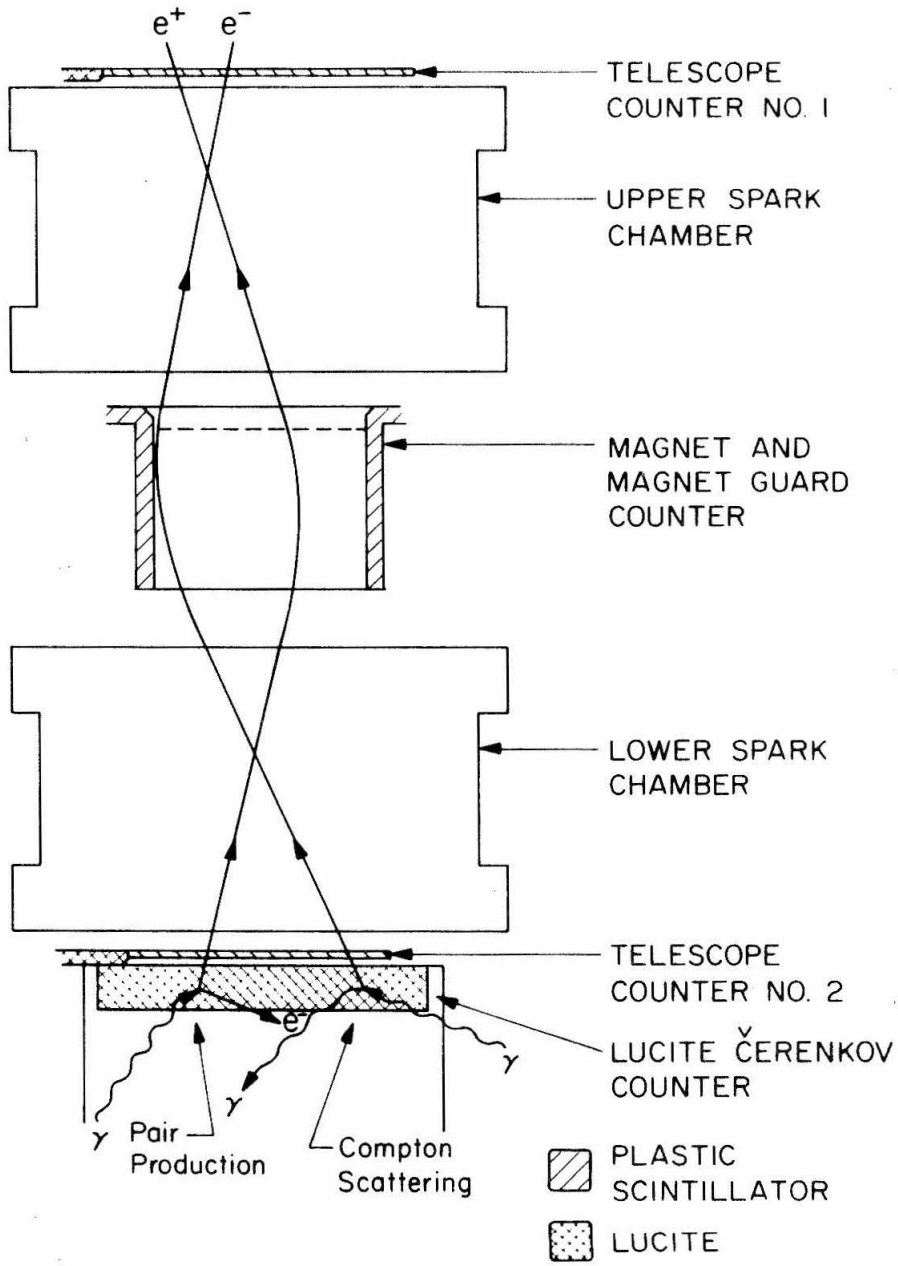

Fig. 20. Schematic representation of gamma-ray interactions in the lucite Čerenkov counter which can produce spurious electron events. The interactions involved are Compton scattering and pair production. Path marked e^+ will be registered as e^- and vice versa due to the backward trajectory.

solar modulation in 1966 was considerably less than in 1968, however. The pion production curves of Perola and Scarsi (60) indicate that these two effects are roughly compensatory. We have therefore used the γ-ray spectra of Fichtel, et al. for Fort Churchill in 1968. Figure 21 shows the derived contribution from this source to our measured positron and negatron spectra at float altitude (63).

With the exception of atmospheric secondary electrons, the γ-ray produced background is the most significant contamination of our measured intensities at low energies. The contribution to the positron flux between 6 and 12 MeV is about 20 percent of the derived primary positron intensity. For negatrons and at higher energies the relative contribution is considerably less. The large error limits which are shown in Figure 21 are estimated errors based on the quoted accuracy of the γ-ray spectrum at balloon altitudes and on the statistical and experimental limitations of the machine calibrations. Further calibrations are being undertaken to improve our knowledge of the sensitivity of our detector to γ-ray produced background. The corrections do not materially affect our final conclusions regarding the primary electron spectrum, however.

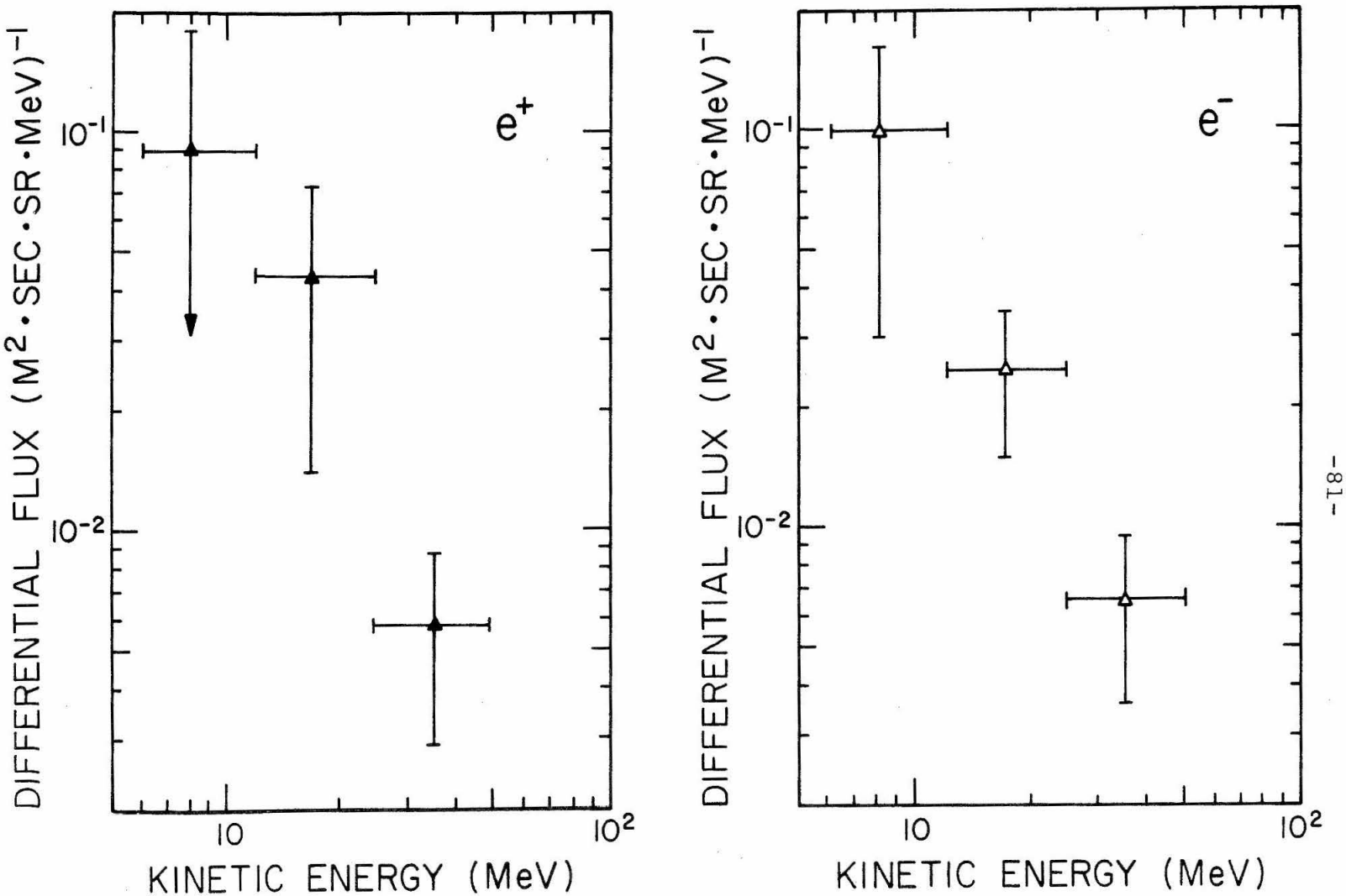

Fig. 21. Gamma-ray produced contribution to measured positron and negatron differential kinetic-energy spectra at balloon altitudes.

4. Splash albedo electrons

In Figure 22 we show the splash albedo spectrum measured at Fort Churchill in 1967 by Israel (18). These particles result primarily from very high energy primary cosmic rays and hence the spectrum in 1968 should be similar. Curve 1 shows this spectrum after propagation through the ~15 g/cm^2 of material in the lower part of our instrument. The lucite Čerenkov counter has an efficiency of .04 for the detection of backward-moving particles. Multiplying curve 1 by the backward detection efficiency, we obtain curve 2 for the contribution to our measured electron spectrum from this source. The splash albedo should consist of essentially equal numbers of positrons and negatrons. The contribution to our measured flux is less than the statistical accuracy throughout our energy interval.

E) Atmospheric Secondaries

A significant part of the electrons between 6 and 200 MeV observed at 2.4 g/cm^2 is of atmospheric origin. The atmospheric electrons result primarily from the decay of pions produced in interactions of the cosmic-ray nuclei with air nuclei; below 20 MeV knock-on electrons also contribute significantly. At somewhat greater atmospheric

Fig. 22. Differential kinetic-energy spectrum of splash albedo electrons. The measurements of Israel (Ref. 18) were made in 1967.

Curve 1: the spectrum after propagating through 15 g/cm^2 of material in the lower gondola.

Curve 2: the background contribution to our measured spectrum of downward-moving electrons, obtained by multiplying curve 1 by the backward detection efficiency, .04.

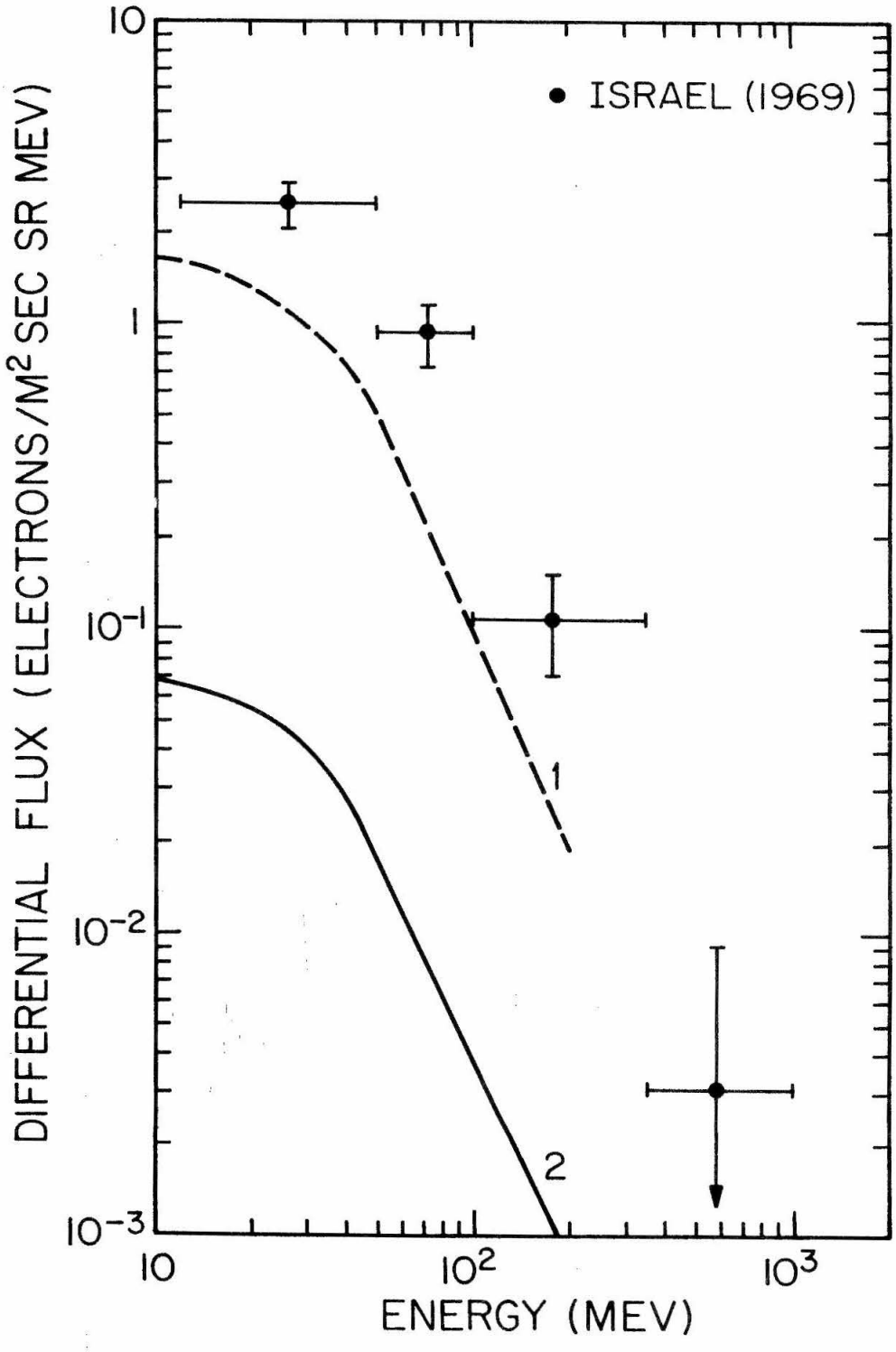
ISRAEL (1969)
DIFFERENTIAL FLUX (ELECTRONS/M² SEC SR MEV)
ENERGY (MEV)
10
1
10⁻¹
10⁻²
10⁻³
10
10²
10³
1
2

Figure 22

depths electromagnetic cascade showers become the dominant source.

Calculations of the atmospheric secondary electron spectrum have been published by Verma (59) and by Perola and Scarsi (60). The two calculated spectra differ considerably below several hundred MeV. In addition, neither includes knock-on electrons nor attempts to separate positrons and negatrons. A new calculation has been made recently by Beuermann (47). This calculation uses the pion production spectrum of Perola and Scarsi (60) corrected to the incident proton spectrum in 1968; it also includes knock-on electrons. The spectra of atmospheric secondary positrons and negatrons are calculated separately over a wide range of atmospheric depths. The depth dependence of the residual primaries can be calculated in a similar manner, given an incident spectrum.

We separate the primary and secondary contributions to our measured flux in the following manner. The atmospheric depth dependence of the total positron or negatron flux $J_i^{\pm}(d)$, for the i^{th} energy interval, is of the form

$$J_i^{\pm}(d) = a_i^{\pm} s_i^{\pm}(d) + b_i^{\pm} p_i^{\pm}(d) \qquad (23)$$

where d is the atmospheric depth, $s_i^{\pm}(d)$ and $p_i^{\pm}(d)$ give the functional form of the calculated depth dependence of

the flux of secondary and primary positrons or negatrons, respectively, and $a_i^{\pm}$ and $b_i^{\pm}$ are parameters giving the relative contribution of each component. We determine the parameters $a_i^{\pm}$ and $b_i^{\pm}$ by making a least-squares fit to seven data points from 2.4 to 42 g/cm^2 atmospheric depth. Since $p_i^{\pm}(d)$ depends on the unknown incident primary spectrum, an iterative process must be used. The derived primary contribution at float altitude, $b_i^{\pm}p_i^{\pm}(d = 2.4\ g/cm^2)$, is not very sensitive to the choice of the incident primary spectrum, $p^{\pm}(d = 0)$, however, and so the iteration converges quickly.

In Figure 23 we show the measured growth curves and the residual primary and atmospheric secondary contributions determined by the least-squares fit. Included are data from the ascent (which in each case occurred after the evening transition to lower geomagnetic cutoff) and from the nighttime interval of the float period. (See Chapter V, section A for a discussion of the diurnal cutoff variation). The data from the 3 flights showed no systematic variations and have therefore been combined for greater statistical accuracy. The energy intervals indicated are those at the top of the detector. The χ^2 probability P for each fit is included in the graphs. In the 50-100 MeV interval, the calculated atmospheric

secondary growth curves for both positrons and negatrons fit the measured curves within statistical errors. The fit for both results in a small negative primary contribution. For this interval, therefore, only upper limits can be derived. The measured spectra of positrons and negatrons together with the separation into primary and secondary components resulting from our fitting technique are shown in Figure 28 and discussed in Chapter V, section B.

Fig. 23. Measured positron and negatron event rates vs. atmospheric depth for the nighttime period. The energy intervals indicated are those measured at the top of the detector. Also shown is the separation into primary and atmospheric secondary components as determined by the least-squares fitting technique described in the text.

Dashed curve: best-fit primary contribution

Dash-dot curve: best-fit secondary contribution

Solid curve: best-fit total positrons or negatrons

The χ^2 probability, P, is indicated for each fit. The increase in the intensity of the primary component with increasing depth, which is evident in some of the graphs, is due to the assumed form of the extraterrestrial positron and negatron spectra (see Fig. 28).

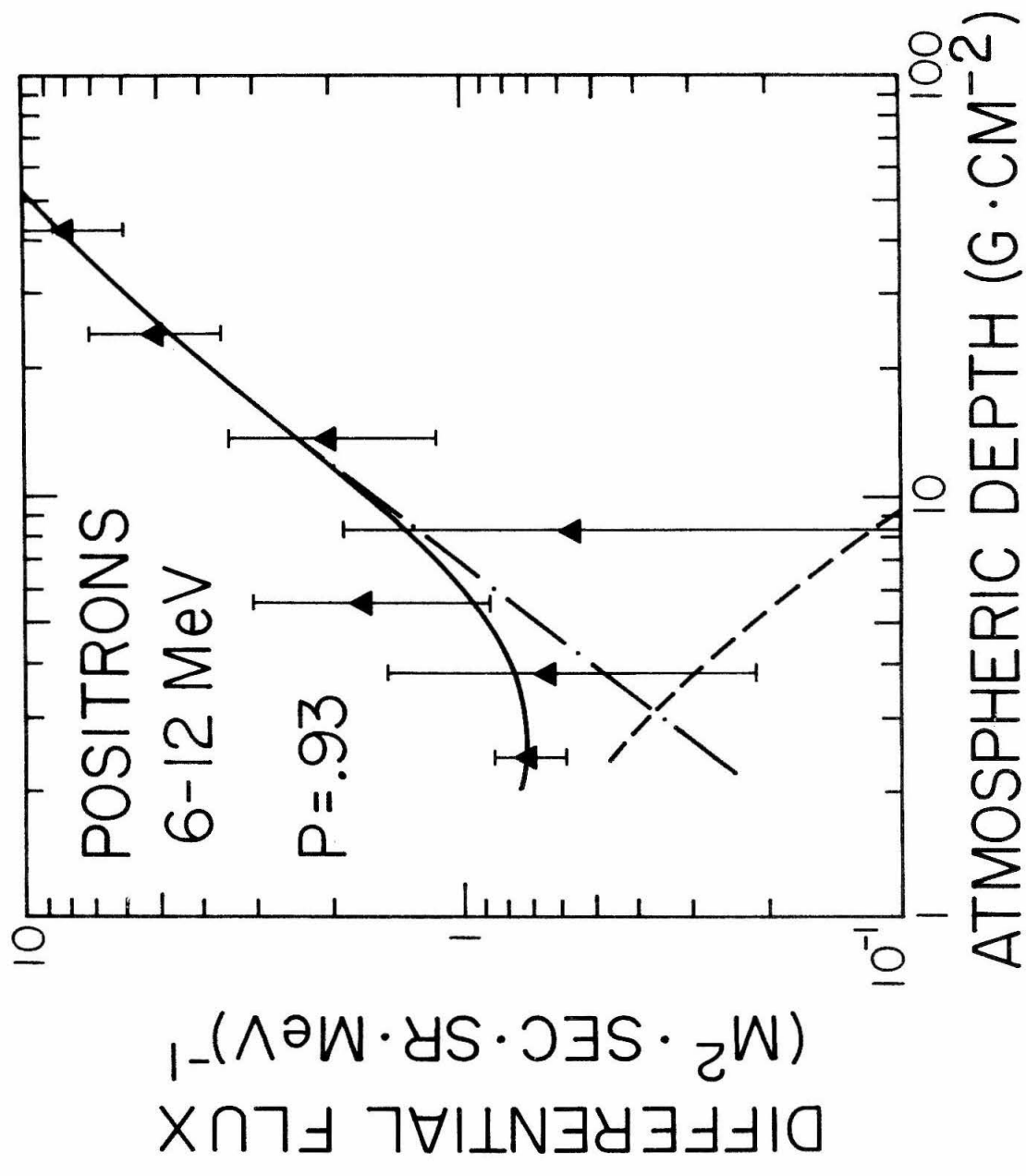
POSITRONS
6-12 MeV
P=.93
DIFFERENTIAL FLUX
(M² · SEC · SR · MeV)⁻¹
ATMOSPHERIC DEPTH (G · CM⁻²)
10
1
10⁻¹
10
100

Figure 23 A

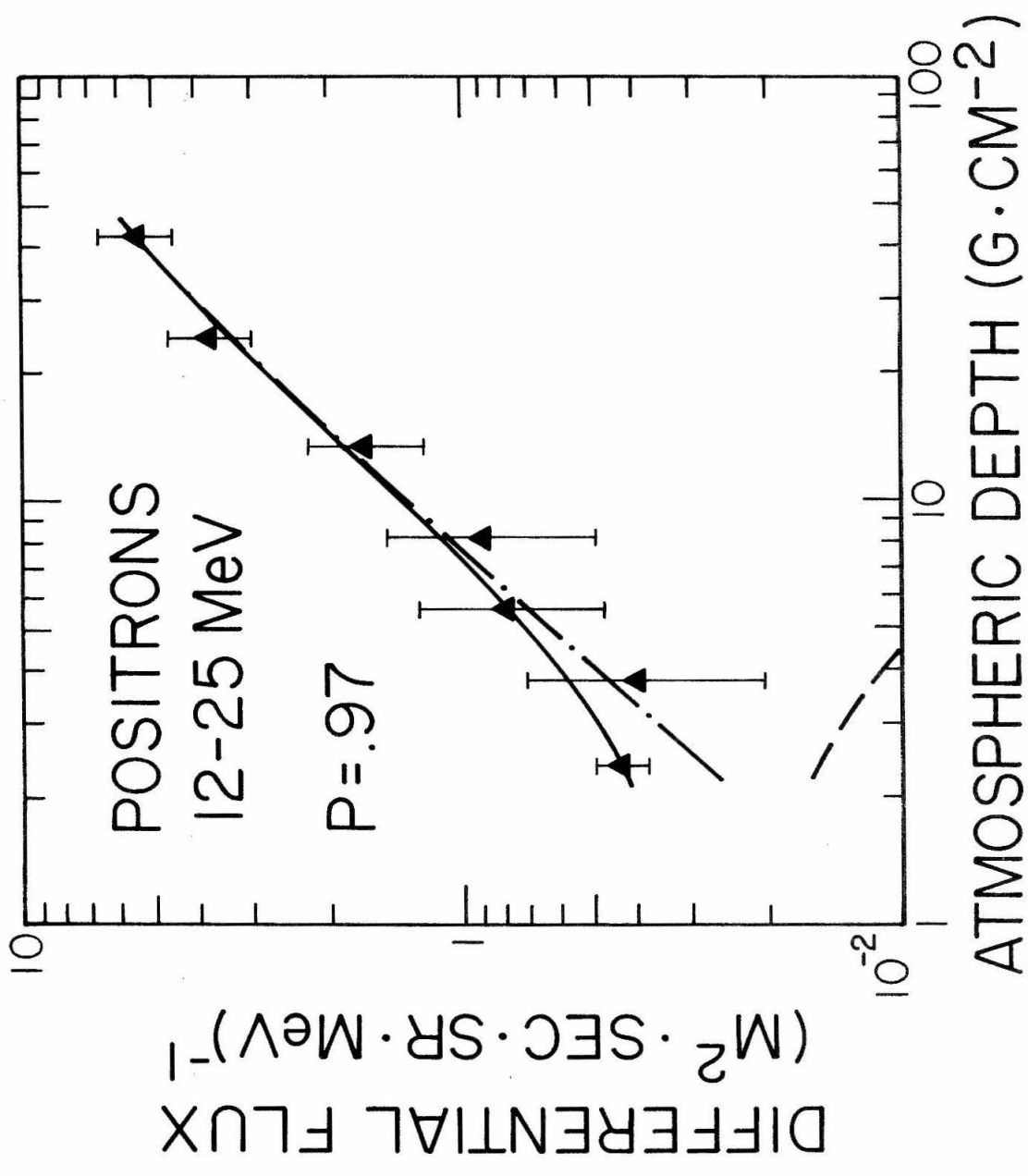
DIFFERENTIAL FLUX
(M² · SEC · SR · MeV)⁻¹
10
1
10⁻²
POSITRONS
12-25 MeV
P=.97
1
10
100
ATMOSPHERIC DEPTH (G·CM⁻²)

Figure 23 B

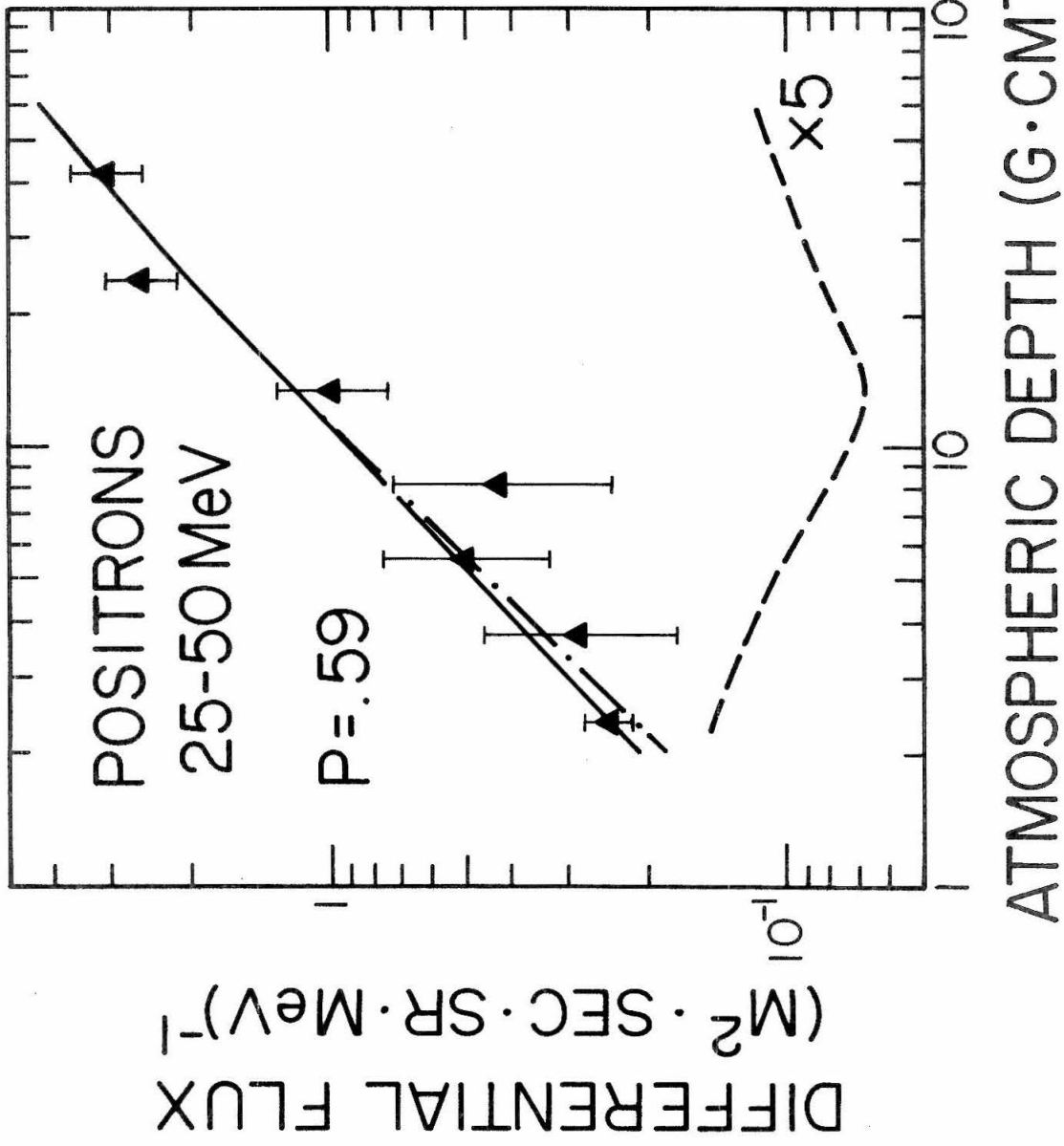
POSITRONS
25-50 MeV
P=.59
x5
DIFFERENTIAL FLUX
(M² · SEC · SR · MeV)⁻¹
ATMOSPHERIC DEPTH (G·CM⁻²)
10⁻¹
1
10
100

Figure 23 c

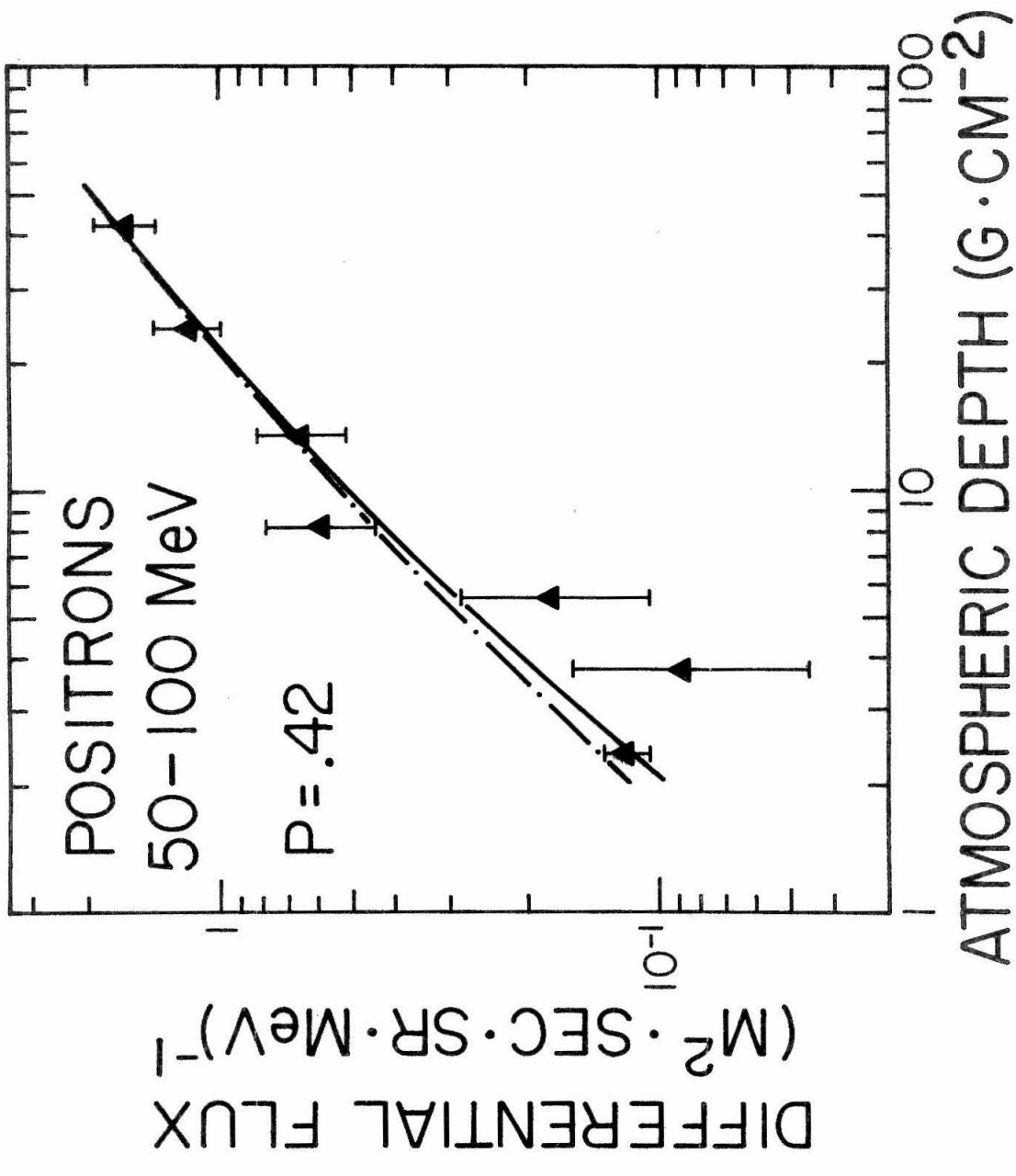
POSITRONS
50-100 MeV
P=.42
DIFFERENTIAL FLUX
(M² · SEC · SR · MeV)⁻¹
10⁻¹
1
10
100
ATMOSPHERIC DEPTH (G·CM⁻²)

Figure 23 D

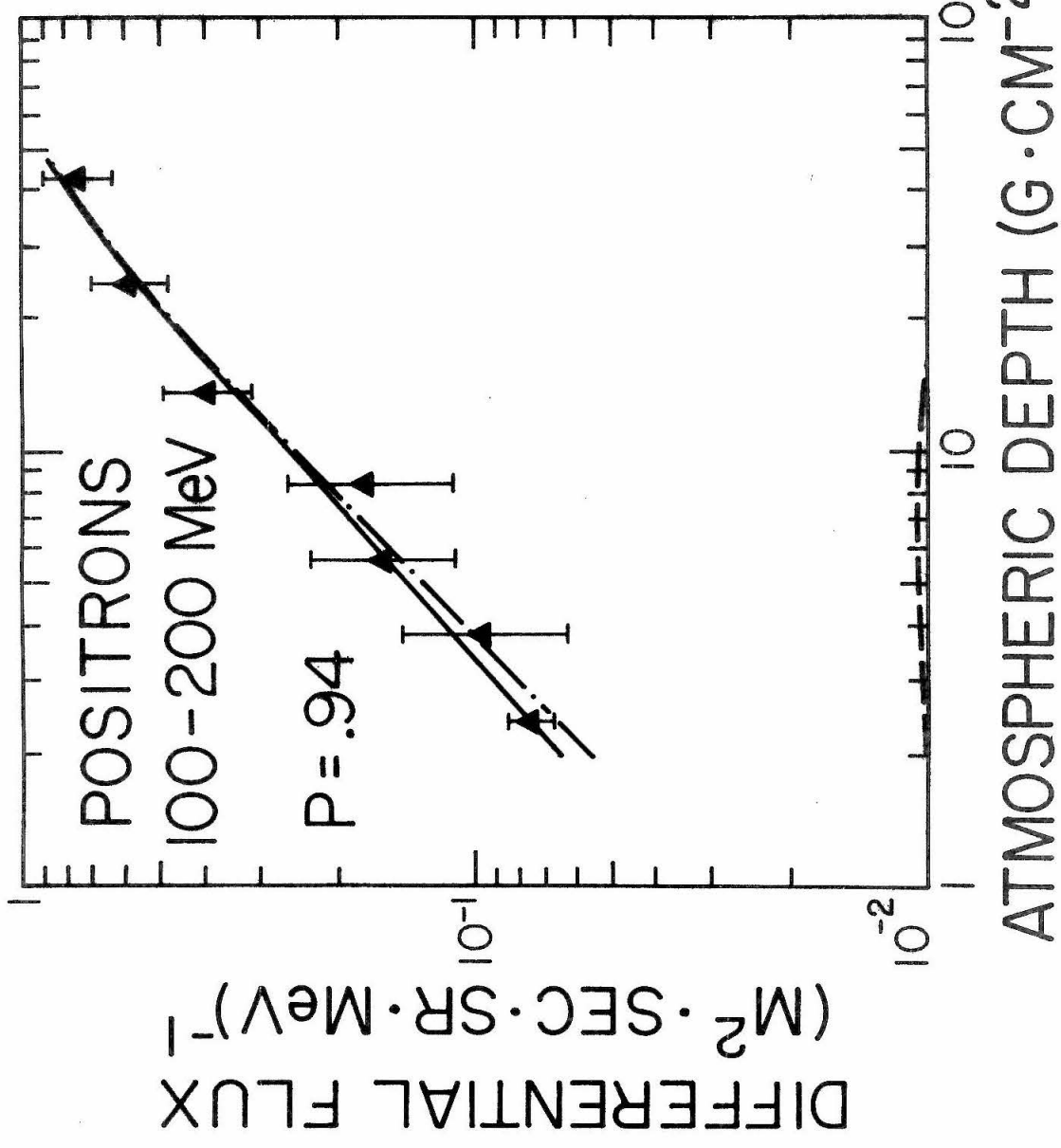
POSITRONS
100-200 MeV
P=.94
DIFFERENTIAL FLUX
(M² · SEC · SR · MeV)⁻¹
ATMOSPHERIC DEPTH (G·CM⁻²)
10⁻¹
10⁻²
10
100

Figure 23 E

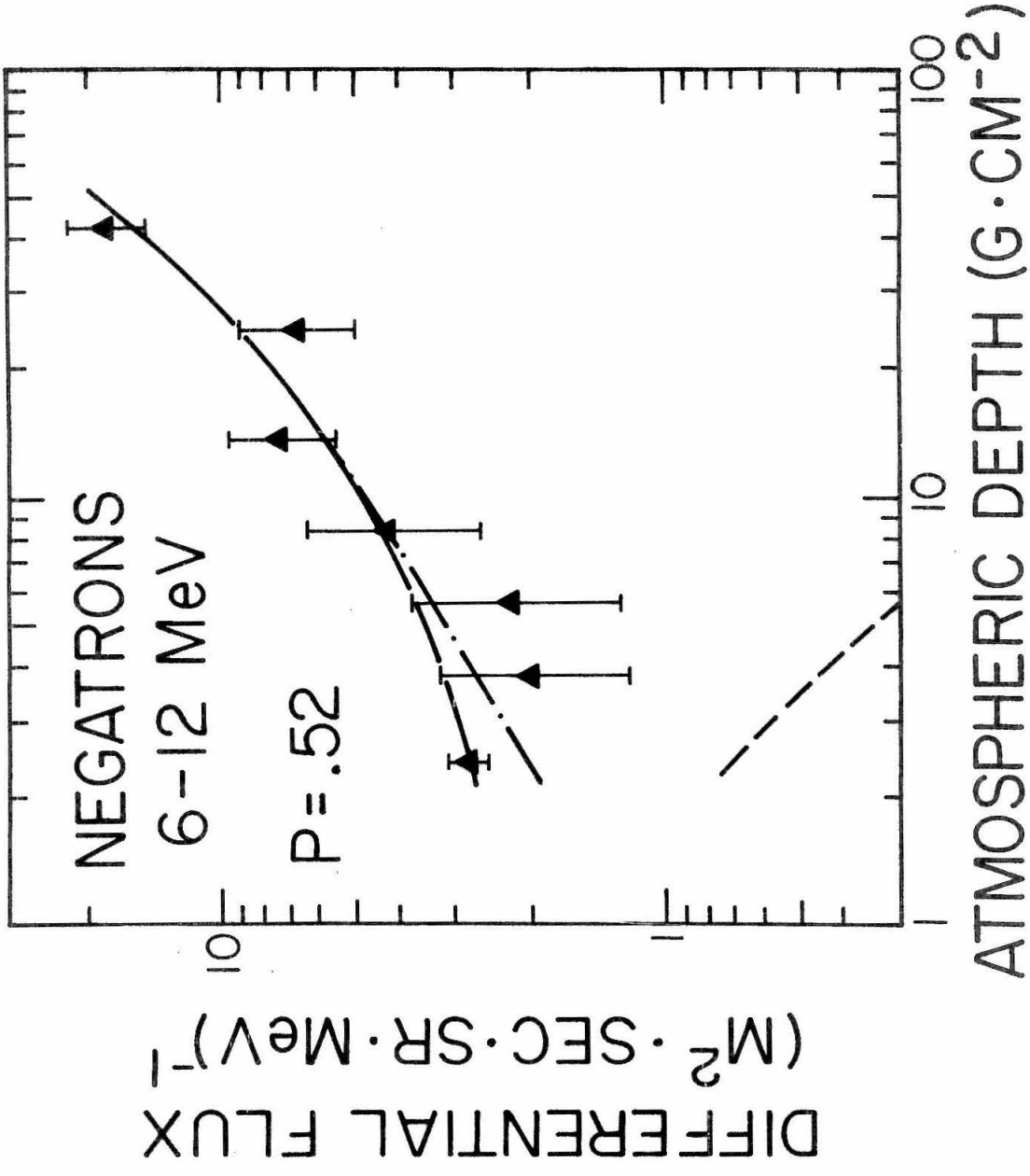
NEGATRONS
6-12 MeV
P=.52
10
1
10
100
ATMOSPHERIC DEPTH (G·CM-2)
DIFFERENTIAL FLUX
(M2·SEC·SR·MeV)-1

Figure 23 F

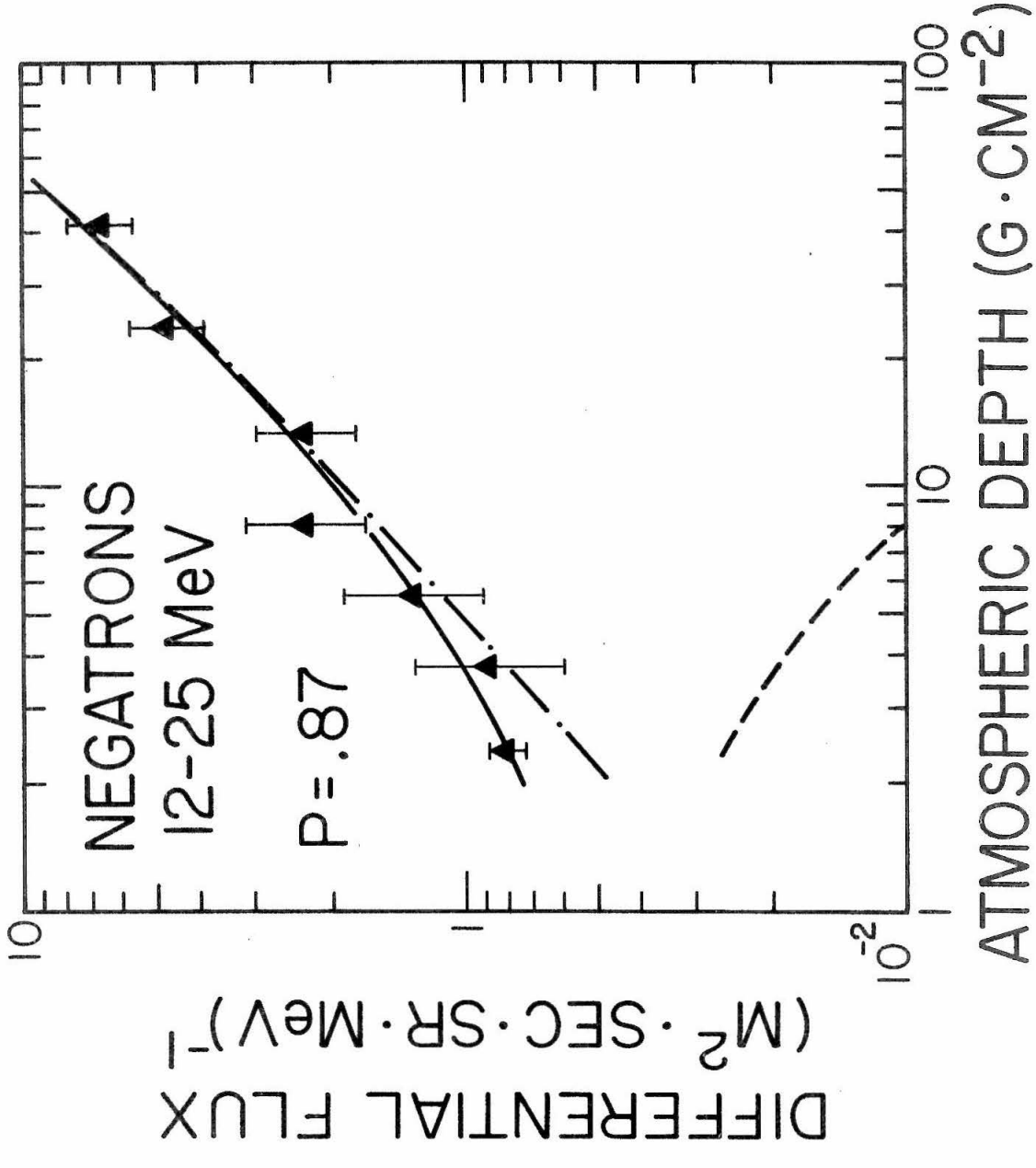
NEGATRONS
12-25 MeV
P=.87
DIFFERENTIAL FLUX
(M² · SEC · SR · MeV)⁻¹
ATMOSPHERIC DEPTH (G·CM⁻²)
10
1
10⁻²
1
10
100

Figure 23 G

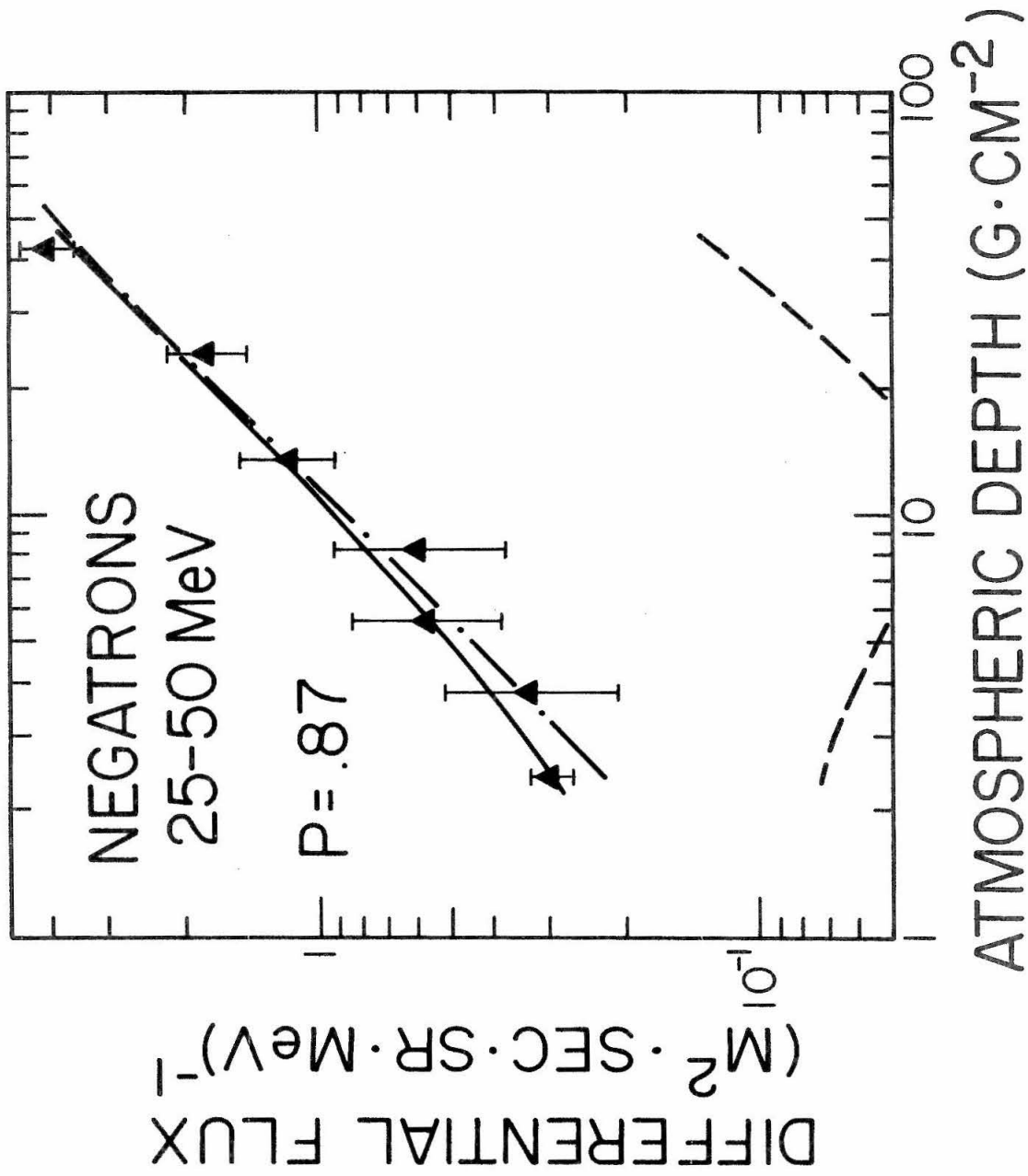
NEGATRONS
25-50 MeV
P= .87
DIFFERENTIAL FLUX
(M² · SEC · SR · MeV)⁻¹
10⁻¹
1
10
100
ATMOSPHERIC DEPTH (G·CM⁻²)

Figure 23 H

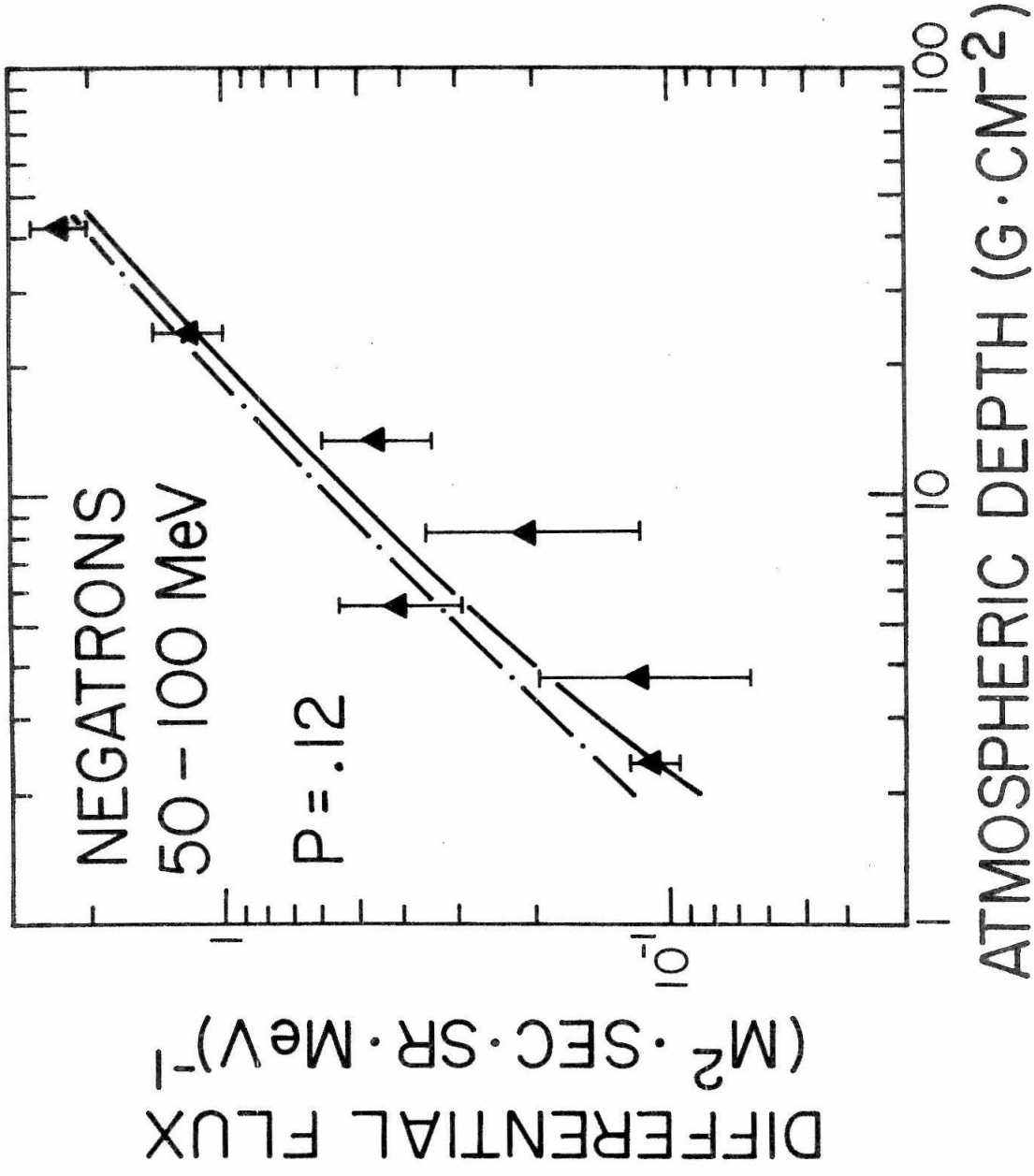
NEGATRONS
50 - 100 MeV
P = .12
DIFFERENTIAL FLUX
(M² · SEC · SR · MeV)⁻¹
ATMOSPHERIC DEPTH (G · CM⁻²)
10⁻¹
1
10
100

Figure 23 I

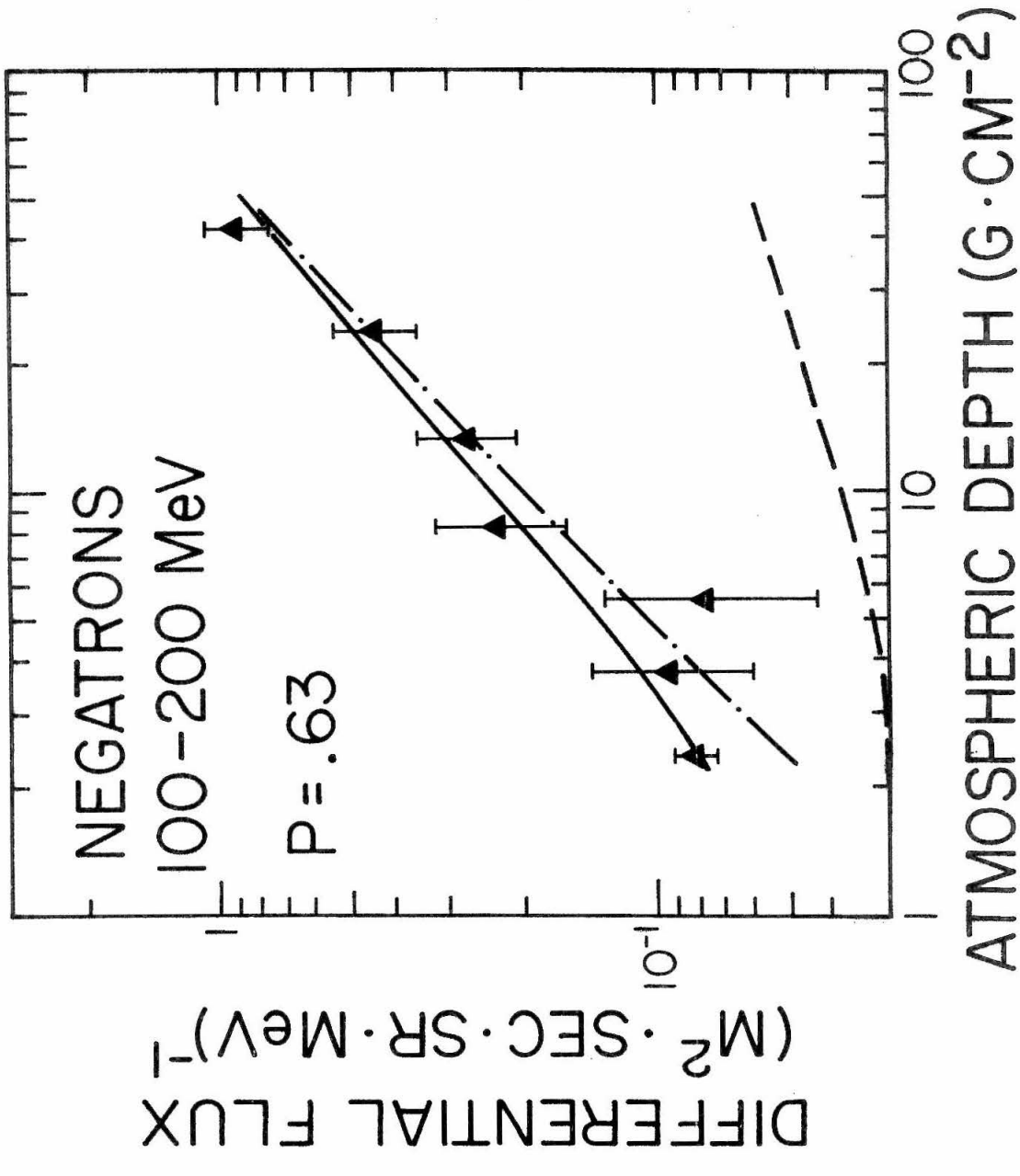
NEGATRONS
100-200 MeV
P=.63
DIFFERENTIAL FLUX
(M² · SEC · SR · MeV)⁻¹
ATMOSPHERIC DEPTH (G·CM⁻²)
10⁻¹
10
100

Figure 23 J

V. RESULTS AND DISCUSSION

A) Diurnal variation of the geomagnetic cutoff

Fort Churchill is the northernmost balloon-launching station where the facilities and terrain permit experiments to be handled with relative ease and good probability of equipment recovery after flight. The nominal geomagnetic cutoff rigidity, calculated for the internal geomagnetic field only, is ~200 MV at Fort Churchill (62). The observation of primary cosmic rays considerably below this rigidity is made possible by a large decrease in the local geomagnetic cutoff rigidity at night. This diurnal cutoff variation is of great interest in itself as a tool to study the magnetosphere. Our concern here, however, will be with the variation as it relates to low-rigidity primary cosmic rays. More general discussions can be found in the literature.

1. Background

The geomagnetic field prevents low-rigidity cosmic rays from reaching the earth at low latitudes. Calculations of the geomagnetic cutoff rigidity based on the internal field of the earth have been performed by several investigators. At the same time it has become apparent that the actual cutoffs differ from these calculations, particularly

at high latitudes. In addition, a diurnal variation in the local cutoff rigidity has been observed at geomagnetic latitudes between 65° and 75°. This cutoff variation has been observed in polar cap absorption (PCA) events (64), in measurements of low energy solar proton fluxes made on polar orbiting satellites (65) (66), and in measurements of low energy electrons observed with balloon-borne detectors (11) (46) (67). The electron data have shown that the cutoff near Fort Churchill (invariant latitude ≈70°) varies from above 100 MV during the day to below 10 MV at night. The transitions, which last 1-2 hours, occur at about 0600 and 1800 local time.

A consistent theoretical picture has emerged which attributes the cutoff variation to the influence of the geomagnetic tail (68-71). In Figure 24 we show schematically a model of the magnetosphere constructed by Williams and Mead (72) based on available satellite data. At geomagnetic latitudes $\leq$ 68° the field lines retain a quasi-dipole shape at all times, while at high latitudes, $\geq$ 80°, the field lines are always swept back into the tail. At intermediate latitudes, 68°-80°, however, the field lines change from a near dipole shape during the day to extension deep into the tail at night. There is evidence that interplanetary particles have essentially free access to

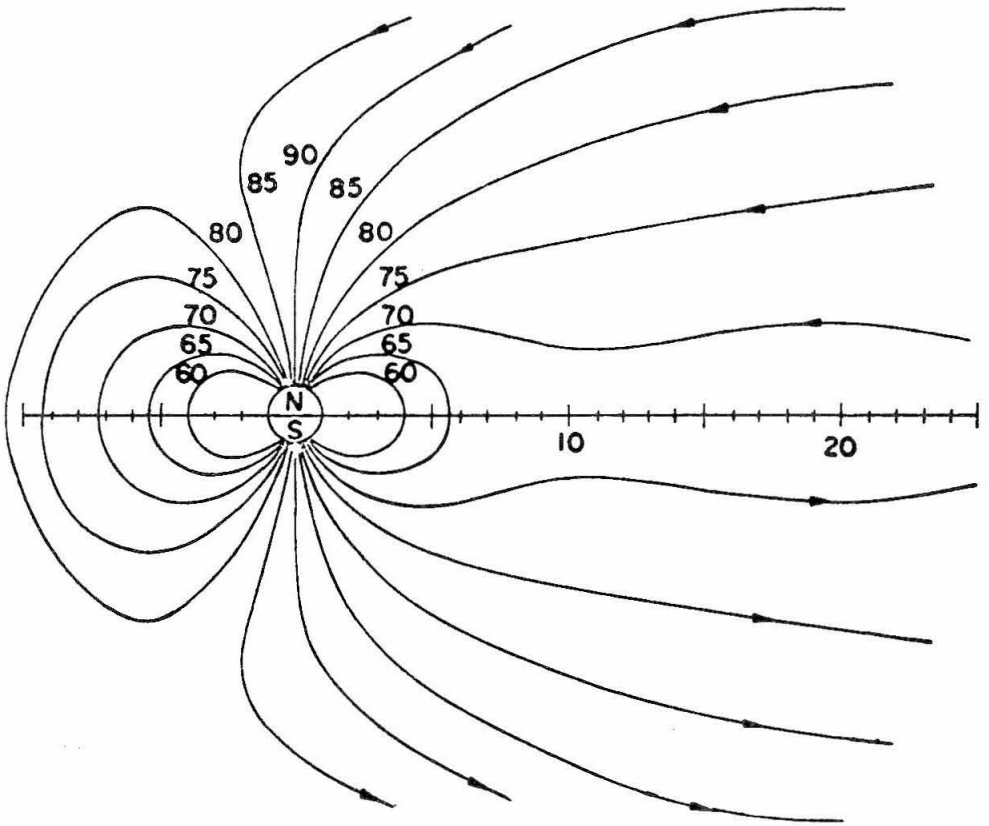

Fig. 24. Geomagnetic field lines in the Williams and Mead model magnetosphere. The horizontal scale indicates distance in units of earth radii. Individual field lines are labeled by the geomagnetic latitude at which they intersect the earth.

the tail, where they can travel freely along the field until they reach the earth (73-75). The cutoff at the foot of a geomagnetic field line which extends into the tail should therefore be essentially zero. On the other hand, if the field line is a quasi-dipole line, connecting directly with a conjugate point in the opposite hemisphere, one would expect the local cutoff to be similar to that calculated using only the internal field. Detailed calculations of particle orbits in the Williams and Mead model magnetosphere have been performed which support the general picture outlined above (70-72).

This theoretical model leads to the following interpretation of the electron measurements (46). During the day the cutoff at Fort Churchill is somewhere between about 100 and 200 MV. The electron flux measured below the cutoff is a mixture of atmospheric secondaries and return albedo. At about 1800 local time the local field lines are swept back into the tail and the cutoff decreases to near zero. The return albedo particles are then replaced by the interplanetary electron flux, which is of lower intensity. The measured flux therefore decreases sharply. At about 0600 local time the reverse transition takes place. This interpretation of the measured electron flux variation is supported by the data of Israel (18) who

measured the splash albedo spectrum at Fort Churchill and found it to be in good agreement with his measured downward-moving daytime electron spectrum below about 100 MeV.

2. Results and discussion

We have referred previously to the timing of our observations which enables us to use data gathered during ascent to directly correct our nighttime measurements for the contribution of atmospheric secondary electrons (Chapter IV, section E). We present here profiles of count rate versus local time which show the location of the morning transition during each flight and the limits of the nighttime and daytime periods used in subsequent analysis. We also present evidence that the nighttime cutoff was below our analysis threshold of 6 MeV at the detector. In addition, our measurement of the charge ratio of the daytime flux is entirely new evidence supporting the albedo origin of this component.

In Figure 25, we show our hourly count rate plotted against local time for each of the three flights. Positron (dotted histogram) and negatron (solid histogram) count rates are shown separately for 5 energy intervals between 6 and 200 MeV at the detector. Data from 4 consecutive phase A periods, an elapsed time of 64 minutes, are

Fig. 25. Event rate vs. local time. Negatrons (solid histogram) and positrons (dotted histogram) are shown separately. Typical 1-σ error limits are indicated. The limits of the time intervals included in summaries of "daytime" and "nighttime" data are indicated. Also shown are the contributions from atmospheric secondary negatrons (long dashes) and positrons (short dashes). In the energy intervals 25-50 MeV and 50-100 MeV positron and negatron secondary intensities are approximately equal; therefore only one component is shown. Variations in the secondary rate reflect altitude variations.

Graph A. Flight C1

Graph B. Flight C2

Graph C. Flight C3

A period of bad data near 0800 local time during flight C3 has been omitted.

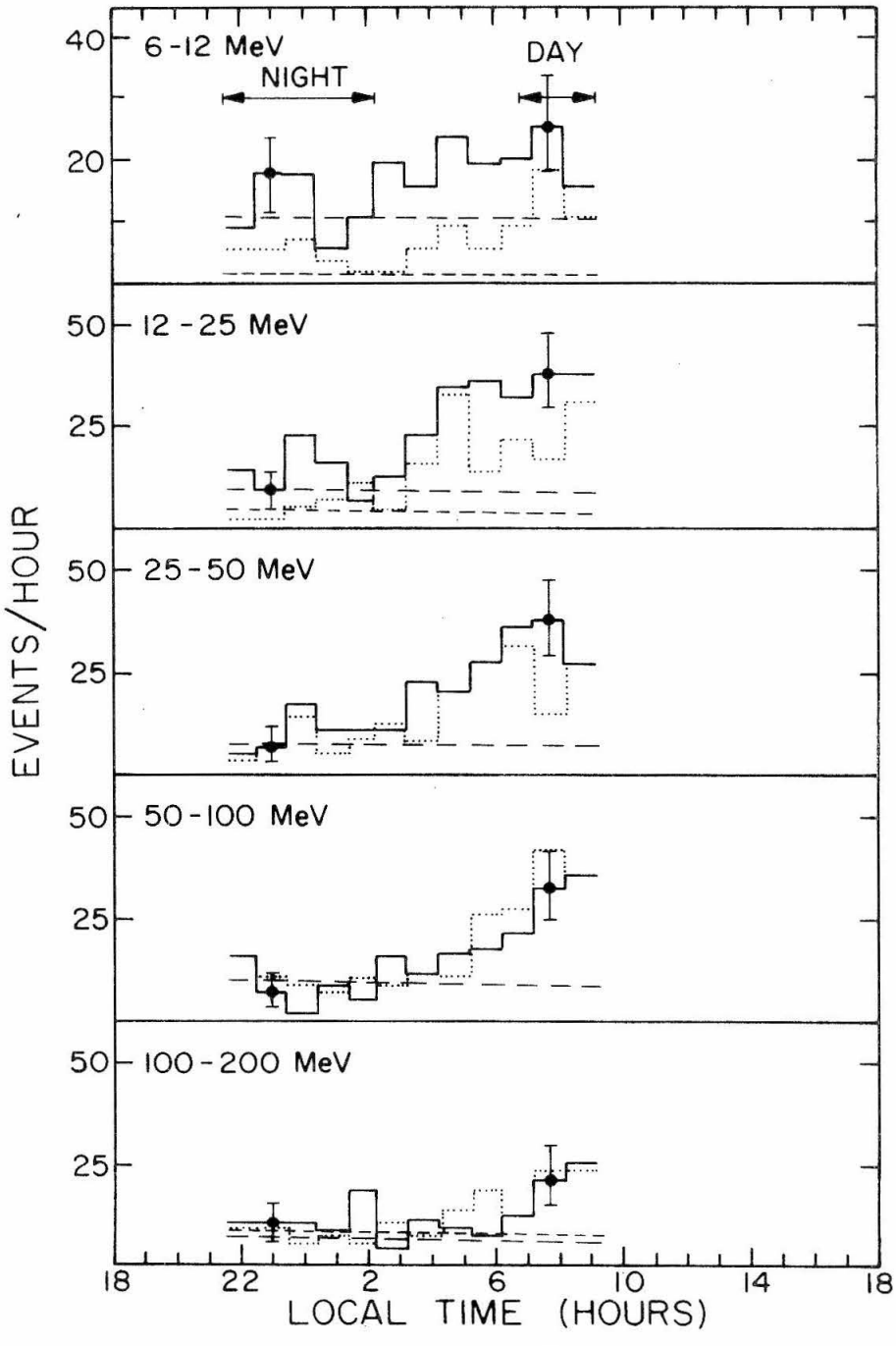

Flight C1

Figure 25 A

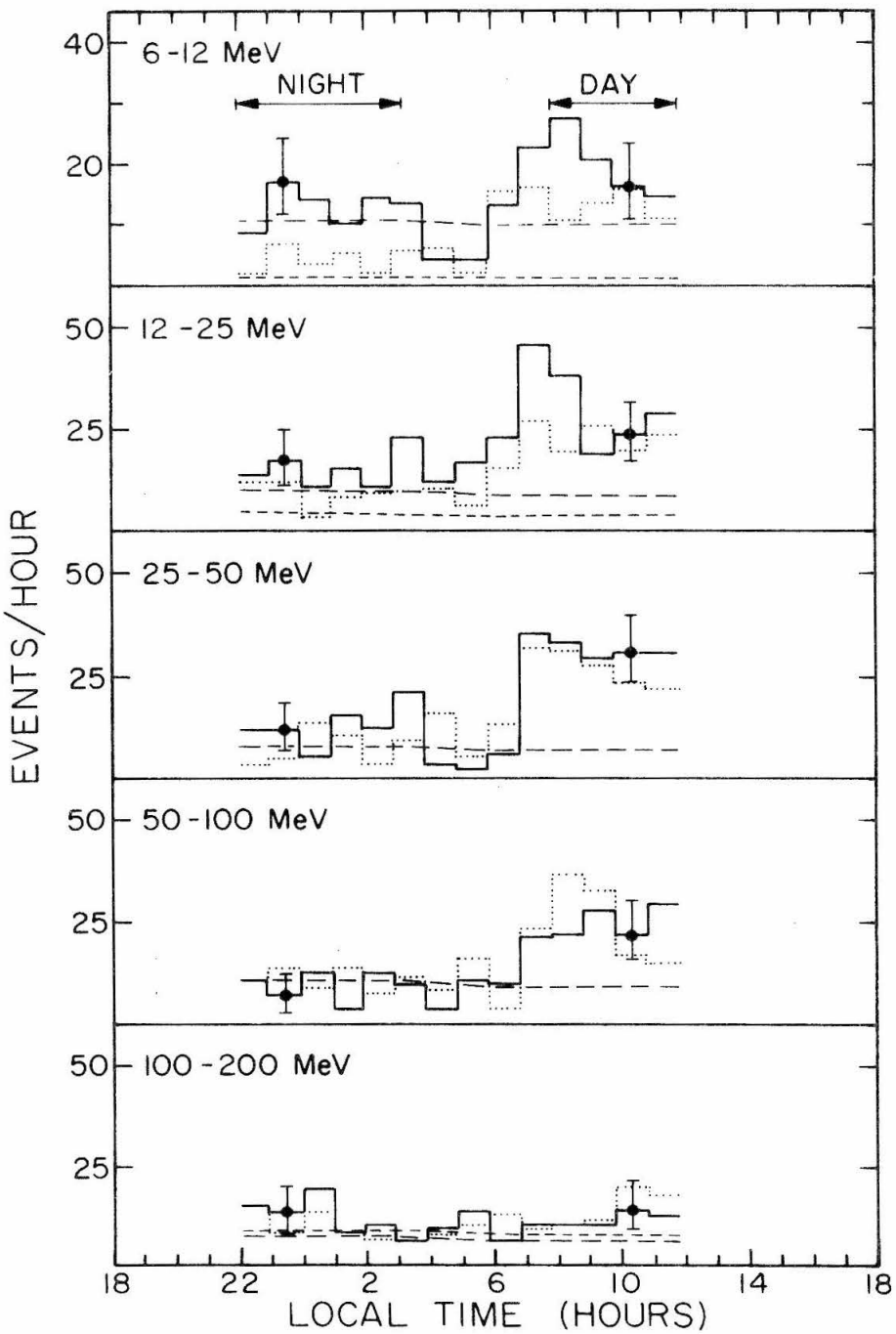

Flight C2

Figure 25 B

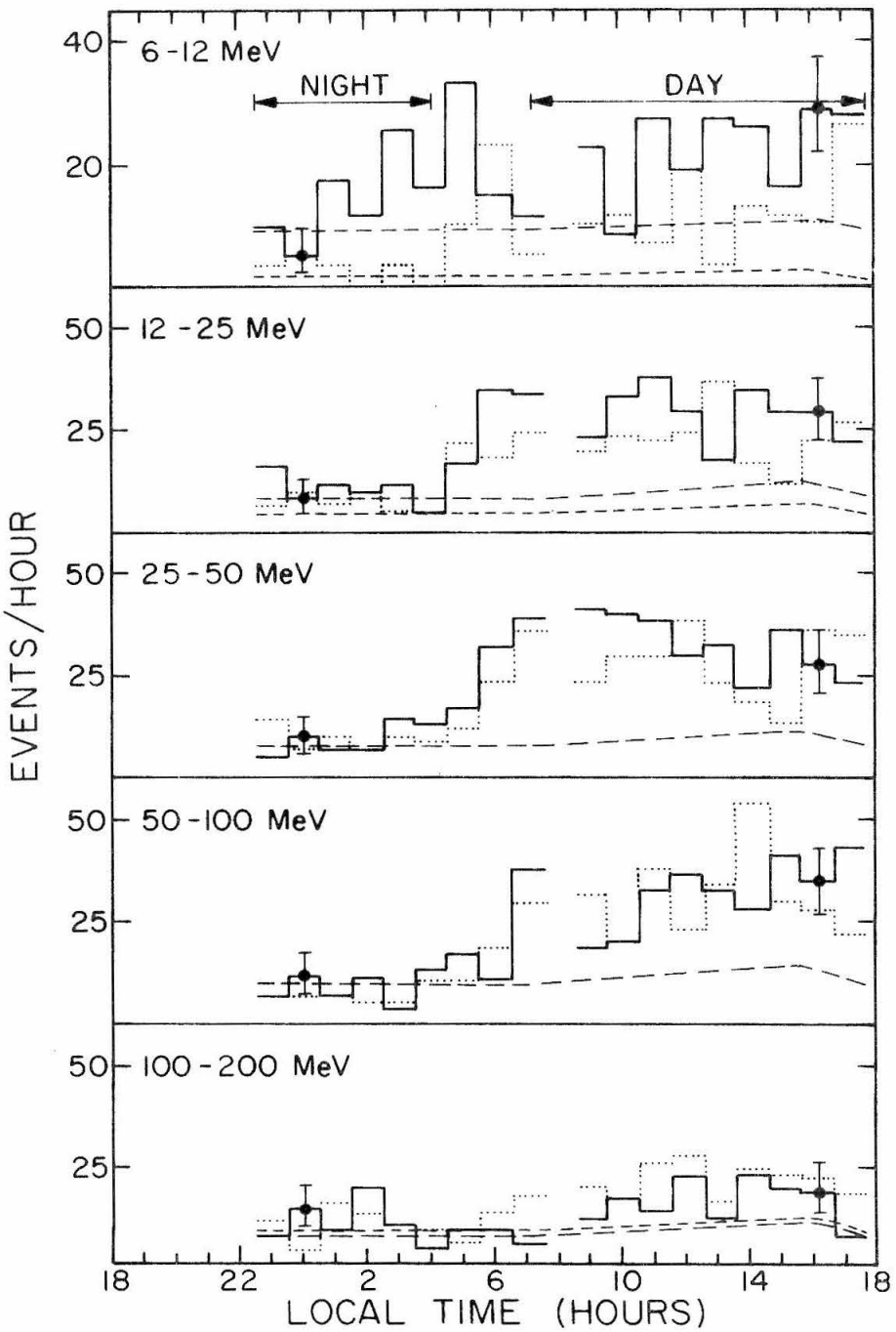

Flight C3

Figure 25 C

averaged for each point. Typical error limits are indicated. The dashed curves (long dashes for negatrons and short dashes for positrons) give the contribution of atmospheric secondaries as determined by our least-squares fit.

In flight C2 the morning transition occurs later than for flights C1 and C3 (about 0700 local time versus approximately 0300 and 0430 local time). It is also more abrupt. The trajectories of all three flights were similar (Figure 11) so that the difference cannot be due simply to a different location of the detector in the geomagnetic field. A small solar event occurred during the latter part of flight C2, around 1600 UT (0800 local time at the detector), but it is difficult to imagine a connection with the delayed transition which actually preceded the solar event. Large variations in the time and abruptness of the transitions have also been observed by Israel and Vogt (67) in 1967, including one flight (their flight C1) where the morning transition had a time profile similar to the transition seen in our flight C2. On the other hand, they did not see a transition as early as the one during our flight C1 in any of their three flights. All of the flights of Israel and Vogt occurred during quiet geomagnetic conditions. Jokipii, L'Heureux, and Meyer (44) observed 5 transitions, all between 0500 and 0700 local

time. Hovestadt and Meyer (76), flying within several weeks of our flights, observed a transition at ~0400 local time. On the other hand, Rockstroh and Webber (12), whose flight was only 2 days after our flight C3, claim to see a morning transition after ~0900 local time (77). It is possible that day-to-day changes in the configuration of the magnetosphere are causing the large variations in the transition time. Despite the fact that there is no statistically significant change in the measured electron flux in flight C2 until the transition near 0700 local time, we have included in our nighttime data interval only the period prior to 0945 UT (0304 local time). We thus make the nighttime period included in the data summary similar for all flights.

The energy interval between 100 and 200 MeV displays a more diffuse transition than the other intervals in all flights. During flight the balloon moved westward, passing to lower geomagnetic latitudes (see Figure 11), and consequently to higher dipole cutoffs. We are thus probably seeing a mixture of the initial transition from the tail field cutoff near zero MV to a closed field cutoff near or somewhat above 100 MV followed by a more gradual change due at least partly to the motion of the balloon.

In Figure 26 we show the measured daytime and nighttime positron and negatron raw spectra for each flight.

Fig. 26. Measured differential kinetic-energy spectra of positrons and negatrons for daytime and nighttime intervals. The data from each flight are plotted separately. Nighttime spectra are for an average floating depth of 2.4 g/cm^2 residual atmosphere. Daytime spectra are for an average depth of 2.2 g/cm^2. The daytime data of flight C3 have been corrected for the change in altitude toward the end of that flight. All other data are raw fluxes.

Graph A. Positrons - night

Graph B. Negatrons - night

Graph C. Positrons - day

Graph D. Negatrons - day

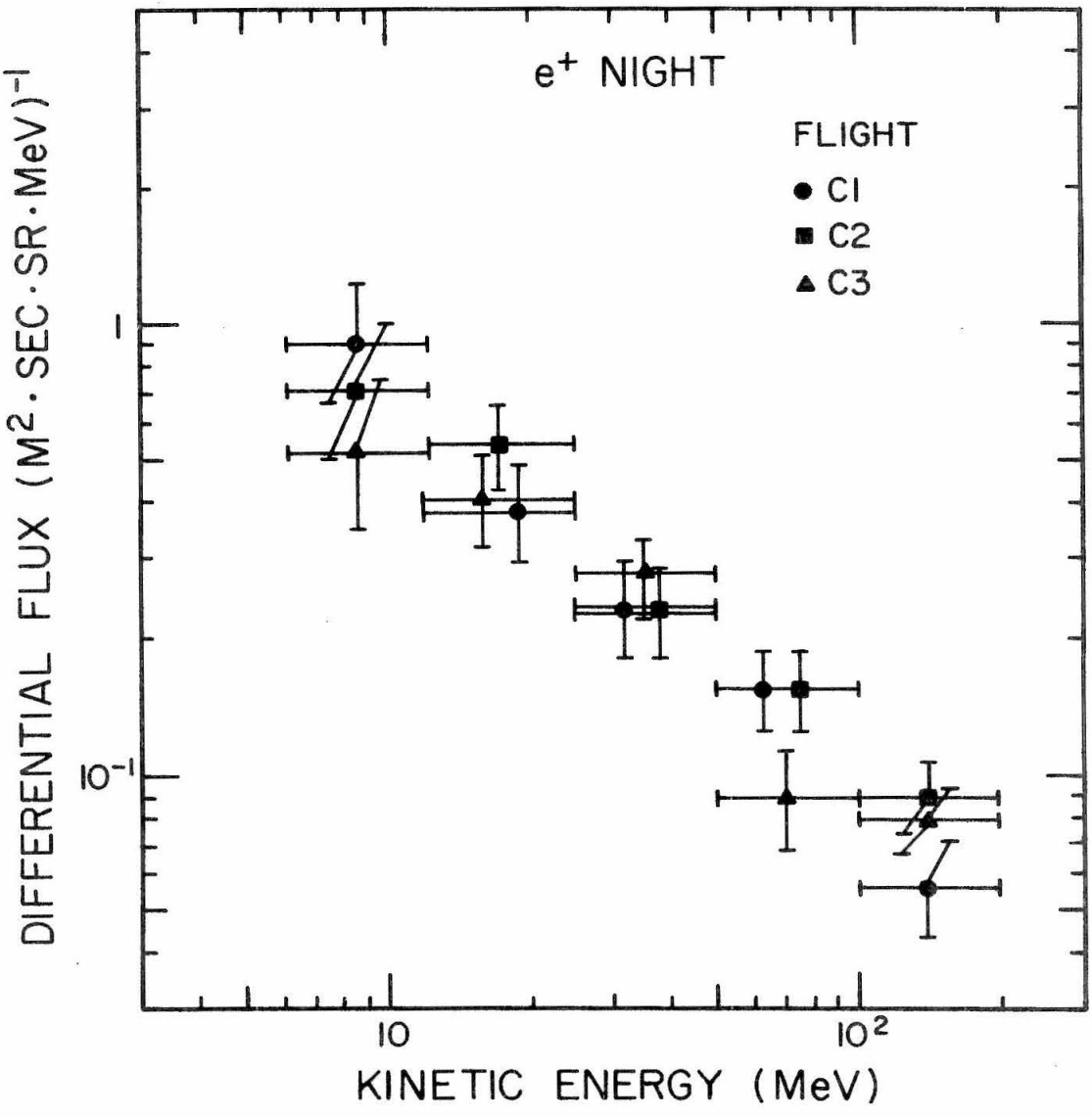
e+ NIGHT
FLIGHT
C1
C2
C3
DIFFERENTIAL FLUX (M2·SEC·SR·MeV)-1
1
10-1
10
102
KINETIC ENERGY (MeV)

Figure 26 A

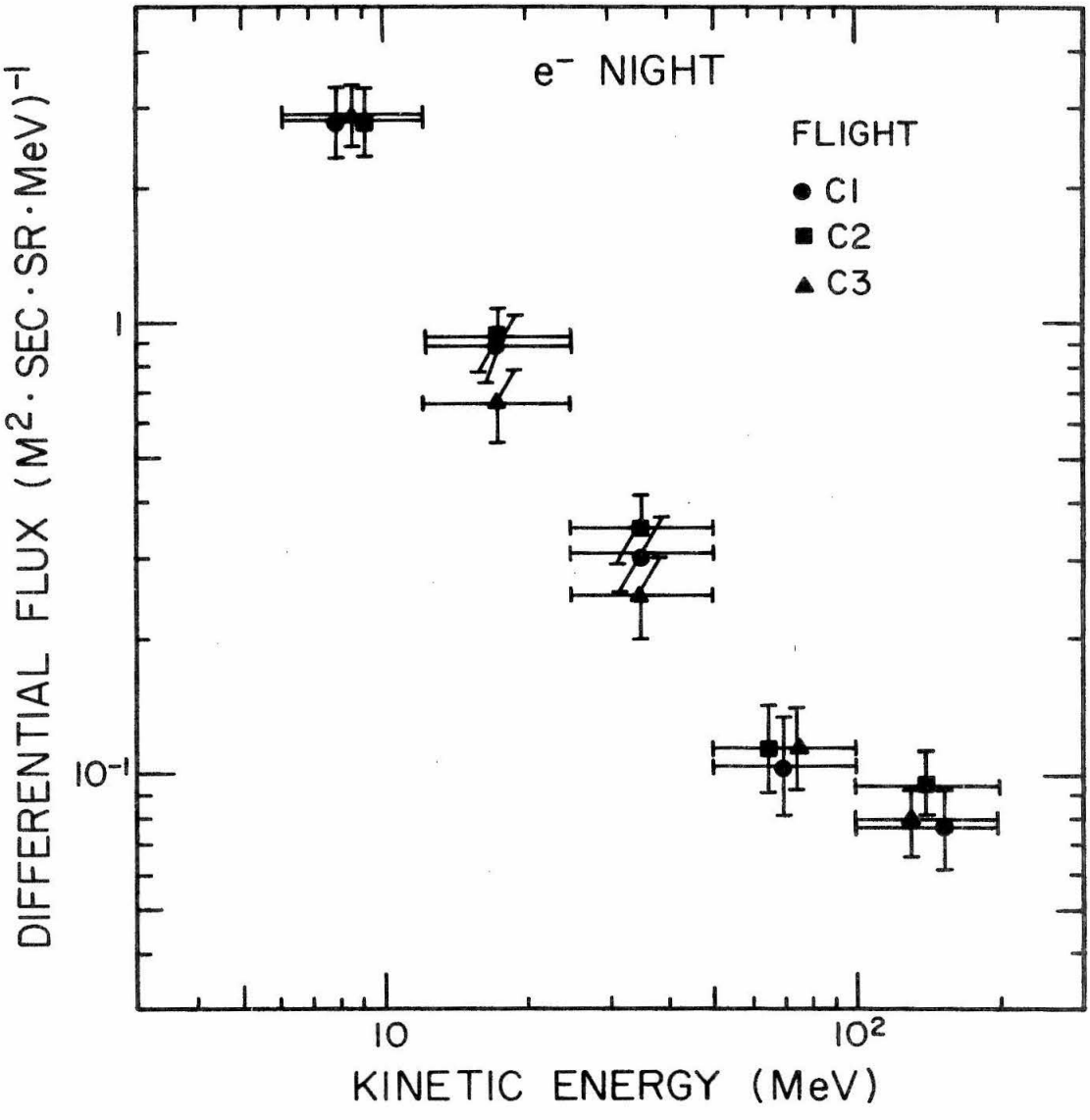
e⁻ NIGHT
FLIGHT
C1
C2
C3
DIFFERENTIAL FLUX (M².SEC.SR.MeV)⁻¹
1
10⁻¹
10
10²
KINETIC ENERGY (MeV)

Figure 26 B

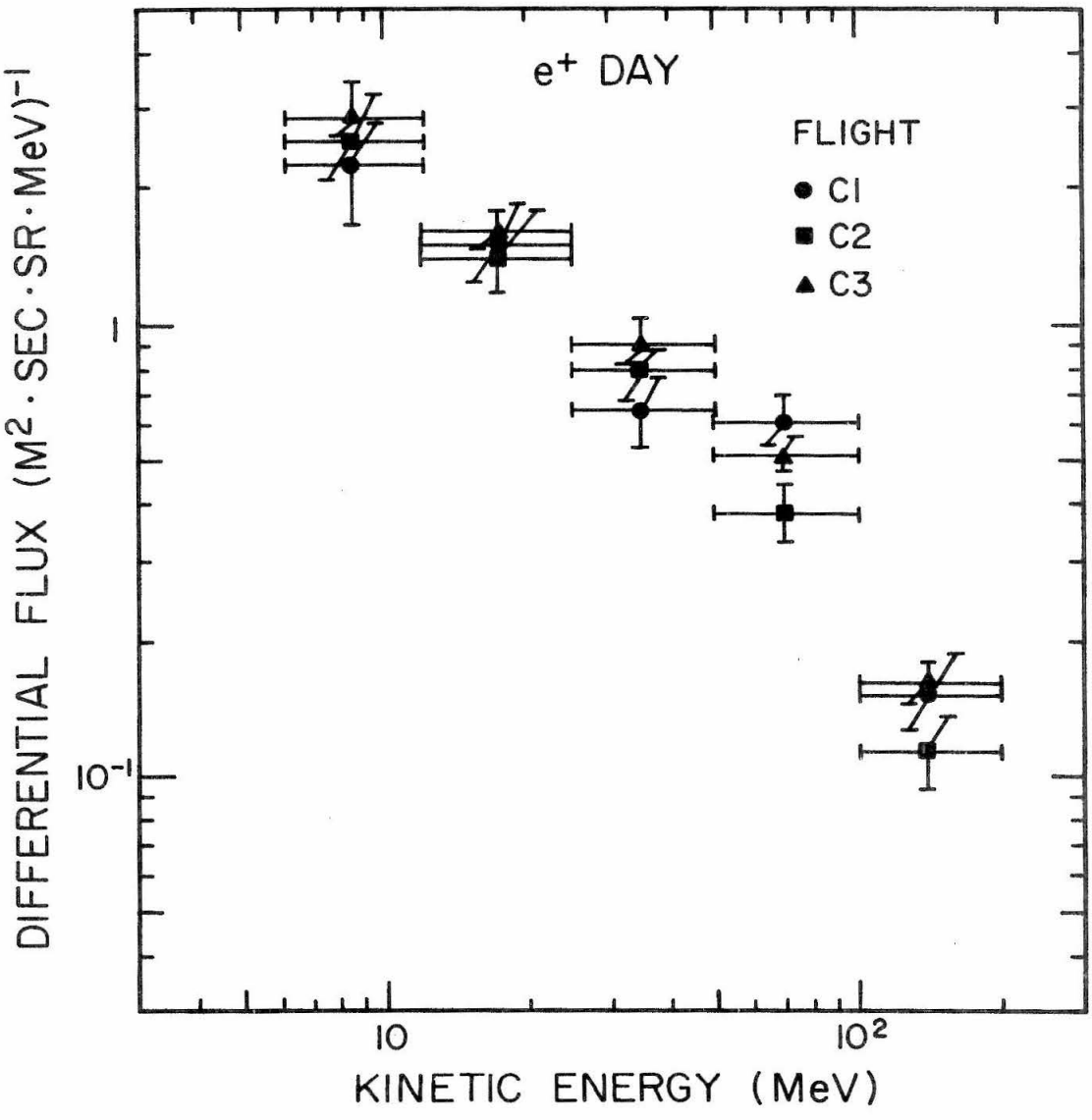
e+ DAY
FLIGHT
C1
C2
C3
DIFFERENTIAL FLUX (M2·SEC·SR·MeV)-1
1
10-1
10
10²
KINETIC ENERGY (MeV)

Figure 26 C

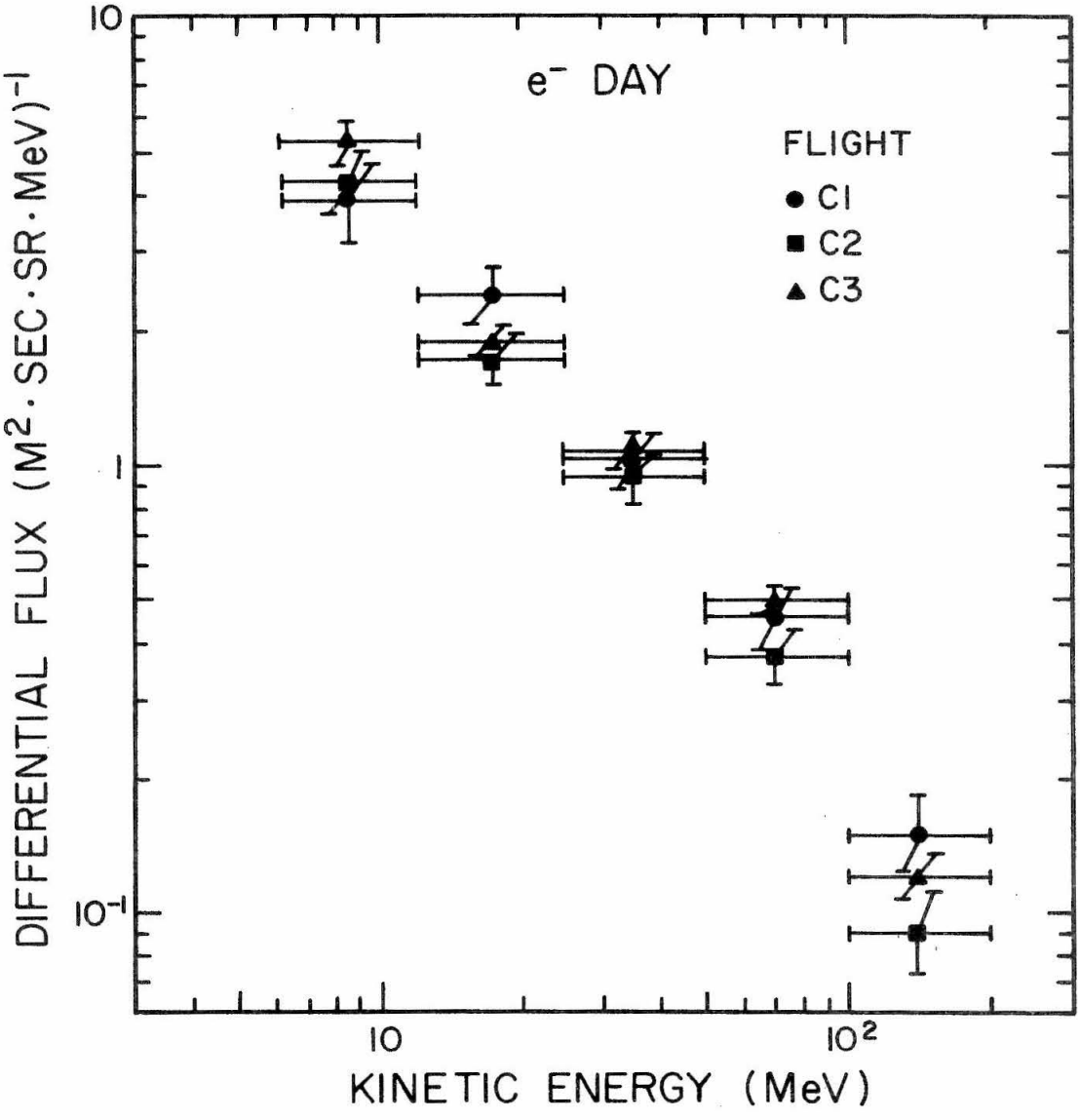
e⁻ DAY
FLIGHT
C1
C2
C3
DIFFERENTIAL FLUX (M².SEC·SR·MeV)⁻¹
KINETIC ENERGY (MeV)
10
1
10⁻¹
10
10²

Figure 26 D

(The daytime data for flight C3 have been corrected for the increased atmospheric secondary flux caused by the change in altitude toward the end of that flight. This is done in order that all daytime measurements apply to an average depth of 2.2 g/cm^2 residual atmosphere. All other values shown, day and night, are raw fluxes). Within the statistical uncertainty, the agreement among flights is good.

Comparison of the day and night spectra reveals large differences down to the lowest energy interval, 6-12 MeV at the detector. Below 6 MeV the geometrical factor of the detector goes quickly to zero and the electron detection efficiency of the Čerenkov counter is also declining. It is therefore not possible to use this interval for a reliable flux determination. Nevertheless, comparison of the measured nighttime and daytime rates, given in Table 4, shows that there is a well-defined diurnal variation for these electrons also. We conclude that the nighttime cutoff is well below our detector threshold of 6 MeV (corresponding to 11.1 MeV at the top of the atmosphere), and that our nighttime data are therefore free of contamination by return albedo.

In Figure 27 we show our measured daytime positron and negatron spectra, as well as their sum, corrected to the top of the atmosphere. We combine here the data from

TABLE 4

MEASURED RATES OF POSITRONS AND NEGATRONS BELOW 6 MeV

Rates for each flight and for daytime and nighttime intervals are given separately. The quoted errors include only statistical uncertainties.

Flight	Component	Nighttime Rate (hr^{-1})	Daytime Rate (hr^{-1})
C1	e^+	$0 \begin{smallmatrix}+ .6\\- 0\end{smallmatrix}$	$3.8 \begin{smallmatrix}+ 2.3\\- 1.5\end{smallmatrix}$
	e^-	$1.0 \begin{smallmatrix}+ 1.0\\- .6\end{smallmatrix}$	$3.8 \begin{smallmatrix}+ 2.3\\- 1.5\end{smallmatrix}$
C2	e^+	$.7 \begin{smallmatrix}+ .9\\- .4\end{smallmatrix}$	$2.6 \begin{smallmatrix}+ 1.6\\- 1.0\end{smallmatrix}$
	e^-	$1.6 \begin{smallmatrix}+ 1.1\\- .7\end{smallmatrix}$	$7.0 \begin{smallmatrix}+ 2.3\\- 1.7\end{smallmatrix}$
C3	e^+	$.3 \begin{smallmatrix}+ .2\\- .3\end{smallmatrix}$	$1.7 \begin{smallmatrix}+ .8\\- .6\end{smallmatrix}$
	e^-	$3.8 \begin{smallmatrix}+ 1.3\\- 1.0\end{smallmatrix}$	$4.5 \begin{smallmatrix}+ 1.1\\- 1.0\end{smallmatrix}$

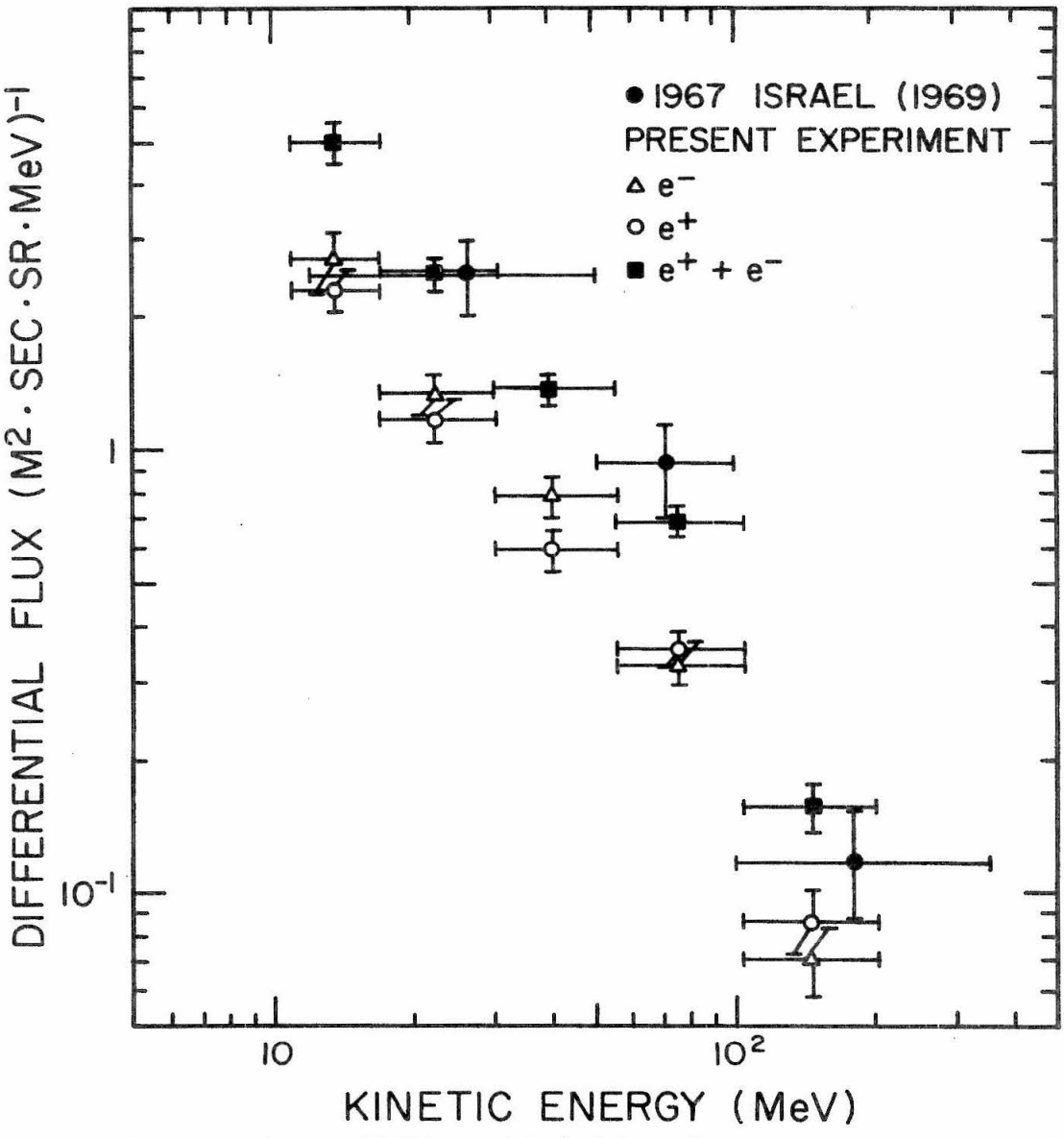

Fig. 27. Daytime differential kinetic-energy spectra of positrons, negatrons, and total electrons, incident at the top of the atmosphere. The data of Israel (Ref. (18)) are for the splash albedo in 1967.

all three flights. Also shown is the splash albedo spectrum at Fort Churchill measured by Israel (18) in 1967. Since the splash albedo flux is produced primarily by the nucleonic component above several BeV we would expect the spectrum in 1968 to be almost the same as in 1967. Our daytime flux agrees well with the splash albedo of Israel. In addition, the similarity of the spectra of the positron and negatron components can be taken as new evidence of the albedo origin of the daytime electron flux. Equal contributions of positrons and negatrons are expected in the albedo spectrum, which should be similar to the spectrum of atmospheric secondary electrons deep in the atmosphere. On the other hand, the spectra of extraterrestrial positrons and negatrons measured during the nighttime interval differ considerably from one another (see the next section.)

B) Primary cosmic-ray positrons and negatrons

1. Background

Our measurements of the cosmic-ray positron and negatron spectra have bearing upon such astrophysical topics as solar modulation and the origin and interstellar spectrum of the electron component of the cosmic rays (see Chapter I). In this section we shall briefly review the current state of theoretical and experimental knowledge of solar modulation as it pertains to our new data. A general review can be found in Webber (78).

While no theory of solar modulation has successfully explained all features of the observed temporal variations of the spectra of cosmic rays, there is reasonable agreement with the diffusion-convection model, first advanced by Parker in 1958 (79). In simple form, this model relates $j_E(R,t)$, the differential rigidity spectrum of a given cosmic-ray constituent observed at the earth at time t, to the interstellar spectrum $j_\infty(R)$ by

$$j_E(R,t) = j_\infty(R) \exp\left(-\frac{\eta(t)}{\beta f(R)}\right) \qquad (1)$$

Here η is a time dependent but rigidity independent parameter related to the geometry of the modulation region, β is the particle velocity in units of the speed of light, and $f(R)$ is a function of the particle rigidity R. According to the work of Jokipii (80) (81), $f(R)$ can be related in a straightforward way to the power spectrum of the magnetic irregularities in the solar wind. Measurements of the power spectrum imply (82)

$$f(R) \simeq \begin{cases} R^{-\delta} & \text{for } R > R_o \\ R_o^{-\delta} & \text{for } R < R_o \end{cases} \qquad (2)$$

where δ is between 0.5 and 1. The transition rigidity R_o is related to the correlation length of the magnetic

irregularities in the solar wind and should be on the order of several hundred MV based on the measurements of the magnetic field (82).

The above formulation of the diffusion-convection theory neglects the effect of adiabatic deceleration during passage of the cosmic rays through the solar wind. The effect is included in the Fokker-Planck equation proposed by Parker (83), but a general solution is difficult, and up to this time only special cases have been examined in the literature (81) (83-86). Gleeson and Axford (87) and Fisk and Axford (88) have used a somewhat different approach to the same problem. In all cases, however, the application at low rigidities is uncertain due to a lack of knowledge of the applicable diffusion coefficient.

The most extensive cosmic-ray data exist for protons and helium nuclei. Because knowledge of their interstellar spectra is lacking, however, it is not possible to determine the absolute modulation, and so study of the solar modulation of protons and helium nuclei has been necessarily limited to temporal variations. From equation (1), it follows that the relationship of the intensities at two different times, t_1 and t_2, is

$$\beta \ln \frac{j_E(R,t_1)}{j_E(R,t_2)} = \frac{\eta(t_2) - \eta(t_1)}{f(R)} \qquad (3)$$

provided there is no change in the functional form of f(R). Time variations of the proton and alpha particle spectra give reasonable agreement with the functional form of f(R) given in eq. (2) with $\delta \simeq 0.5\text{-}1.0$ and $R_o \simeq 500$ MV (78) (82). The data do not extend below several hundred MV rigidity, however.

Several investigators have studied temporal changes in the measured electron spectrum and have come to differing conclusions. L'Heureux, Meyer, Verma, and Vogt (89) report essentially no change in the electron spectrum between 250 and 1050 MV in the period 1960-1966. They quote an upper limit of 60 percent for the fractional change in modulation during this time. Bleeker, Burger, Deerenberg, Scheepmaker, Swanenburg, and Tanaka (90) report no change above 500 MV between 1965 and 1966. On the other hand, Rockstroh and Webber (12) claim to see significant continuing modulation from 1965 through 1968 for rigidities between 20 MV and 1 GV. In addition, Bleeker, et al. (13) have recently reported a reduction in the electron intensity between 500 MV and 5 GV of about 30 percent between 1966 and 1968. However, the actual reported absolute fluxes of Bleeker, et al. differ considerably from those of Rockstroh and Webber.

In view of these apparent inconsistencies, the question of the existence of a temporal change in the electron spectrum must be considered unresolved at the present time. This question is an important one. The temporal variation of the proton and helium modulation is well known. Electrons, with their much smaller mass-to-charge ratio, could be of great value in distinguishing between possible models of the modulation mechanism, as well as extending the measurements to very low rigidities where measurements of nuclear species are particularly difficult.

The problem of ultimate concern, however, is the determination of the total, or absolute, solar modulation, for which it is necessary to know or be able to estimate the interstellar spectrum $j_\infty(R)$ as well as the directly measured spectrum at the earth, $j_E(R,t)$. This restriction severely limits the cosmic-ray constituents which can be used to determine the absolute solar modulation. Ramaty and Lingenfelter (91) have calculated the interstellar spectra of deuterium and helium-3 assuming that these particles are produced in collisions of cosmic-ray nuclei with the interstellar gas. Comparing with measured intensities at rigidities > 600 MV they found good agreement with the modulation function of eqs. (1) and (3) with $\eta = 350 \pm 150$ MV, $\delta \simeq 1$, and $R_o < 600$ MV. Experimental difficulties prevent reliable measurements at lower

rigidities. Several authors have attempted to deduce the interstellar electron spectrum from the galactic background synchrotron radiation (92-94). These calculations involve the estimation of certain galactic parameters, notably the interstellar magnetic field. In general, the results indicate modulation in reasonable agreement with eq. (1) and (3) with η = 500 - 1000 MV and $R_o \lesssim 300$ MV. Interstellar absorption below ~ 10 Mhz limits this method to rigidities > 200 MV.

This restriction to rigidities above several hundred MV does not apply to the derivation of the absolute solar modulation employing cosmic-ray positrons. We make the assumption that all of the cosmic-ray positrons with energies above a few MeV originate in the decay of charged pions produced in interstellar collisions between high-energy cosmic-ray nuclei and the ambient matter. The interstellar negatron and positron spectra from this source can be calculated with reasonable accuracy (27-29). We shall use here the calculation of Ramaty and Lingenfelter (28), which uses an integral path length of 4 g/cm^2 for cosmic rays in the interstellar medium. By comparing our measured positron spectrum at the earth with the calculated interstellar spectrum, we derive the absolute solar modulation of positrons between 11 and 200 MV. The

conditions under which this modulation can be applied to other cosmic-ray constituents, in particular to negatrons, will be examined later.

2. Results

In Figures 26A and 26B we show the positron and negatron spectra measured during the nighttime interval of each of our three flights. In general the mutual agreement is good within the statistical accuracy of the measurements. In particular, there are no systematic deviations which might be associated with the recovery phase of the Forbush decrease which is evident in the neutron monitor count rates shown in Figure 13. The altitude profiles of all three flights were very similar to well past the time of the morning cutoff transition (Figure 12). The average nighttime float altitudes were 2.45, 2.40 and 2.35 g/cm^2 for flights C1, C2, and C3, respectively, with variations of $\pm$ .15 g/cm^2. We therefore consider the 3 flights equivalent and have combined the data for improved statistical accuracy in the subsequent analysis.

In Figure 28 we show the combined measured nighttime spectra at 2.4 g/cm^2 residual atmosphere. We also show the division into primary and secondary components according to the least-squares fitting technique described in Chapter IV, section E. The fits are made to the raw data, i.e., no

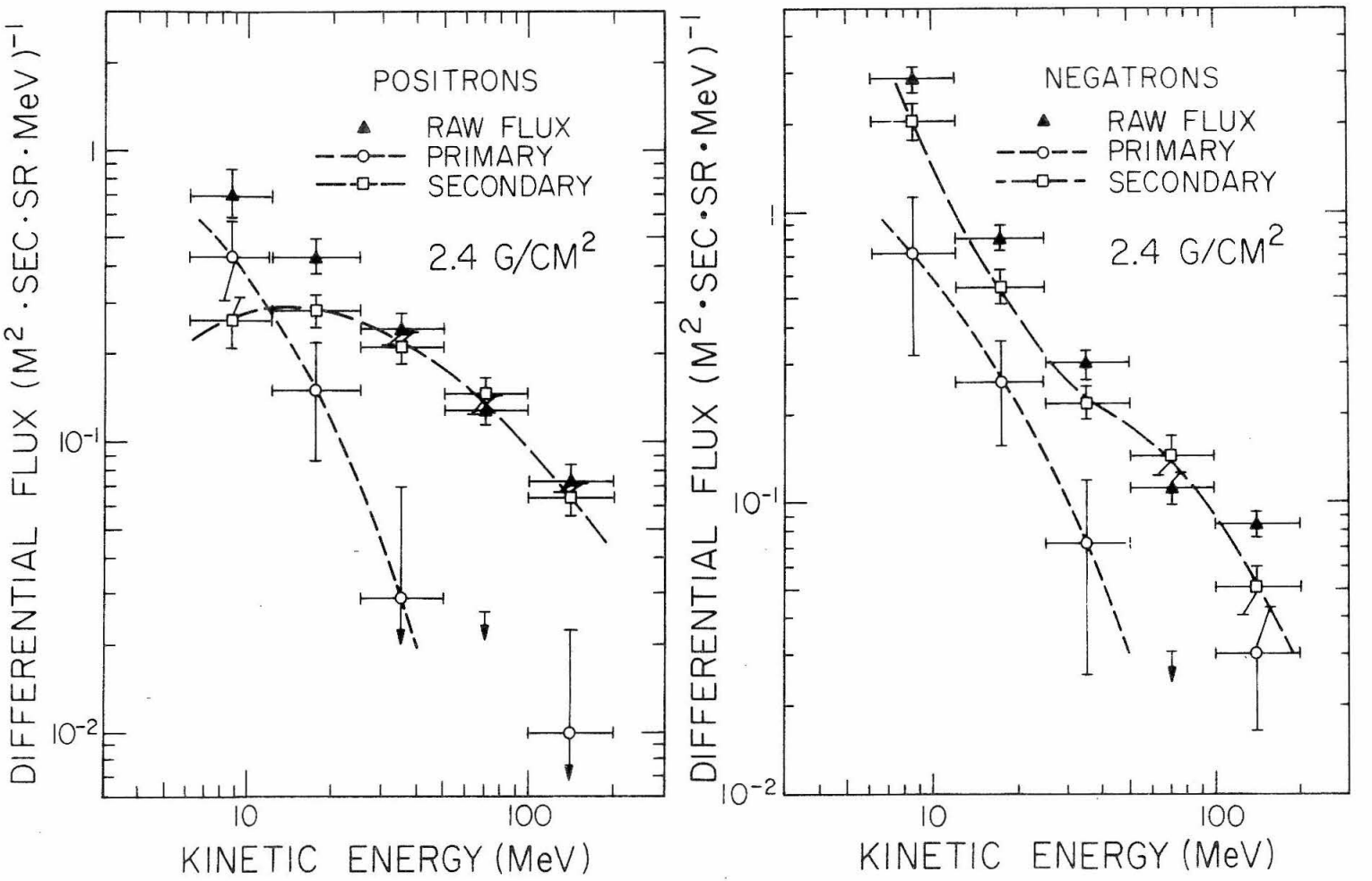

Fig. 28. Nighttime differential kinetic-energy spectra of positrons and negatrons at 2.4 g/cm^2 residual atmosphere. Shown are the measured spectra and the separation into primary and atmospheric secondary components as determined by the least-squares fitting technique described in the text.

corrections have been included for deflection resolution or for background events. The effect of folding in the resolution of the instrument was calculated and was found to influence the measured flux by less than one percent in any energy interval. This correction is not included in the quoted data. The atmospheric depth dependence of the principal causes of background events - γ-rays, splash albedo, and muons - is such that each source contributes almost exclusively to either the "primary" or the "atmospheric secondary" component as determined by the fit. In the case of the γ-ray and splash albedo background the contribution is to the separated "primary" spectrum. Background subtraction after the fit has been adopted in order to facilitate possible later adjustments in the background corrections should new data become available. This is particularly important for the γ-ray corrections where the present knowledge, both of the γ-ray spectrum at float altitude and of our detector sensitivity, is somewhat limited.

The "primaries" determined by the fit are 20-30 percent or less of the total measured flux with the single exception of the 6-12 MeV positron point where the contribution is $\sim$ 60 percent. Statistical error limits are correspondingly large. All error limits shown in Figure 28 are 1-σ statistical errors only. The fitting procedure

determined small negative "primary" contributions in the 50-100 MeV interval for both positrons and negatrons (see Figure 23). Hence we can indicate only upper limits for this interval. The upper limits shown in Figure 28 for the 50-100 MeV interval are the 1-σ uncertainties on the "primary" fit, taken from zero flux.

After subtraction of the γ-ray and splash albedo background the primary spectrum is corrected for energy loss to the top of the atmosphere. Only ionization loss is included. Bremsstrahlung loss also affects our highest energy interval. The magnitude of the correction depends on the spectral form at somewhat higher energies, however, and there is presently no general agreement on the spectrum immediately above 200 MeV. In any case the effect on the primary flux between 100 and 200 MeV is less that ± 5 percent for any reasonable extension of our own spectrum to higher energies. This value is small compared with the statistical errors. Our derived primary positron and negatron spectra at the top of the atmosphere are shown in Figure 29. The steps leading to our incident spectra are summarized in Table 5.

3. Discussion

In Figure 30 we show our primary electron ($e^+ + e^-$) spectrum together with some recent results of other

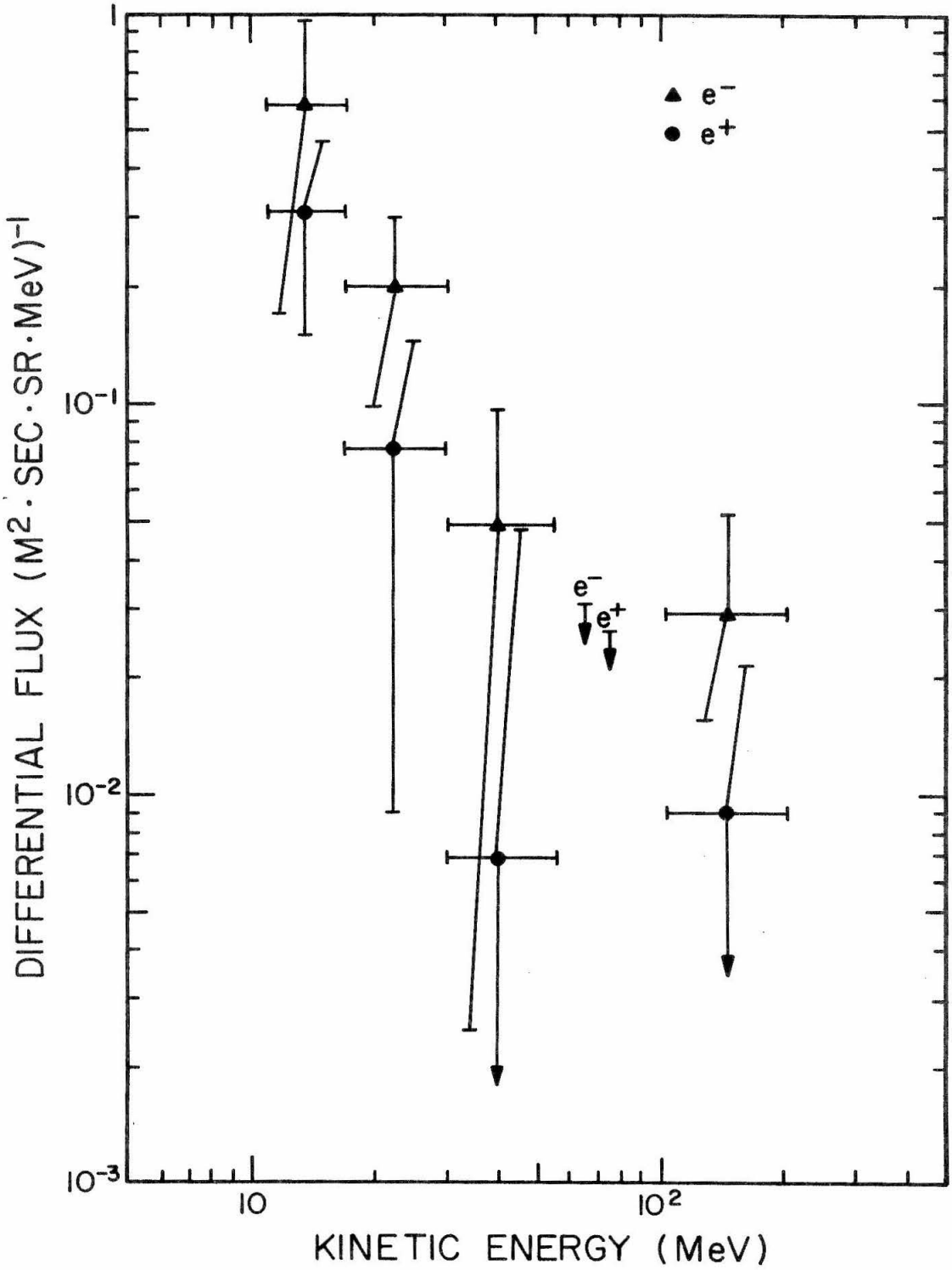

Fig. 29. Differential kinetic-energy spectra of positrons and negatrons.

TABLE 5

NIGHTTIME POSITRON AND NEGATRON FLUXES

A) Positrons. Flux values are in $(m^2 \cdot sec \cdot sr \cdot MeV)^{-1}$

Rigidity interval at the detector (MV)	6-12	12-25	25-50	50-100	100-200
Flux from combined flights	.71±.13	.44±.06	.24±.03	.13±.015	.075±.008
Least-squares fit separation					
1) "Primaries"	.44±.13	.15±.07	.030±.041	-.021±.026	.010±.012
2) "Secondaries"	.26±.05	.28±.04	.21±.03	.15±.02	.065±.009
Background corrections					
1) Splash albedo (1)	.03±.01	.03±.01	.016±.005	.0045±.0045	.0010±.0003
2) γ-ray (1)	.09±.09	.044±.030	.006±.003	---	---
Corrected primary positrons at 2.4 g/cm^2 residual atmosphere	.31±.16	.078±.069	.007±.042	0+.026	.009±.012
Energy interval at top of atmosphere (MeV)	11.1-17.1	17.1-30.2	30.2-55.2	55.2-104.9	104.9-203.9
Flux at top of atmosphere	.31±.16	.077±.068	.007±.041	0+.026	.009±.012

(1) Error limits are estimated errors.

TABLE 5 (Cont.)

B) Negatrons. Flux values are in $(m^2 \cdot sec \cdot sr \cdot MeV)^{-1}$

Rigidity interval at the detector (MV)	6-12	12-25	25-50	50-100	100-200
Flux from combined flights	2.80±0.30	.81±.08	.30±.03	.11±.02	.084±.008
Least-squares fit separation					
1) "Primaries"	.72±.40	.26±.10	.072±.047	-.038±.030	.030±.014
2) "Secondaries"	2.05±.29	.55±.07	.22±.03	.15±.02	.051±.009
Background corrections					
1) Splash albedo (1)	.03±.01	.03±.01	.016±.005	.0045±.0045	.0010±.0003
2) γ-ray (1)	.10±.06	.025±.010	.0066±.0030	---	---
Corrected primary negatrons at 2.4 g/cm^2 residual atmosphere	.59±.41	.20±.10	.050±.048	0+.030	.029±.014
Energy interval at top of atmosphere (MeV)	11.1-17.1	17.1-30.2	30.2-55.2	55.2-104.9	104.9-203.9
Flux at top of atmosphere	.58±.40	.20±.10	.049±.047	0+.030	.029±.13

(1) Error limits are estimated errors.

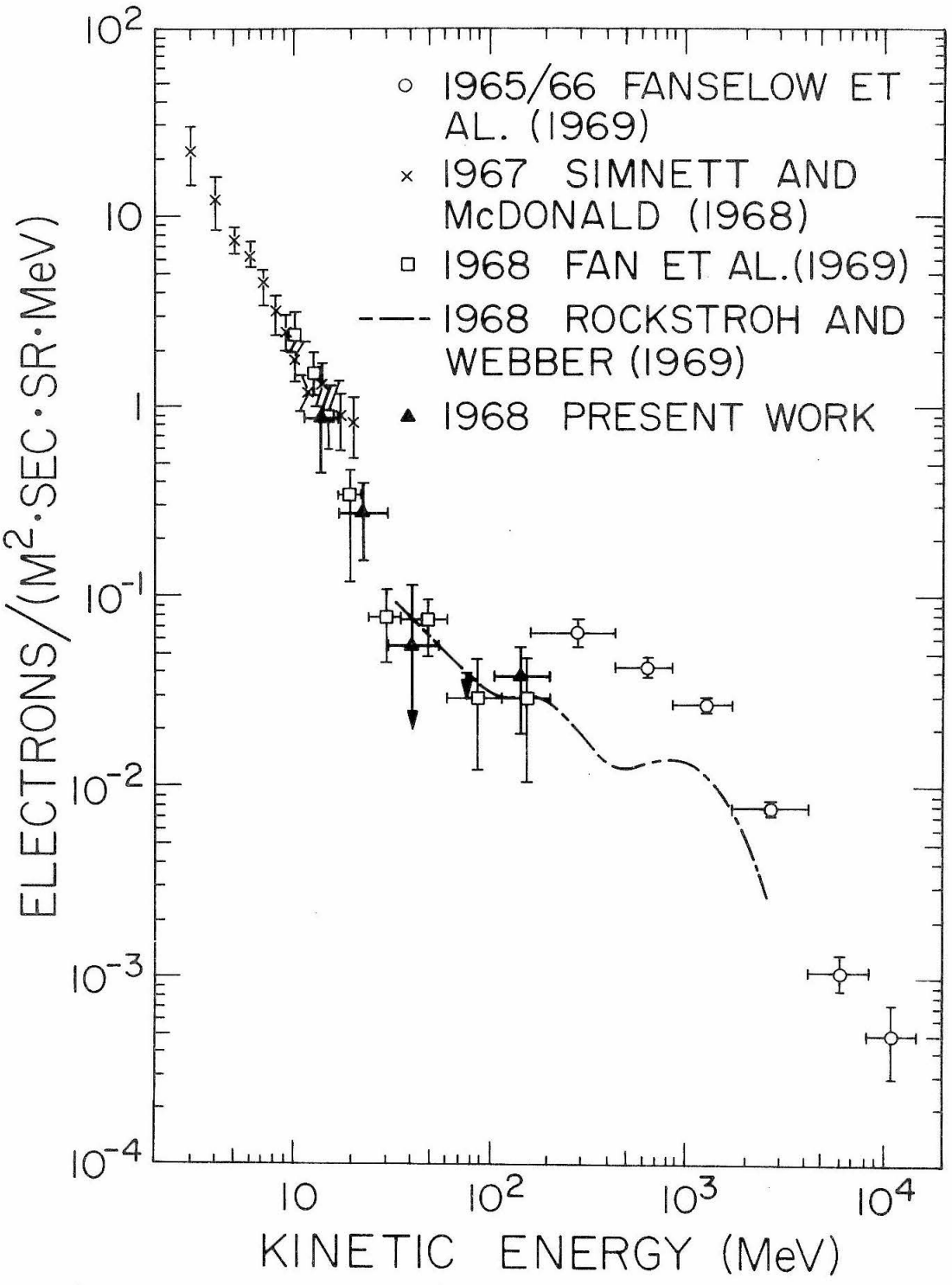

Fig. 30. Differential kinetic-energy spectrum of extraterrestrial cosmic-ray electrons ($e^+ + e^-$)

investigators. The data of Simnett and McDonald (21) and of Fan, L'Heureux, and Meyer (17) are satellite measurements and are thus free of contamination by atmospheric secondaries. Where their measurements overlap our own the agreement is very good. This is a good indication of the validity of our correction technique for atmospheric secondaries.

Earlier measurements of the electron spectrum in the energy range 10-200 MeV are generally higher than our values measured in 1968; this is true even if restricted to satellite measurements and to balloon data where the local cutoff is known to be below the detector threshold throughout the period included in the analysis (for a summary of such measurements see Israel (18)). Some of the variation might be due to increased solar modulation in 1968, but differing atmospheric secondary corrections may also play a significant role. The large contribution of atmospheric secondaries which are present in balloon data covering this energy interval render the derived primary spectrum very sensitive to this correction. The reduction technique for earlier satellite measurements at MeV energies has also been reexamined (21). The derivation of temporal changes of the solar modulation of electrons by combining data of different investigators is thus open to serious question and we shall not attempt it here.

In Figure 31 we show the positron fraction of the total electron flux, $N_{e^+}/(N_{e^+} + N_{e^-})$ as a function of energy. Plotted are our values between 11 and 204 MeV together with those of Fanselow, Hartman, Hildebrand, and Meyer (35) at higher energies. A positron fraction for the interval between 55 and 105 MeV cannot be derived because we have only upper limits for both components. With the exception of this energy interval and the interval from 30 to 55 MeV where statistics are very poor, the measured positron fraction lies between .24 and .35 from 11 MeV up to ~300-400 MeV. Also shown in Figure 31 is the interstellar positron fraction for the collision source. We have derived this curve by combining the calculation of Ramaty and Lingenfelter (28) for the pion-decay source with those of Abraham, Brunstein, and Cline (30) for the knock-on source. In Table 6 we use the calculated and measured positron fractions to determine the relative contributions of directly accelerated (primary) and collision-produced (secondary) electrons to the total cosmic-ray electron spectrum. We assume here and in the subsequent discussion that the collision source is the only significant source of positrons of these energies. Energy loss during the modulation process, which we have ignored, affects the derived primary and secondary electron contributions. We shall return to this point later.

Fig. 31. Positron fraction of the extraterrestrial electron flux, $N_{e+}/(N_{e+} + N_{e-})$. The dashed curve is the interstellar positron fraction for the collision source alone. It is derived by the author by combining the work of Ramaty and Lingenfelter (Ref. 28) and Abraham, Brunstein, and Cline (Ref. 30).

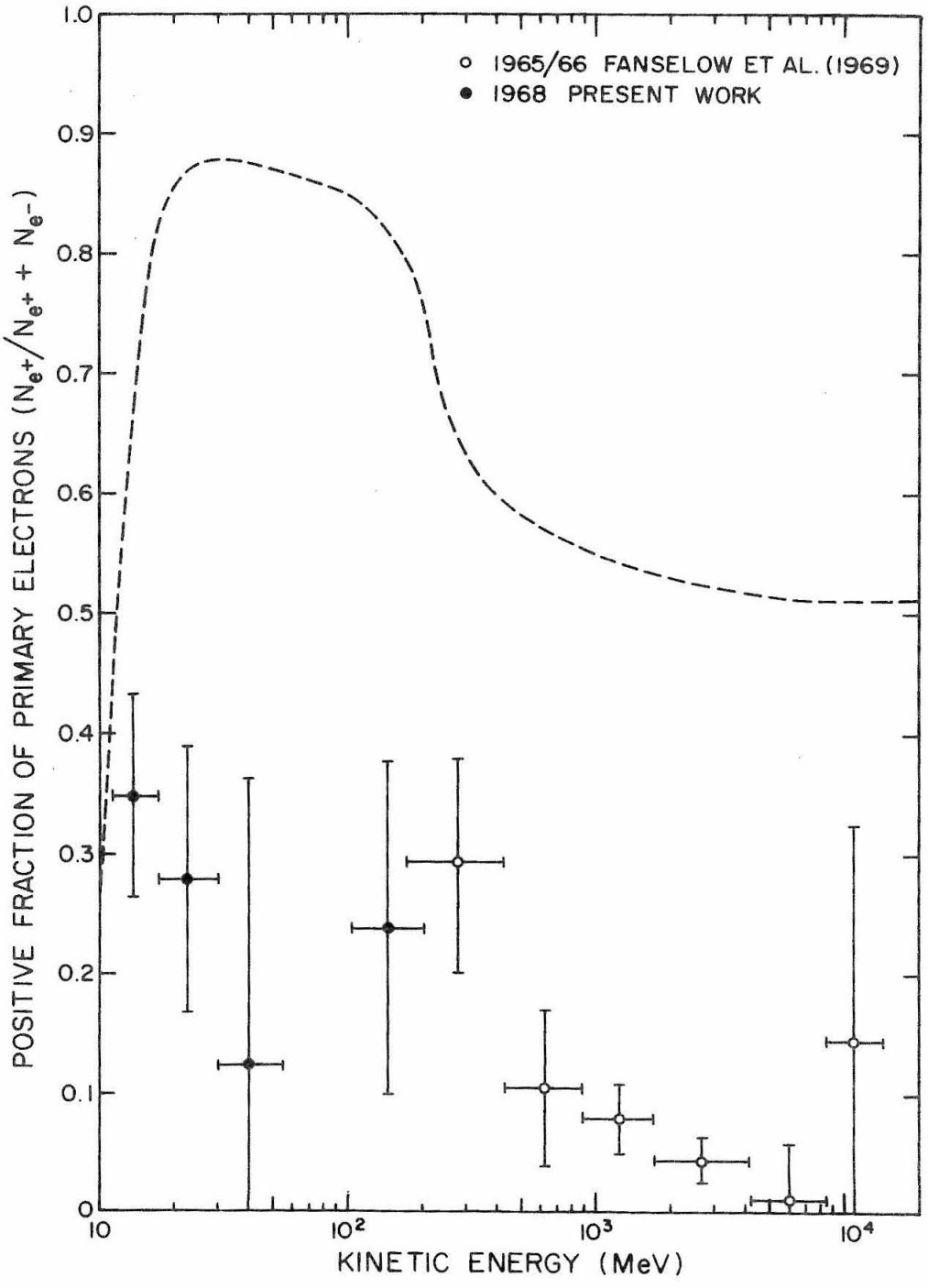
1.0
0.9
0.8
0.7
0.6
0.5
0.4
0.3
0.2
0.1
0
10
10^2
10^3
10^4
KINETIC ENERGY (MeV)
POSITIVE FRACTION OF PRIMARY ELECTRONS ($N_{e^+}/N_{e^+} + N_{e^-}$)
○ 1965/66 FANSELOW ET AL. (1969)
● 1968 PRESENT WORK

Figure 31

TABLE 6

POSITRON FRACTIONS

Measured energy interval (MeV)	11.1-17.1	17.1-30.2	30.2-55.2	55.2-104.9	104.9-203.9
Measured positron fraction $F_m = \frac{N_{e+}}{N_{e+}+N_{e-}}$	.35±.08	.28±.11	.12±.24	---	.24±.14
Positron fraction for pion-decay source F_π (1)	.9	.9	.9	.85	.85
Relative contribution of pion-decay secondaries to measured electron flux $T_\pi = \frac{F_m}{F_\pi}$ (2)	.39±.09	.31±.12	.13±.27	---	.28±.16
Positron fraction for secondary electron source F_s (3)	.65	.9	.9	.85	.85
Relative contribution of primaries to measured electron flux $T_p = 1 - \frac{F_m}{F_s}$ (2)	.46±.12	.69±.12	.87±.27	---	.72±.16

(1) Ramaty and Lingenfelter (Ref. 28).
(2) Derivation of the listed values assumes insignificant energy loss during modulation.
(3) Includes both the interstellar pion-decay (Ref. 28) and knock-on (Ref. 30) sources.

In Figure 32 we plot our measured positron flux together with values reported by Fanselow, Hartman, Hildebrand, and Meyer (35), Kniffen, Cline, and Fichtel (44), and Cline and Porreca (43). The solid curve, e_s^+, is the interstellar equilibrium positron spectrum from pion decay as calculated by Ramaty and Lingenfelter (28). We define the modulation factor for a given energy interval as the ratio of the measured intensity to the calculated interstellar intensity for the same energy interval. The modulation factors which we derive are shown in Figure 33. This graph suggests rapidly decreasing modulation below about 50 MV. For example, the modulation factor between 11 and 17 MV is a factor of 50 greater than that between 30 and 55 MV (i.e., the modulation is less at the lower energies).

Fanselow *et al.* have suggested as a good fit to their own data the modulation function

$$\frac{j_{E(R,1965)}}{j_\infty(R)} = \begin{cases} \exp\ (-600/\beta R) & \text{for } R > R_o = 300 \text{ MV} \\ \exp\ (-600/\beta R_o) & \text{for } R \leq R_o = 300 \text{ MV} \end{cases} \qquad (4)$$

where the particle rigidity R is measured in MV. Use of eq. (4) with e_s^+ in Figure 32 yields curve *a* in Figures 32 and 33. This functional form is predicted by the diffusion-convection theory of solar modulation without

Figure 32. Differential kinetic-energy spectrum of extraterrestrial positrons, including data of other investigators. The year in which each measurement was made is indicated. The solid curve, e_s^+, is the interstellar positron spectrum from pion decay calculated by Ramaty and Lingenfelter for an integral path length of 4 g/cm^2 (Ref. 28). The modulated spectra a, b, and c are described in the text.

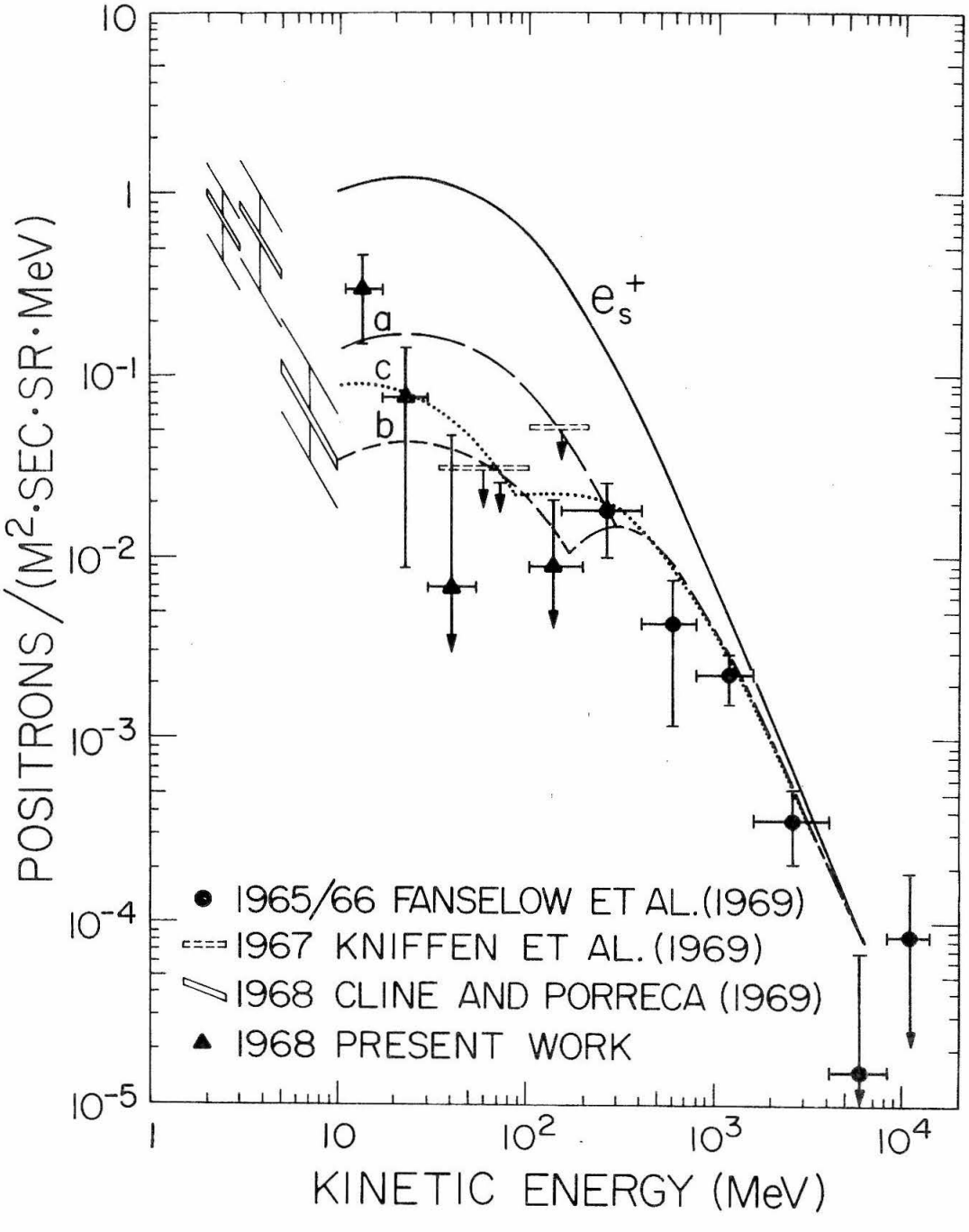
POSITRONS/(M²·SEC·SR·MeV)
KINETIC ENERGY (MeV)
10
1
10⁻¹
10⁻²
10⁻³
10⁻⁴
10⁻⁵
1
10
10²
10³
10⁴
a
b
c
e_s⁺
1965/66 FANSELOW ET AL.(1969)
1967 KNIFFEN ET AL. (1969)
1968 CLINE AND PORRECA (1969)
1968 PRESENT WORK

Figure 32

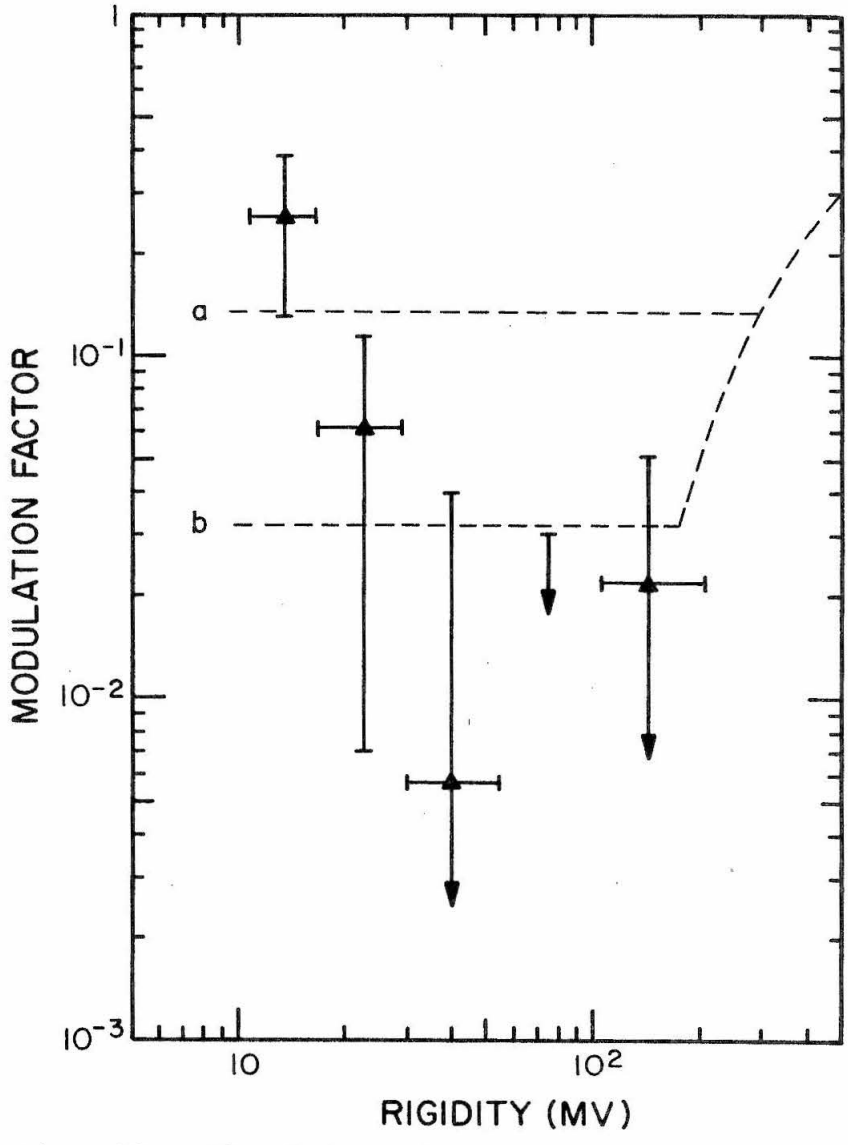

Fig. 33. Absolute solar modulation factors, $j_E(R,t)/j_\infty(R)$, for positrons in 1968. Curves a and b are modulation functions described in the text and also shown in Figure 32.

energy loss (equations (1) and (3)). The parameters are in reasonable agreement with values derived from data for cosmic-ray deuterium and helium-3 (91). On the other hand, curve a represents a very poor fit to our own data, having a chi-square probability much less than one percent. Due to the large error limits on our measurements, however, it is not possible to entirely exclude a similar modulation function with somewhat lower R_o, e.g., curve b in Figures 32 and 33 which is

$$\frac{j_E(R,\ 1968)}{j_\infty(R)} = \begin{cases} \exp\ (-600/\beta R) & R > R_o = 175\ \text{MV} \\ \exp\ (-600/\beta R_o) & R \leq R_o = 175\ \text{MV} \end{cases} \qquad (5)$$

and has a chi-square probability of 40 percent. This value of R_o would also be in approximate agreement with the rigidity at which Jokipii (82) suggests a change to β-dependent modulation on the basis of the observed power spectrum of the interplanetary magnetic field. Note that eq. (5) is an equally good fit to the data of Fanselow, et al. In the following discussion we shall take the derived modulation factors at face value; the fact that modulation functions such as eq. (5), which gives constant modulation at low rigidities, cannot be excluded should be kept in mind, however.

Our measured positron fractions (Figure 31) can be used together with the calculated interstellar positron spectrum (curve e_s^+ in Figure 32) to derive the galactic electron spectrum. In order to do this, however, it is necessary to know how much energy is lost by the electrons in reaching the inner solar system, i.e., at what energy in interstellar space the measured positron fractions are to apply. If we assume the energy loss to be an insignificant fraction of the original energy, we obtain curve 2 in Figure 34 for the galactic electron spectrum. The spectrum has been smoothly extrapolated above 200 MeV assuming no modulation above 5 GeV. Use of our measured positron fractions assuming no energy loss is equivalent to assuming equal modulation for the positron and negatron components. Also shown in Figure 34 are three estimates of the interstellar electron spectrum made by Webber (92), Verma (93), and Anand, Daniel, and Stephens (94) based on measurements of the galactic radio background. Although there is little actual overlap with our directly derived values, these estimates agree reasonably well with our extrapolated spectrum, particularly the estimate of Webber.

Curve 3 in Figure 34 is the calculated interstellar secondary electron spectrum for 4 g/cm^2 integral path length including both pion-decay (28) and knock-on

Fig. 34. Differential kinetic-energy spectra of interplanetary and of interstellar electrons.

Curve 1: composite interplanetary electron spectrum observed near the earth (see Figure 30). The closed squares are our measurements.

Curve 2: interstellar electron spectrum derived from curve 1 assuming insignificant energy loss during modulation. Our demodulated data points are shown as open squares.

Curve 3: interstellar secondary electron spectrum resulting from pion-decay (Ref. 28) and knock-on processes (Ref. 30).

Curve 4: interstellar primary electron spectrum, obtained by subtracting curve 3 from curve 2.

Also shown are galactic electron spectra obtained by Webber (Ref. 92), Verma (Ref. 93), and Anand, Daniel, and Stephens (Ref. 94), from studies of the galactic background synchrotron emission.

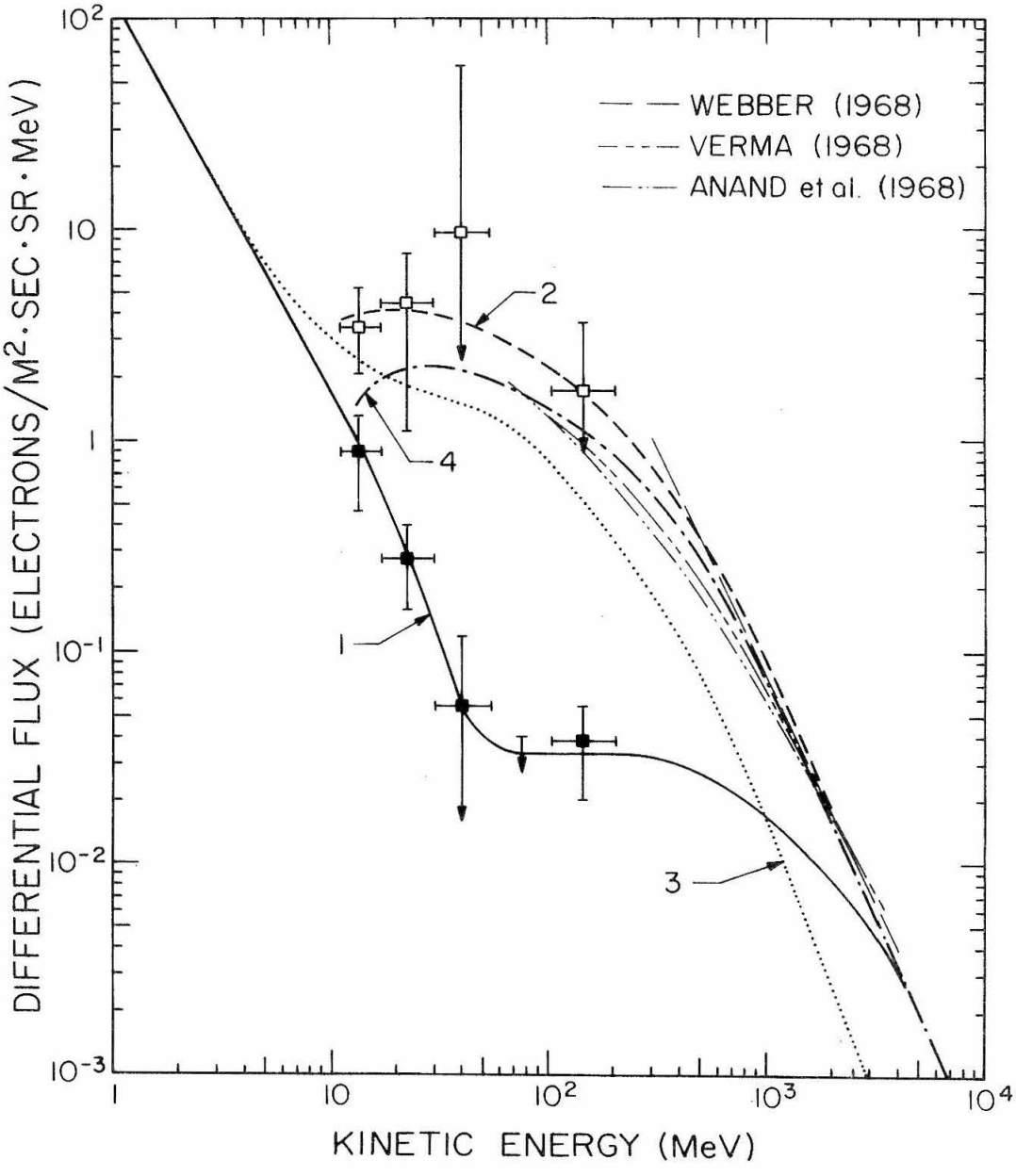
WEBBER (1968)
VERMA (1968)
ANAND et al. (1968)
1
2
3
4
DIFFERENTIAL FLUX (ELECTRONS/M²·SEC·SR·MeV)
KINETIC ENERGY (MeV)
10²
10
1
10⁻¹
10⁻²
10⁻³
1
10
10²
10³
10⁴

Figure 34

processes (30). Subtraction of curve 3 from curve 2 yields curve 4 for the equilibrium spectrum of primary electrons in the galaxy. This spectrum appears to have a broad peak around 30-50 MeV which, if real, might be associated with a minimum escape energy from the source region. Curve 1 in Figure 34 is a composite spectral shape for electrons measured near the earth in 1967-1968. Below about 10 MeV this spectrum is primarily the work of Simnett and McDonald (21). These authors have noted previously that their measured spectrum is compatible with a sole origin in the galactic knock-on component (the dominant contributor to the collision source below about 20 MeV) provided solar modulation is insignificant at these energies. Recently Beedle, Lezniak, Rockstroh, and Webber (95) have reported electron measurements which indicate that the similarity to the galactic knock-on spectrum may persist down to 200 keV. Our data imply that the modulation, though high near 100 MeV, does, in fact, seem to be rapidly decreasing below about 50 MeV. Furthermore, in Figure 32, extrapolation of the calculated positron spectrum, e_s^+, to lower energies would intersect the two lowest values of Cline and Porreca, which are thus consistent with no modulation. Their value between 5 and 10 MeV is inconsistent with no modulation, however. We note, however, that the spectral shape reported by Cline and

Porreca is one of several interpretations of their data. A mean flux value for the entire interval from 2 to 10 MeV is perhaps equally valid; such a value would fall reasonably close to the interstellar positron intensity from pion decay (96). The absence of significant modulation at low energies would also help to explain the lack of long-term variations in the 3-12 MeV electron flux which has been noted by Cline and McDonald (20). This absence is especially striking in view of large short-term variations of this component seen by the same authors. The interplanetary magnetic field has been observed to have a filamentary structure (97-99) with flux tubes down to perhaps 4000 km in diameter (approximately the cyclotron radius of a 70 MV particle). Beuermann, Rice, Stone, and Vogt (100) have noted that a well ordered field within such flux tubes might enable low-rigidity particles to penetrate into the inner solar system without undergoing significant modulation. Parker (83) has also suggested, on the basis of measurements of the interplanetary magnetic field, that low-energy electrons ($\lesssim$ 10 MeV) may have relatively free access to the inner solar system.

Up to this point we have not considered the adiabatic cooling of the cosmic-ray particles diffusing through the expanding solar wind. The energy loss due to this effect may not be insignificant, however. Parker (84) has

estimated that a cosmic-ray particle which penetrates to the earth will have lost 5-20 percent of its original energy. At the low rigidities with which we are primarily concerned the energy loss could be even higher, however, perhaps as high as 50 percent or more. We shall examine here the general effect which energy losses of this magnitude would have on our earlier discussion.

The relative contribution, T_π, of pion-decay secondaries to the electron flux measured at energy E is

$$T_\pi(E,E') = \frac{F_M(E)}{F_\pi(E')}$$

where F_M is the positron fraction measured at the earth, $F_\pi(E')$ is the positron fraction calculated for the pion-decay source at energy E' in interstellar space, and $\Delta E = E' - E$ is the energy lost by the electrons in reaching the earth. In Table 6 we list the values of T_π derived for each of our 5 energy intervals assuming $\Delta E = 0$. It is apparent from Table 6 that both F_M and F_π are relatively constant from 11 to 200 MeV. It follows that the derived values of T_π do not significantly change for $\Delta E/E'$ as high as .5 or greater. This is true whether T_π is considered at the earth (i.e., at fixed E) or in interstellar space (i.e., at fixed E'). A direct consequence is that the derived interstellar differential kinetic-energy spectra

of all electrons and of directly accelerated electrons, curves 2 and 4 in Figure 34, are not appreciably altered even for quite a large energy loss ($\Delta E/E'$ as large as .5-.7). Because of adiabatic deceleration, the derived interstellar spectra will not, of course, reach to energies as low as those we have measured at the earth. Furthermore our lowest measured interval, 11.1-17.1 MeV, contains an insignificant knock-on contribution for $\Delta E/E'$ as small as .2-.3. Thus, even though there would still be a good indication of a considerable flattening in curves 2 and 4 in Figure 34 below several hundred MeV, support for the sole knock-on origin of electrons below ~10 MeV must be considered weakened.

Adiabatic cooling of the cosmic-ray particles may itself cause some of the apparent decrease in solar modulation which we observe at low positron energies. Since no particles are actually lost due to adiabatic deceleration, the presence of the broad maximum around 30-35 MeV in the interstellar differential kinetic-energy spectrum of positrons (e_s^+ in Figure 32), coupled with a significant energy loss, leads to an accumulation of positrons at low energies. We shall illustrate the approximate effect by including this energy loss with the simple modulation function given by eq. (5). The discussion will be similar

to a section in Parker (83) with some change of notation. Derivations of the relevant equations can be found in this source or references quoted therein.

We shall consider a radial solar wind with constant velocity v and let the cosmic-ray diffusion coefficient κ be isotropic and uniform out to the boundary of the modulation region at r = L. In the absence of energy loss, the cosmic-ray intensity at the earth, $j_E(R,t)$, is reduced relative to the interstellar intensity $j_\infty(R)$ by the factor

$$\frac{j_E(R,t)}{j_\infty(R)} = \exp\ (-Lv/\kappa) \tag{7}$$

Comparison of eqs. (5) and (7) shows that the modulation function assumed in eq. (5) is equivalent to

$$\kappa = \begin{cases} \frac{Lv}{600}\ \beta R & R > R_o = 175\ \text{MV} \\ \frac{Lv}{600}\ \beta R_o & R \leq R_o = 175\ \text{MV} \end{cases} \tag{8}$$

The rate of energy loss of a relativistic particle which is undergoing adiabatic deceleration is given by

$$\frac{1}{E}\frac{dE}{dt} = \frac{2v}{3r} = \frac{1}{t_E} \tag{9}$$

where t_E is the characteristic time of the energy loss rate.

We now make two further approximations. First, we assume that as a particle loses energy, the diffusion coefficient which applies to its motion does not change, i.e., κ is constant for a given particle and, in particular, is the value applicable to the rigidity R' of the particle when it first entered the modulation region. With the assumed form for κ (eq. (8)), this condition is fulfilled in any case for $R' \lesssim 175$ MV. Thus the low-rigidity interval with which we are primarily interested is not affected. Second, we substitute for r in eq. (9) a characteristic value r_o such that t_E can be taken to be a constant. With these simplications, it follows directly from integrating eq. (9) that the energy of a cosmic-ray particle at the earth is

$$E = E' \exp(- t_L/t_E) \qquad (10)$$

Here t_L is the time required to diffuse into the inner solar system. It is approximately

$$t_L = L^2/4\kappa \qquad (11)$$

Combining eqs. (8), (10), and (11), we obtain

$$E \simeq \begin{cases} E' \exp\left(-\frac{100\ L}{\beta R' r_o}\right) & R' > R_o = 175\ \text{MV} \\ E' \exp\left(-\frac{100\ L}{\beta R_o r_o}\right) & R' \leq R_o = 175\ \text{MV} \end{cases} \qquad (12)$$

We can obtain an estimate of the energy loss of the cosmic-ray electrons by substituting $r_o = L$ into eq. (12). In that case we find, for example, that $E \simeq .6E'$ for $E' \leq 175$ MeV and $E \simeq .9E'$ for $E' \simeq 1000$ MeV.

The total effect on the interstellar positron spectrum e_s^+ is derived by including energy loss as given by eq. (12) with the simple diffusion-convection modulation as given by eq. (5). The energy loss is normalized by taking $E = .5E'$ for $E' \leq 175$ MeV and we substitute R' for R on the right-hand side of eq. (5) (equivalent to an unchanging diffusion constant κ for a given particle). In this manner we obtain curve c in Figure 32 for the differential kinetic-energy spectrum of positrons at the earth. Curve c is to be compared with curve b which follows from eq. (5) without energy loss. The accumulation of particles at low energies is apparent; the greater similarity of curve c to the shape of our measured spectrum is also evident.

A measurement of the positron spectrum by itself does not lead to a determination of the magnitude of the

adiabatic deceleration. It seems likely that adiabatic deceleration has played some role in shaping the interplanetary positron spectrum which we observe. On the other hand, the general arguments advanced in support of decreasing modulation at low rigidities seem to result in a self-consistent picture which correlates many different observations. It is possible that both processes, adiabatic deceleration and decreasing modulation at low rigidities, contribute to shaping the cosmic-ray electron spectrum which we observe at the earth.

VI. CONCLUSIONS

In this thesis we have presented measurements of the cosmic-ray positron and negatron spectra between 11 and 204 MeV. The data lead to several conclusions.

1) We obtained new data relating to the behavior of charged particles inside the earth's magnetosphere. Our measurement of the diurnal intensity variation of electrons indicates that the local geo-magnetic cutoff at invariant latitude $\Lambda = 68°-70°$ was <11 MeV at night. The approximately equal contributions of positrons and negatrons in the daytime electron flux (Figure 27) is in agreement with the charge ratio expected for return albedo particles and is in marked contrast to the measured nighttime charge ratio. This feature supports the interpretation of the daytime electrons as return albedo and also allows us to eliminate albedo as a significant contamination in the nighttime electron flux.

2) We derived interplanetary positron and negatron spectra (Figure 29). Our total electron ($e^+ + e^-$) spectrum agrees well with recently reported satellite measurements (Figure 30). We measured a positron-to-total-electron ratio which lies between .24 and .35 over the major part of our energy interval. By comparing our measured positron flux with a calculated interstellar positron spectrum resulting from pion decay (28), we derived the magnitude of the absolute solar modulation of positrons in 1968 (Figure 33). The measured positron intensity near 50 MV was less than ~.03 times the interstellar flux; near 15 MV, however, the

modulation factor was ~.25. This apparent absence of significant modulation at low energies supports the suggestion that the knock-on component contributes significantly to the interstellar electron flux below ~10 MeV (21).

3) We derived the total interstellar electron spectrum, ignoring adiabatic deceleration during modulation (Figure 34). The extrapolation of this spectrum to higher energies agrees reasonably well with estimates based on the galactic background radio emission. We also derived the interstellar spectrum of directly accelerated (primary) electrons. This spectrum exhibits considerable flattening below several hundred MeV when compared with the electron spectrum at higher energies. We examined the general effect of adiabatic deceleration during the modulation process and found that many of our deductions (in particular, the derived interstellar total electron spectrum and the directly accelerated component) are not significantly affected, even for an energy loss as high as 50 percent of the original energy.

REFERENCES

1. M. Schein, W. P. Jesse, and E. O. Wollan, Phys. Rev. 59, 615 (1941).
2. R. I. Hulsizer and B. Rossi, Phys. Rev. 73, 1402 (1948).
3. C. L. Critchfield, E. P. Ney, and S. Oleksa, Phys. Rev. 85, 461 (1952).
4. K. O. Kiepenheuer, Phys. Rev. 79, 738 (1950).
5. S. Hayakawa, Prog. Theoret. Phys. 8, 571 (1952).
6. P. Meyer and R. Vogt, Phys. Rev. Letters 6, 193 (1961).
7. J. A. Earl, Phys. Rev. Letters 6, 125 (1961).
8. J. L'Heureux, Astrophys. J. 148, 399 (1967).
9. J. L'Heureux and P. Meyer, Can. J. Phys. 46, 892 (1968).
10. R. E. Beedle and W. R. Webber, Can. J. Phys. 46, 1014 (1968).
11. W. R. Webber, J. Geophys. Res. 73, 4905 (1968).
12. J. Rockstroh and W. R. Webber, J. Geophys. Res. 74, 5041 (1969).
13. J. A. M. Bleeker, J. J. Burger, A. J. M. Deerenberg, A. Scheepmaker, and Y. Tanaka, Phys. Rev. Letters 22, 1325 (1969).

14. K. C. Anand, R. R. Daniel, and S. A. Stephens, Phys. Rev. Letters 20, 764 (1968).

15. C. J. Bland, G. Boella, G. Degli Antoni, C. Dilworth, L. Scarsi, G. Sironi, B. Agrinier, Y. Koechlin, B. Parlier, and J. Vasseur, Nuovo Cimento 55B, 451 (1968).

16. J. L. Fanselow, Astrophys. J. 152, 783 (1968).

17. C. Y. Fan, J. L'Heureux, and P. Meyer, Eleventh International Conference on Cosmic Rays, Budapest, paper no. OG-24, to be published, 1969.

18. M. H. Israel, J. Geophys. Res. 74, 4701 (1969).

19. T. L. Cline, G. H. Ludwig, and F. B. McDonald, Phys. Rev. Letters 13, 786 (1964).

20. T. L. Cline and F. B. McDonald, Can. J. Phys. 46, 761 (1968).

21. G. M. Simnett and F. B. McDonald, Astrophys. J. 157, 1435 (1969).

22. S. Hayakawa and H. Okuda, Prog. Theoret. Phys. 28, 517 (1962).

23. S. Hayakawa, H. Okuda, Y. Tanaka, and Y. Yamamoto, Suppl. Prog. Theoret. Phys. 30, 153 (1964).

24. F. C. Jones, J. Geophys. Res. 68, 4399 (1963).

25. V. L. Ginzburg and S. I. Syrovatskii, The Origin of Cosmic Rays, (MacMillan Co., New York, 1964).

26. J. B. Pollack and G. G. Fazio, Astrophys. J. 141, 730 (1965).

27. R. Ramaty and R. E. Lingenfelter, J. Geophys. Res. 71, 3687 (1966).

28. R. Ramaty and R. E. Lingenfelter, Phys. Rev. Letters 20, 120 (1968).

29. G. C. Perola, L. Scarsi, and G. Sironi, Nuovo Cimento 52B, 455 (1967), and 53B, 459 (1968).

30. P. B. Abraham, K. A. Brunstein, and T. L. Cline, Phys. Rev. 150, 1088 (1966).

31. V. L. Ginzburg and S. I. Syrovatskii, Proc. Int. Conf. Cosmic Rays, London, 1, 53 (1965).

32. J. A. DeShong, R. H. Hildebrand, and P. Meyer, Phys. Rev. Letters 12, 3 (1964).

33. R. C. Hartmen, R. H. Hildebrand, and P. Meyer, J. Geophys. Res. 70, 2713 (1969).

34. R. C. Hartman, Astrophys. J. 150, 371 (1967).

35. J. L. Fanselow, R. C. Hartman, R. H. Hildebrand, and P. Meyer, Astrophys. J. 158, 771 (1969).

36. C. J. Bland, G. Boella, G. Degli Antoni, C. Dilworth, L. Scarsi, G. Sironi, B. Agrinier, Y. Koechlin, B. Parlier, and J. Vasseur, Phys. Rev. Letters 17, 813 (1966).

37. R. R. Daniel and S. A. Stephens, Phys. Rev. Letters 17, 935 (1966).

38. S. A. Stephens, Ph.D. Thesis, Tata Institute of Fundamental Research, Bombay, 1969.

39. K. C. Anand, R. R. Daniel, and S. A. Stephens, Eleventh International Conference on Cosmic Rays, Budapest, paper no. OG-42, to be published, 1969.

40. T. L. Cline and E. W. Hones, Jr., Can. J. Phys. 46, 527 (1968).

41. S. D. Verma, Astrophys. J. 156, L79 (1969).

42. R. Ramaty, F. W. Stecker, and D. Misra, Eleventh International Conference on Cosmic Rays, Budapest, paper no. OG-28, to be published, 1969.

43. T. L. Cline and G. Porreca, Transactions, American Geophysical Union 50, 308 (1969).

44. D. A. Kniffen, T. L. Cline, and C. E. Fichtel, Eleventh International Conference on Cosmic Rays, Budapest, paper no. OG-31 to be published, 1969.

45. C. Y. Fan, G. Gloeckler, J. A. Simpson, S. D. Verma, Astrophys. J. 151, 737 (1968).

46. J. R. Jokipii, J. L'Heureux, and P. Meyer, J. Geophys. Res. 72, 4375 (1967).

47. K. P. Beuermann, to be published, 1969.

48. C. P. Jupiter, J. A. Lonergan, and G. Merkel, in Protection Against Space Radiation, ed. by A. Reetz, Jr., and K. O'Brien (NASA SP-169, Washington, D. C., 1968), p. 257.

49. V. Perez-Mendez and J. M. Pfab, Nucl. Instr. Methods 33, 141 (1965).

50. F. A. Kirsten, K. L. Lee, and J. Conragan, IEEE Trans. Nucl. Sci. NS-13, 583 (1966).

51. J. C. Cain, S. J. Hendricks, R. A. Langel, W. V. Hudson, J. Geomag. and Geoelectricity, 335 (1967).

52. Environmental Data Service, ESSA, Solar Geophysical Data, IER-FB-289, pp. 94-98 (1968).

53. J. A. Lockwood, Univ. of New Hampshire, private communication.

54. J. V. Lincoln, J. Geophys. Res. 73, 7544 (1968).

55. Environmental Data Service, ESSA, Solar and Geophysical Data, IER-FB-293, pp. 130-135 (1969).

56. W. Galbraith and W. S. E. Williams, ed., High Energy and Nuclear Physics Data Handbook (Rutherford Lab., Chilton, England (1964), p. VIII-1.

57. J. F. Ormes and W. R. Webber, in Proceedings of the Ninth International Conference on Cosmic Rays, ed. by A. C. Strickland (Institute of Physics and the Physical Society, London, 1965) Vol. I, p. 349.

58. J. F. Ormes and W. R. Webber, Can. J. Phys. 46, 883 (1968).

59. S. D. Verma, Proc. Indian Acad. Sci. 66, 125 (1967).

60. G. C. Perola and L. Scarsi, Nuovo Cimento 46, 718 (1966).

61. C. E. Fichtel, D. A. Kniffen, and H. B. Ögelman, Astrophys. J. 158, 193 (1969).

62. M. A. Shea, D. F. Smart, and J. R. McCall, Can. J. Phys. 46, 1098 (1968).

63. C. J. Rice, Space Radiation Laboratory Internal Report, 1969.

64. H. Leinbach, J. Geophys. Res. 72, 5473 (1967).

65. E. C. Stone, J. Geophys. Res. 69, 3577 (1964).

66. G. A. Paulikas, J. B. Blake, and S. C. Freden, J. Geophys. Res. 73, 87 (1968).

67. M. H. Israel and R. E. Vogt, J. Geophys. Res. 74, 4714 (1969).

68. G. C. Reid and H. H. Sauer, J. Geophys. Res. 72, 197 (1967).

69. H. E. Taylor, J. Geophys. Res. 72, 1593 (1967).

70. R. Gall, J. Jimenez, and L. Camacho, J. Geophys. Res. 73, 1593 (1968).

71. D. F. Smart, M. A. Shea, and R. Gall, J. Geophys. Res. 74, 4731, (1969).

72. D. J. Williams and G. D. Mead, J. Geophys. Res. 70, 3017 (1965).

73. F. C. Michel, Planet. Space Sci. 13, 753 (1965).

74. J. W. Dungey, Phys. Rev. Letters 6, 47 (1961).

75. S. M. Krimigis and J. A. Van Allen, J. Geophys. Res. 72, 4471 (1967).

76. D. Hovestadt and P. Meyer, Eleventh International Conference on Cosmic Rays, Budapest, paper no. MO-118, to be published, 1969.

77. W. R. Webber, Private Communication.

78. W. R. Webber, in Proceedings of the Tenth International Conference on Cosmic Rays, Part A, ed. by

J. R. Prescott (University of Calgary, Calgary, Canada, 1967), pp. 146-193.

79. E. N. Parker, Phys. Rev. 110, 1445 (1958).

80. J. R. Jokipii, Astrophys. J. 146, 480 (1966).

81. J. R. Jokipii, Astrophys. J. 149, 405 (1967).

82. J. R. Jokipii, Can J. Phys. 46, 950 (1968).

83. E. N. Parker, Planet. Space Sci. 13, 9 (1965).

84. E. N. Parker, Planet. Space Sci. 14, 371 (1966).

85. J. R. Jokipii and E. N. Parker, Planet. Space Sci. 15, 1375 (1967).

86. L. A. Fisk and W. I. Axford, J. Geophys. Res. 73, 4396 (1968).

87. L. J. Gleeson and W. I. Axford, Astrophys. J. 154, 1011 (1968).

88. L. A. Fisk and W. I. Axford, J. Geophys. Res. 74, 4973 (1969).

89. J. L'Heureux, P. Meyer, S. D. Verma, and R. Vogt, Can. J. Phys. 46, 896 (1968).

90. J. A. M. Bleeker, J. J. Burger, A. J. M. Deerenberg, A. Scheepmaker, B. N. Swanenburg, and Y. Tanaka, Can. J. Phys. 46, 911 (1968).

91. R. Ramaty and R. E. Lingenfelter, Astrophys. J. 155, 587 (1969).

92. W. R. Webber, Australian J. Phys. 21, 845 (1968).

93. S. D. Verma, Astrophys. J. 152, 537 (1968).

94. K. C. Anand, R. R. Daniel, S. A. Stephens, Nature 217, 25 (1968).

95. R. E. Beedle, J. A. Lezniak, J. Rockstroh, and W. R. Webber, Eleventh International Conference on Cosmic Rays, Budapest, paper no. OG-22, to be published, 1969.

96. T. L. Cline and G. Porreca, Eleventh International Conference on Cosmic Rays, Budapest, paper no. OG-26, to be published, 1969.

97. W. C. Bartley, R. P. Bukata, K. G. McCracken, and W. R. Rao, J. Geophys. Res. 71, 3297 (1966).

98. K. G. McCracken and N. F. Ness, J. Geophys. Res. 71, 3315 (1966).

99. G. L. Siscoe, L. Davis, Jr., P. J. Coleman, Jr., E. J. Smith, and D. E. Jones, J. Geophys. Res. 73, 61 (1968).

100. K. P. Beuermann, C. J. Rice, E. C. Stone, and R. E. Vogt, Phys. Rev. Letters 22, 412 (1969).

Corrections to C. Rice Thesis

Page	Line	
64	8	read "σ_θ = .0027 and σ_θ = .003 radians, respectively."
108	24	change reference (44) to (46).
149	16	read "undergoing adiabatic deceleration in the expanding solar wind is given by"